

3-22-2012

Spectral and Spatial Coherent Emission of Thermal Radiation from Metal-Semiconductor Nanostructures

Shane N. McConnell

Follow this and additional works at: <https://scholar.afit.edu/etd>

Part of the [Plasma and Beam Physics Commons](#)

Recommended Citation

McConnell, Shane N., "Spectral and Spatial Coherent Emission of Thermal Radiation from Metal-Semiconductor Nanostructures" (2012). *Theses and Dissertations*. 1184.
<https://scholar.afit.edu/etd/1184>

This Thesis is brought to you for free and open access by the Student Graduate Works at AFIT Scholar. It has been accepted for inclusion in Theses and Dissertations by an authorized administrator of AFIT Scholar. For more information, please contact richard.mansfield@afit.edu.



**SPECTRAL AND SPATIAL COHERENT EMISSION OF THERMAL
RADIATION FROM METAL-SEMICONDUCTOR NANOSTRUCTURES**

THESIS

Shane N. McConnell, Captain, USAF

AFIT/EE.ABET/ENP/12-M01

**DEPARTMENT OF THE AIR FORCE
AIR UNIVERSITY**

AIR FORCE INSTITUTE OF TECHNOLOGY

Wright-Patterson Air Force Base, Ohio

DISTRIBUTION STATEMENT A
APPROVED FOR PUBLIC RELEASE; DISTRIBUTION UNLIMITED.

The views expressed in this thesis are those of the author and do not reflect the official policy or position of the United States Air Force, Department of Defense, or the United States Government. This material is declared a work of the U.S. Government and is not subject to copyright protection in the United States.

AFIT/EE.ABET/ENP/12-M01

SPECTRAL AND SPATIAL COHERENT EMISSION OF THERMAL RADIATION
FROM METAL-SEMICONDUCTOR NANOSTRUCTURES

THESIS

Presented to the Faculty

Department of Electrical and Computer Engineering

Graduate School of Engineering and Management

Air Force Institute of Technology

Air University

Air Education and Training Command

In Partial Fulfillment of the Requirements for the
Degree of Master of Science in Electrical Engineering

Shane N. McConnell
Captain, USAF


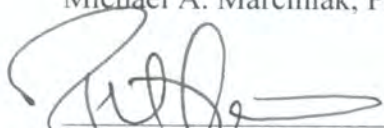
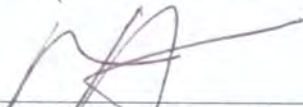

March 2012

DISTRIBUTION STATEMENT A
APPROVED FOR PUBLIC RELEASE, DISTRIBUTION UNLIMITED.

SPECTRAL AND SPATIAL COHERENT EMISSION OF THERMAL RADIATION
FROM METAL-SEMICONDUCTOR NANOSTRUCTURES

Shane N. McConnell
Captain, USAF

Approved:

 _____ Michael A. Marciniak, PhD (Chairman)	<u>9 Mar 12</u> Date
 _____ Peter J. Collins, PhD (Member)	<u>2 Mar 2012</u> Date
 _____ Maj Milo W. Hyde (Member)	<u>2 Mar 2012</u> Date
 _____ Stephen E. Nauyoks, PhD (Member)	<u>2 Mar 2012</u> Date

Abstract

The spectral and spatial radiative properties of coherent thermal emission in the mid- and far-infrared (mid-IR and far-IR) through the use of micro- and nano-structured metal-semiconductor materials were designed for and demonstrated experimentally. Using an efficient implementation of the Rigorous Coupled Wave Analysis (RCWA) numerical technique and Computer Simulation Technology (CST) electromagnetic modeling software, two structures were designed to selectively emit at mid- and far-IR wavelengths, a one-dimensional (1-D) truncated multilayer resonator and a three-dimensional (3-D) hybrid photonic crystal-multilayer (PC-multilayer). A High Impulse Power Magnetron Sputtering (HIPIMS) deposition technique was used to fabricate two silver-germanium-silver (Ag-Ge-Ag) resonating structures with layer thicknesses of 6-240-160 nm for one sample and 6-700-200 nm for the other. The design thicknesses of each sample were verified through both reflectance and standard spectral ellipsometric measurements at wavelengths from 2-15 μm . Reflectance measurements demonstrated spectrally selective absorption at the designed IR wavelengths whose general behavior was largely unaffected by a wide range of incident angles. Ellipsometric measurements showed significant disagreement between HIPIMS-deposited material properties and bulk values found in literature. Further, radiance measurements were taken at various high temperatures to investigate the effect of thermally excited surface waves on the radiative properties of the resonating structures. From these radiance measurements, spectral emittance was directly derived and compared to the emittance inferred from reflectance

measurements. It was established that inferring emittance can help to approximate the expected emission from a structure, but it is not an exact method of determining the actual emittance of a thermal source. Using CST, the 3-D hybrid PC-multilayer structure was simulated as a sub-wavelength square hole array embedded inside a Ag slab on a Si substrate to examine the spatial coherence achieved by this more complex geometry. Simulated results indicate strong angular and polarization dependencies of incident radiation at IR design wavelengths of interest. Initial fabrication results of the PC-multilayer involving both HIPIMS deposition of a Ge-Ag-Ge-Ag (4-12-270-200 nm) multilayer, and focused ion beam milling of a square array of 3.6- μm diameter circular holes are also presented.

Acknowledgments

First, I would like to thank my academic advisor, Dr. Michael Marciniak, for his guidance and time towards this research effort. I would also like to thank the other members of my thesis committee, Dr. Peter Collins, Maj Milo Hyde, and Dr. Stephen Nauyoks, for their support and active involvement throughout my time here at AFIT. The friendships developed with my classmates (more like teammates) through this endeavor will be cherished and have made the tough times not so tough and I thank them too. Above all, I'd like to thank my wife for being my lifeline and enduring my mind's "academic deployment".

My sincere appreciation goes out to the following individuals for whom made this research possible with their help and expertise:

- ❖ Mr. Scott Apt, FIB and SEM
- ❖ Dr. Kurt Eyink, Ellipsometry and Materials
- ❖ Maj. Nathan Glauvitz, SEM and Fabrication
- ❖ Ms. Stephanie Gray, IR-VASE and modeling
- ❖ Dr. Kevin Gross, FTIR
- ❖ Mr. Richard Johnston, Cleanroom and Photolithography
- ❖ Ms. Abbey Juhl, Nanoscribe and Photolithography
- ❖ Mr. Charlie McNealy, Electrodeposition
- ❖ Mr. Neil Murphy, Materials
- ❖ Mr. Michael Ranft, FTIR
- ❖ Capt. Michael Seal, Original RCWA Code, Thermal Radiative Properties, Plasmonics
- ❖ Capt. Spencer Sellers, Lumerical
- ❖ Mr. Greg Smith, Mask Aligner and Emissometer
- ❖ Mr. Thomas Stephenson, Zygo and Cleanroom
- ❖ Ms. Lirong Sun, HIPIMS deposition
- ❖ Mr. Vincent Tondiglia, Nanoscribe
- ❖ Jason Vap, CASI, Mueller matrix

Shane N. McConnell

Table of Contents

	Page
Abstract.....	iv
Acknowledgments.....	vi
List of Figures.....	x
List of Tables.....	xix
List of Symbols.....	xx
List of Abbreviations.....	xxiii
I. Introduction.....	1
General Issue.....	1
Problem Statement.....	4
Methodology.....	4
Implications/Applications.....	6
Preview.....	6
II. Theoretical Background.....	8
Chapter Overview.....	8
Conventions.....	8
Conservation of Energy and Kirchhoff's Law.....	9
Electromagnetic Theory and Constitutive Relations.....	11
Thermal Radiation.....	15
Surface Waves.....	16
Designing a Thermal Emitter.....	18
Scatterometry.....	20
Spectroscopic Ellipsometry.....	20
Summary.....	21
III. Literature Review.....	22
Review Papers.....	22
Relevant Research.....	23
Summary.....	25
IV. Methodology.....	26
Chapter Overview.....	26
Truncated Multilayer Resonator.....	27

	Page
<i>Constituent Material Properties</i>	28
<i>Angular Reflectance and Emittance of Ag</i>	35
<i>Fabrication</i>	38
Hybrid PC–Multilayer.....	40
<i>Design</i>	41
<i>Fabrication</i>	41
Reflectance/Ellipsometric Measurements.....	42
Calculating Emittance	43
Summary	45
V. Analysis and Results – Truncated Resonator.....	46
Chapter Overview	46
Truncated Multilayer Resonator Design	46
<i>Sample 1: 6-240-160 nm (Ag-Ge-Ag)</i>	47
<i>Sample 1: Fabrication Results</i>	49
<i>Sample 1: Reflectance Measurements</i>	52
<i>Sample 2: 6-700-200 nm (Ag-Ge-Ag)</i>	55
<i>Sample 2: Fabrication</i>	55
<i>Sample 2: Reflectance Measurements</i>	56
<i>Spectroscopic Ellipsometry</i>	59
<i>Radiance Measurements and Calculating Emittance</i>	67
Summary	80
VI. Analysis and Results – Hybrid PC-Multilayer	81
Chapter Overview	81
Hybrid PC-Multilayer Design	81
Hybrid PC-Multilayer: Initial Fabrication	89
Summary	98
VII. Conclusion.....	99
Future Work	102
<i>Design</i>	102
<i>Fabrication</i>	103
<i>Characterization</i>	107
Appendix A. Nanofabrication.....	109
3-D Laser Lithography: Initial Fabrication Results	109
Other Nanotechnology Characterization Techniques	112
Nanofabrication Literature.....	113

	Page
Appendix B. Supplemental IR-VASE Measurements and Modeling.....	114
Bibliography	121

List of Figures

Figures	Page
1. Illustration of the direction of propagation of radiation being emitted from a surface in spherical coordinates. Both θ and ϕ are measured with respect to the local coordinate system constructed from the surface normal.	11
2. Schematic representation of a surface plasmon at the interface between a surface that supports surface waves (Medium 1) and free space (Medium 2). The wave amplitudes decay exponentially with distance from the interface with decay constant α and distance from the interface z	17
3. Illustration of a transverse magnetic (TM) surface wave on a bare metal interface.	18
4. Calculated angular emittance of a Au-SiO ₂ -Au tri-layer resonator for (a) TM and (b) TE polarizations. The triangles and circles represent the measured reflectance dips obtained by an FTIR spectrometer and a laser scatterometer, respectively. From [11].	24
5. Illustration of a truncated multilayer resonator.	27
6. Index of refraction for Germanium using a temperature-dependent Sellmeier equation versus measured values reported by Li [55].	30
7. Reduction in reflectivity with rising temperature at 0.69 (left) and 10.6 μm (right) for silver (Ag), gold (Au), sodium (Na), copper (Cu), potassium (K), and aluminum (Al). From [56].	31
8. Real and imaginary parts of the complex dielectric function of silver at room 294 K (room temperature) and 1000 K as calculated from the free-electron/Drude.	33
9. Complex refractive index for Silver (Ag) using a free-electron/Drude model at 1000 K plotted with measured bulk values reported in Palik [44].	34
10. Calculated specular reflectance (p-pol) for Ag at 294 K (left) and 1000 K (right) from 0.1-10 μm . Specular reflectance at 294 K was calculated using complex refractive index from Palik [44]. Specular reflectance at 1000 K was calculated using complex refractive index values using a Drude model.	36
11. Calculated specular reflectance (p-pol) for Ag at 294 K (left) and 1000 K (right) from 0.1-0.5 μm . Specular reflectance at 294 K was calculated using complex refractive index from Palik [44]. Specular reflectance at 1000 K was calculated using complex refractive index values using a Drude model.	37

Figures	Page
12. Calculated specular emittance (p-pol) for Ag at 1000 K over two wavelength bands, 0.1-10 μm (left) and 0.1-0.5 μm (right). Specular emittance was calculated using complex refractive index values using a Drude model.	38
13. Scanning Electron Microscope (SEM) micrograph of the cross-section of a Ge sample deposited on a Si wafer and prepared by the Air Force Research Laboratory (AFRL) using a High Power Impulse Magnetron Sputtering (HIPIMS) technique. From [60].	39
14. Illustration of a photonic crystal-multilayer hybrid structure constructed of a circular hole array embedded inside of a truncated multilayer resonator.	40
15. Illustration of a photonic crystal-multilayer hybrid structure constructed of a square array of circular holes embedded inside of a multilayer, where a is the period between each hole and d is the diameter of each hole. View is from surface normal of the structure.	41
16. Comparison of the calculated angular emittance (p-pol) spectra of a Ag-Ge-Ag truncated multilayer resonator with varying thicknesses for the top, optically thin Ag layer.	48
17. Calculated angular emittance (p-pol) for a Ag-Ge-Ag resonating structure at 294 K (left) and 500 K (right) from 2-10 μm . Thicknesses of constituent materials are 6-240-160 nm, respectively.	49
18. Calculated specular emittance (p-pol) for a Ag-Ge-Ag resonating structure at 294 K (left) and 500 K (right) from 2-4 μm . Thicknesses of constituent materials are 6-240-160 nm, respectively.	49
19. SEM micrograph of a Ag-Ge-Ag truncated resonator (6-240-160 nm) on a silicon substrate. Ag and Ge layers were deposited via a High Power Impulse Magnetron Sputtering (HIPIMS) technique. Micrograph was taken at 100,000 \times magnification and at an angle of 52 $^\circ$ from surface normal.	50
20. SEM micrograph of a Ag-Ge-Ag truncated resonator (6-240-160 nm) on a silicon substrate. Measurements shown on the micrograph were made with the SEM showing several different estimates of the total height of the structure. Ag and Ge layers were deposited via a High Power Impulse Magnetron Sputtering (HIPIMS) technique. Micrograph was taken at 75,000 \times magnification and at an angle of 52 $^\circ$ from surface normal.	51

Figures	Page
21. Spectral reflectance (p-pol) of a Ag-Ge-Ag truncated resonator (6-240-160 nm) between 1.4 and 20 μm . Reflectance measurements were taken using a J. A. Woollam Infrared – Variable Angle Spectroscopic Ellipsometer (IR-VASE).	52
22. Spectral reflectance (p-pol) of a Ag-Ge-Ag truncated resonator (6-240-160 nm) on silicon between 1.7 and 6 μm . Reflectance measurements were taken using a J. A. Woollam Infrared – Variable Angle Spectroscopic Ellipsometer (IR-VASE).	53
23. Comparison (p-pol) between theoretical emittance results (left) and experimental emittance results (right) found through measurements taken using a J. A. Woollam Infrared Variable Angle Spectroscopic Ellipsometer (IR-VASE) for a Ag-Ge-Ag resonating structure with thicknesses 6-240-160 nm, respectively.	54
24. Calculated specular emittance (p-pol) for a Ag-Ge-Ag resonating structure at 294 K (left) and 500 K (right) between 2-20 μm . Thicknesses of constituent materials are 6-700-200 nm, respectively.	55
25. SEM micrograph of the top Ag surface of a Ag-Ge-Ag multilayer with thicknesses 6-700-200 nm, respectively. Ag and Ge layers were deposited via a High Power Impulse Magnetron Sputtering (HIPIMS) technique. Micrograph was taken at 45,000 \times magnification.	56
26. Spectral reflectance (p-pol) of a Ag-Ge-Ag truncated resonator (6-700-200 nm) between 1.7 and 29 μm . Reflectance measurements were taken using a J. A. Woollam Infrared Variable Angle Spectroscopic Ellipsometer (IR-VASE).	57
27. Spectral reflectance (p-pol) of a Ag-Ge-Ag truncated resonator (6-700-200 nm) between 1.7 and 15 μm . Reflectance measurements were taken using the J. A. Woollam Infrared Variable Angle Spectroscopic Ellipsometer (IR-VASE).	58
28. Comparison (p-pol) between the theoretical emittance results (left) and experimental emittance results (right) found through measurements taken using a J. A. Woollam Infrared Variable Angle Spectroscopic Ellipsometer (IR-VASE) for a Ag-Ge-Ag resonating structure with thicknesses 6-700-200 nm, respectively.	59
29. Screen capture from the J. A. Woollam VASE32 software of a modeled multilayer structure with associated thicknesses.	60
30. Amplitude ratio Ψ (green) and phase difference Δ (blue) ellipsometric measurements made using a J. A. Woollam Infrared Variable Angle Spectroscopic Ellipsometer (IR-VASE) on a Ag-Ge-Ag truncated resonator, Sample 1 (6-240-160 nm), with associated model fits (red).....	61

Figures	Page
31. Calculated complex index of refraction, n (red) and k (green), for a Ag layer deposited via a High Power Impulse Magnetron Sputtering (HIPIMS) technique.....	62
32. Calculated complex index of refraction, n (red) and k (green), for a Ge layer deposited via a High Power Impulse Magnetron Sputtering (HIPIMS) technique.....	62
33. The real part of the index of refraction (n) for HIPIMS-deposited Ag compared with bulk optical constants reported in Palik [44] over IR wavelengths.	63
34. The imaginary part of the index of refraction (k) for HIPIMS-deposited Ag compared with bulk optical constants reported in Palik [44] over IR wavelengths.	64
35. The real part of the index of refraction (n) for HIPIMS-deposited Ge compared with bulk optical constants reported in Palik [44] over IR wavelengths.	64
36. The imaginary part of the index of refraction (k) for HIPIMS-deposited Ge compared with bulk optical constants reported in Palik [44] over IR wavelengths.	65
37. Comparison (p-pol) between new theoretical emittance predictions that include derived optical constants (n and k) for the HIPIMS-deposited materials (left) to those calculated (right) from measurements taken using a J. A. Woollam Infrared Variable Angle Spectroscopic Ellipsometer (IR-VASE) for a Ag-Ge-Ag resonating structure with thicknesses 6-240-160 nm, respectively.	66
38. Comparison (p-pol) between new theoretical emittance predictions that include derived optical constants (n and k) for the HIPIMS-deposited materials (left) to those calculated (right) from measurements taken using a J. A. Woollam Infrared Variable Angle Spectroscopic Ellipsometer (IR-VASE) for a Ag-Ge-Ag resonating structure with thicknesses 6-700-200 nm, respectively.	67
39. Spectral radiance measured by a MR-154 Bomem Fourier transform infrared (FTIR) spectrometer for Ag-Ge-Ag truncated resonator, Sample 2 (6-700-200 nm), at room temperature (297 K) overlaid with the theoretical radiance of an ideal blackbody also at 297 K.	68
40. Spectral radiance measured by a MR-154 Bomem Fourier transform infrared (FTIR) spectrometer for Ag-Ge-Ag truncated resonator, Sample 2 (6-700-200 nm), at 408 K overlaid with the theoretical radiance of an ideal blackbody also at 408 K.	69

Figures	Page
41. Spectral radiance measured by a MR-154 Bomem Fourier transform infrared (FTIR) spectrometer for Ag-Ge-Ag truncated resonator, Sample 2 (6-700-200 nm), at 473 K overlaid with the theoretical radiance of an ideal blackbody also at 473 K.	70
42. Spectral radiance measured by a MR-154 Bomem Fourier transform infrared (FTIR) spectrometer for Ag-Ge-Ag truncated resonator, Sample 2 (6-700-200 nm), at 601 K overlaid with the theoretical radiance of an ideal blackbody also at 601 K.	71
43. Calculated emittance results for Ag-Ge-Ag truncated resonator, Sample 2 (6-700-200 nm), from two data sets, one was calculated from reflectance measurements and invoking Kirchhoff's law to assume that the radiation selectively absorbed by Sample 2 at room temperature (297 K) is also selectively emitted (blue), and the other data set represents the calculated emittance derived from radiance measurements of Sample 2 while thermally excited to 408 K (red).	72
44. Calculated emittance results for Ag-Ge-Ag truncated resonator, Sample 2 (6-700-200 nm), from two data sets, one was calculated from reflectance measurements and invoking Kirchhoff's law to assume that the radiation selectively absorbed by Sample 2 at room temperature (297 K) is selectively emitted (blue), and the other data set represents the calculated emittance derived from radiance measurements of Sample 2 while thermally excited to 473 K (red).	73
45. Calculated emittance results for Ag-Ge-Ag truncated resonator, Sample 2 (6-700-200 nm), from two data sets, one was calculated from reflectance measurements and invoking Kirchhoff's law to assume that the radiation selectively absorbed by Sample 2 at room temperature (297 K) is selectively emitted (blue), and the other data set represents the calculated emittance derived from radiance measurements of Sample 2 while thermally excited to 601 K (red).	74
46. SEM micrograph of a Ag-Ge-Ag truncated resonator (6-240-160 nm) on a silicon substrate after being thermally excited to 408 K. Ag and Ge layers were deposited via a High Power Impulse Magnetron Sputtering (HIPIMS) technique. Micrograph was taken at 100,000× magnification and at an angle of 35° from surface normal.	75
47. Measured spectral reflectance (p-pol) of a Ag-Ge-Ag truncated resonator (6-240-160 nm) between 1.7 and 6 μm and in 10° increments between 25-75° of incident angle before (blue) and after (red) being thermally excited to 408 K. Reflectance measurements were taken using the J. A. Woollam Infrared Variable Angle Spectroscopic Ellipsometer (IR-VASE).	76

Figures	Page
48. SEM micrograph of a Ag-Ge-Ag truncated resonator (6-700-200 nm) on a silicon substrate after being thermally excited to 601 K. Ag and Ge layers were deposited via a High Power Impulse Magnetron Sputtering (HIPIMS) technique. Micrograph was taken at 50,000× magnification and at an angle of 35° from surface normal.....	77
49. Measured spectral reflectance (p-pol) of a Ag-Ge-Ag truncated resonator (6-700-200 nm) between 1.7 and 15 μm and in 10° increments between 25-75° of incident angle before (blue) and after (red) being thermally excited to 601 K. Reflectance measurements were taken using the J. A. Woollam Infrared Variable Angle Spectroscopic Ellipsometer (IR-VASE).	78
50. Calculated emittance results for Ag-Ge-Ag truncated resonator, Sample 2 (6-700-200 nm), from three data sets – two data sets were calculated from reflectance measurements before (blue) and after (green) being thermally excited to 601 K and invoking Kirchhoff’s law to assume that the radiation selectively absorbed by Sample 2 at room temperature (297 K) is selectively emitted, and the last data set represents the calculated emittance derived from radiance measurements of Sample 2 while thermally excited to 601 K (red).....	79
51. CST simulated reflectance at normal incidence for a Ag-Ge-Ag (6-240-160 nm) hole array structure (red) using optical constants from literature (Palik) and a single Ag (400 nm) slab hole array structure (green) using the default Ag from the CST material library.	83
52. Illustration of one unit cell of the PC-multilayer structure as constructed in the CST simulation environment. The Ag slab with hole at its center is highlighted on the left with a transparent Si substrate behind it. On the right, the Si substrate is highlighted behind the transparent Ag layer.	84
53. Illustration of the periodic boundary conditions implemented on the hybrid photonic crystal-multilayer in CST (left) and the respective coordinate system superimposed over one unit cell (right).	85
54. Simulated spectral reflectance and transmittance from the hybrid photonic crystal-multilayer for θ from 0-60° from a p-pol (TM) plane wave incident at $\phi = 0^\circ$	86
55. Simulated spectral reflectance and transmittance from the hybrid photonic crystal-multilayer for θ from 0-60° from a s-pol (TE) plane wave incident at $\phi = 0^\circ$	86

Figures	Page
56. Simulated spectral reflectance and transmittance from the hybrid photonic crystal-multilayer for θ from 0-60° from a p-pol (TM) plane wave incident at $\phi = 45^\circ$	88
57. Simulated spectral reflectance and transmittance from the hybrid photonic crystal-multilayer for θ from 0-60° from a s-pol (TE) plane wave incident at $\phi = 45^\circ$	88
58. SEM micrograph of a hybrid photonic crystal-multilayer (Ag-Ge-Ag) on a silicon substrate. Ag and Ge layers were deposited via a High Power Impulse Magnetron Sputtering (HIPIMS) technique with dimensions 6-240-160 nm. The hole array was milled into the multilayer using focused ion beam (FIB) milling. Micrograph was taken from surface normal.	90
59. SEM micrograph of a hybrid photonic crystal-multilayer (Ag-Ge-Ag) on a silicon substrate. Ag and Ge layers were deposited via a High Power Impulse Magnetron Sputtering (HIPIMS) technique with dimensions 6-240-160 nm. The hole array was milled into the multilayer using focused ion beam (FIB) milling. Micrograph was taken at an angle of 52° from surface normal.	91
60. SEM micrograph of a hybrid hole array/multilayer (Ag-Ge-Ag) on a silicon substrate. Ag and Ge layers were deposited via a High Power Impulse Magnetron Sputtering (HIPIMS) technique with dimensions 6-240-160 nm. The hole array was milled into the multilayer using focused ion beam (FIB) milling. Micrograph was taken at an angle of 52° from surface normal.	92
61. Illustration of a photonic crystal-multilayer hybrid structure constructed of a square array of circular holes embedded inside of a multilayer with 3- μ m diameters and 6- μ m periods View is from surface normal of the structure.	93
62. Picture taken with a digital camera of a hybrid photonic crystal-multilayer structure embedded immediately to the right of a black ink dot. Total array size is 1.61 mm \times 113.33 μ m. The Ge-Ag-Ge-Ag (4-12-270-200 nm) multilayer was deposited on a Si substrate. The square array of circular holes was milled into the multilayer using a focused ion beam (FIB) system.	94

Figures	Page
63. SEM micrograph at 50× magnification of a hybrid photonic crystal-multilayer structure embedded immediately to the right of a black ink dot. Total array size is 1.61 mm × 113.33 μm. The Ge-Ag-Ge-Ag (4-12-270-200 nm) multilayer was deposited on a Si substrate. The square array of circular holes was milled into the multilayer using a focused ion beam (FIB) system.....	95
64. SEM micrograph of the center of a hybrid photonic crystal-multilayer structure at 750× magnification. The Ge-Ag-Ge-Ag (4-12-270-200 nm) multilayer was deposited on a Si substrate. The square array of circular holes was milled into the multilayer using a focused ion beam (FIB) system.	96
65. SEM micrograph of the center of a hybrid photonic crystal-multilayer structure at 5000× magnification. The Ge-Ag-Ge-Ag (4-12-270-200 nm) multilayer was deposited on a Si substrate. The square array of circular holes was milled into the multilayer using a focused ion beam system.	97
66. Illustration of a template-based nanofabrication approach that is capable of producing robust, large-scale samples with simple, repeatable, and low-cost execution.	104
67. Image of planar 3-D unit cell constructed in CST.	109
68. The final arrayed pattern (simulated in CST) shown next to same pattern with Zygo images overlaid in front of the respective areas where the pictures were taken.	110
69. Zygo images of fabricated 2×2 array using a Nanoscribe 3-D laser lithography tool. Patterned array was exposed in Nanoscribe IP-L photoresist on a glass substrate.....	111
70. Transmittance baseline of the ambient environment captured by the J. A. Woollam Infrared Variable Angle Spectroscopic Ellipsometer (IR-VASE).....	114
71. Spectral transmittance of a p-type silicon (Si) wafer measured using the Air Force Research Laboratory's (AFRL) J. A. Woollam Infrared Variable Angle Spectroscopic Ellipsometer (IR-VASE)	115
72. A comparison between a fitted model and spectral transmittance of a p-type silicon (Si) wafer. The model was fit using material constants from J. A. Woollam's infrared material library. The transmittance was measured using a J. A. Woollam Infrared Variable Angle Spectroscopic Ellipsometer (IR-VASE).	116

Figures	Page
73. Measured and generated ellipsometry data of a silicon substrate (p-doped) at visible and near-infrared wavelengths. Measured data captured using a J. A. Woollam Visible Variable Angle Spectroscopic Ellipsometer (V-VASE). Fitted model data was generated using J. A. Woollam WVASE23 software.	117
74. Measured and generated amplitude ratio Ψ data of a silicon substrate (p-doped) at mid-infrared wavelengths. Measured data was captured using a J. A. Woollam Infrared Variable Angle Spectroscopic Ellipsometer (IR-VASE). Fitted model data was generated using J. A. Woollam WVASE23 software.	118
75. Measured and generated phase difference Δ data of a silicon substrate (p-doped) at mid-infrared wavelengths. Measured data was captured using a J. A. Woollam Infrared Variable Angle Spectroscopic Ellipsometer (IR-VASE). Fitted model data was generated using J. A. Woollam WVASE23 software.	118
76. General Oscillator parameters used to model native silicon oxide layer (SiO ₂) using Air Force Research Laboratory's (AFRL) J. A. Woollam Infrared – Variable Angle Spectroscopic Ellipsometer (IR-VASE).....	119
77. Optical constants for Si wafer derived from measured ellipsometric data between 2-15 μm . Measured data was captured using a J. A. Woollam Infrared Variable Angle Spectroscopic Ellipsometer (IR-VASE).....	120
78. Optical constants for a SiO ₂ passivation layer derived from measured ellipsometric data between 2-15 μm . Measured data was captured using a J. A. Woollam Infrared Variable Angle Spectroscopic Ellipsometer (IR-VASE).....	120

List of Tables

Tables	Page
1. Electrical and Thermal Properties of Crystalline Germanium (Ge).	29
2. Electrical and Thermal Properties of Bulk Silver (Ag).	32

List of Symbols

Symbol	
$^{\circ}$	Degree(s)
Ψ	Amplitude Ratio
Δ	Phase Difference
θ	Incident Zenith
ϕ	Incident Azimuth
α	Absorptance, Attenuation Constant
μ	Permeability
ε	Permittivity, Emittance
a	Period of Unit Cell
d	Diameter of Hole
$\Phi_{incident}$	Incident Energy
$\Phi_{reflected}$	Reflected Energy
$\Phi_{absorbed}$	Absorbed Energy
$\Phi_{transmitted}$	Transmitted Energy
ρ	Reflectance
τ	Transmittance
L_{λ}	Spectral Radiance
T	Temperature
h	Planck's Constant

c	Speed of Light in Vacuum
λ	Wavelength
k	Boltzmann's Constant
\vec{E}	Electric Field
\vec{M}_i	Impressed Magnetic Current Density
\vec{B}	Magnetic Flux Density
\vec{H}	Magnetic Field
\vec{J}_i	Impressed Electric Current Density
\vec{J}_c	Conduction Electric Current Density
\vec{D}	Electric Flux Density
q_{ev}	Electric Charge Density
q_{mv}	Magnetic Charge Density
z	Distance to Interface
n	Real Part of Refractive Index
k	Imaginary Part of Refractive Index, or Extinction Coefficient
ω	Angular Frequency
ω_p	Plasma Frequency
ω_c	Electron Collision Frequency
\vec{k}	Direction of Propagation
\vec{r}	Position Vector

ϵ_1	Real Part of Complex Dielectric Constant
ϵ_2	Imaginary Part of Complex Dielectric Constant
®	Registered Trademark
Ag	Silver
Al	Aluminum
Au	Gold
C	Celsius
CO ₂	Carbon Dioxide
Cu	Copper
Ge	Germanium
K	Kelvin
K	Potassium
Na	Sodium
O ₃	Tri-Oxide
Si	Silicon
SiO ₂	Silicon Dioxide
<i>sr</i>	Steradian
W	Tungsten

List of Abbreviations

Abbreviation

1-D	One-Dimensional
2-D	Two-Dimensional
AFIT	Air Force Institute of Technology
AFRL	Air Force Research Laboratory
AR	Anti-Reflective
BRDF	Bi-Directional Reflectance Distribution Function
BSDF	Bi-Directional Scatter Distribution Function
BTDF	Bi-Directional Transmittance Function
cm	Centimeters
CASI	Complete Angle Scatter Instrument
CST	Computer Simulation Technology
DRIE	Deep Reactive Ion Etching
eV	Electron Volt
far-IR	Far-Infrared
FDFD	Finite Difference Frequency Domain
FDT	Fluctuation-Dissipation Theorem
FDTD	Finite Difference Time Domain
FEM	Finite Elements Method xxi
FEM-TD	Finite Elements Method in Time Domain
FIB	Focused Ion Beam
FIT-TD	Finite Integral Technique in Time Domain

FMM	Fourier Modal Method
FOV	Field Of View
FTIR	Fourier Transform Infrared spectrometer
FVTD	Finite Volume Time Domain
HgCdTe	Mercury Cadmium Telluride
HIPIMS	High Impulse Power Magnetron Sputtering
InSb	Indium Antimonide
IR-VASE	Infrared Variable Angle Spectroscopic Ellipsometer
MCF	Material Characterization Facility
mid-IR	Middle-Infrared
mm	Millimeter
nA	Nanoamps
NIL	Nano-Imprint Lithography
PC	Photonic Crystal
PEC	Perfect Electric Conductor
PMMA	Poly(methyl methacrylate)
RCWA	Rigorous Coupled Wave Analysis
RIE	Reactive Ion Etching
RF	Radio Frequency xxii
RMS	Root Mean Square
SEM	Scanning Electron Microscope
SMS	Schmitt Measurement Services
TE	Transverse Electric

TM	Transverse Magnetic
μm	Micrometer, or Micron
p-pol	P-polarized
s-pol	S-polarized

SPECTRAL AND SPATIAL COHERENT EMISSION OF THERMAL RADIATION FROM METAL-SEMICONDUCTOR NANOSTRUCTURES

I. Introduction

General Issue

Thermal energy transfer consists of three modes of transport — conduction, convection, and radiation. Conduction is due to a temperature gradient within and between matter leading to the transfer of thermal energy. It occurs when adjacent molecules vibrate against one another, or as free electrons move between neighboring molecules.

Convection is similar to conduction in that thermal energy is transferred between material mediums but different because it requires a dynamic environment, such as air or fluid flows. Thermal energy transport via convection depends on the physical properties in the immediate vicinity of the volume. Radiation encompasses thermal energy transport between bodies of matter without requiring an intermediate medium or direct contact.

Radiative properties of material surfaces, particles, and gases generally vary substantially over the electromagnetic spectrum. Thermal radiation covers wavelengths between 0.1-100 microns (μm) [1]. For most practical engineering problems, the most significant implications can be realized from the visible to far-infrared (far-IR) wavelength range between 0.4-30 μm , as defined by [2]. Moreover, the middle-IR (mid-IR) to far-IR wavelength range, from 3-30 μm as defined by [2], is where all finite

temperature biological materials and mechanical objects emit thermal radiation [3]. This frequency dependence is referred to as dispersion. To account for these dependencies, a rigorous formulation will be required that takes into account electrical and thermal properties of materials and the boundary conditions that separate these mediums. Further, the physical properties of a material can vary significantly with temperature. The resistivity of a material, and subsequently the electrical and thermal conductivity, will change as temperature decreases or increases. These changes in conductivity affect the electrical and thermal properties of matter to include a material's complex index of refraction. Therefore, a thorough understanding of the physical properties for a given material surface is needed to sufficiently predict and modify its radiative properties.

Radiative transfer constitutes the quantitative calculation of electromagnetic energy exchanged between objects [1]. The way this energy interacts with those objects largely depends on the characteristics of the source, medium, and the material properties of the object being illuminated. Thermal energy exchanges are generally described by the radiative transfer equation and the Planck blackbody distribution [1]. Radiation associated with a heated body is described as an example of incoherent radiation, both spectrally and spatially, where thermal energy transport is conceptualized as a particle. However, several recent experiments have experimentally demonstrated coherence properties associated with thermal radiation. The discovery of new properties, such as coherence from thermally excited surface waves, associated with thermal radiation is partly due to new developments in experimental techniques that allow one to directly observe the near-fields [4].

The study of surface waves is commonly referred to today as *plasmonics*. This topic has been around for a hundred years, dating back to the early 1900s. Back then, much of the analytical computations were based on Rayleigh's work on diffraction, and Zenneck's and Sommerfeld's work on surface waves [5]. Today, plasmonics encompasses a large part of the field of nanophotonics. Further, the idea of using thermally generated surface waves to create resonant effects in the near-field is a recent advancement and shows promise in uncovering more properties not previously demonstrated in the past [4]. This recent development has inspired new designs for selective thermal emitters and other thermally pumped optical devices. The utilization of thermally excited surface waves for coherent thermal radiation allows one to further exploit surface wave phenomena, and offers a new context for the application of plasmonics.

One of the ways to take advantage of plasmonics and coherently affect the radiative properties of a surface is through micro- and nano-scale structuring of a surface or of the bulk of a material. Layered media, where two or more different materials are layered together, is one example of altering the composition of a surface along one dimension to modify its radiative qualities [6-13]. Photonic crystals (PC) are another example where engineered structures whose material properties vary periodically in one, two, or all three dimensions result in unique optical properties absent or seldom found in nature [9, 14-22]. Metamaterials are another category of engineered structures that have generated a lot of attention due to their seemingly unnatural transmissive and reflective properties [23-27]. However, much of the research and literature on metamaterials focuses on radiative characteristics at radio frequency (RF) wavelengths. This is due to

readily available and mature fabrication techniques, as well as affordable implementation. Less research has been accomplished at optical frequencies primarily due to the increased difficulty in fabrication at micrometer (μm) and nanometer (nm) scales. An even smaller fraction of this research has been focused on thermal radiative properties that take advantage of thermally excited surface waves [3, 10, 16, 28-31].

Problem Statement

In this thesis, the ability to selectively affect the thermal radiative properties of a surface, both spectrally and directionally, through the use of micro- and nano-structured materials will be designed for and demonstrated experimentally. Polarization and angular sensitivities to incident light at room temperature will be investigated. In addition, the effects of thermally excited surface waves on spectral emittance will be determined over mid- and far-IR wavelengths, from 3-19 μm as defined by [2], while each sample is heated to various high temperatures.

Methodology

Design of the photonic nanostructures in this work will involve modern modeling and simulation techniques to help complement rigorous analytical calculations, where applicable. Two thermal emitter designs will be proposed, fabricated, and experimentally analyzed – a 1-D multilayer resonator and a 3-D hybrid PC-multilayer, or PC-multilayer for short. Rigorous analytical solutions, complemented by Computer Simulation Technology (CST) electromagnetic modeling software, will be used for the design of the multilayer structure. For the 3-D hybrid structure, computer simulations through CST

will be utilized for this more complex geometrical problem where a PC hole array will be embedded inside a multilayer.

Upon completion of the analytical design, fabrication efforts will be accomplished using Air Force Research Laboratory (AFRL) facilities and resources. The multilayer design will use a High Impulse Power Magnetron Sputtering (HIPIMS) deposition technique to deposit the constituent materials. Fabrication of the hybrid PC-multilayer will involve both the HIPIMS deposition and a focused ion beam (FIB) milling tool. Tools such as a scanning electron microscope (SEM), Zygo Interferometer, and Zeiss optical microscope will be used to continually verify that fabricated structures meet design specifications.

Reflectance measurements will be taken using a J. A. Woollam Infrared-Variable Angle Spectroscopic Ellipsometer (IR-VASE) to characterize how light is scattered at various IR wavelengths. The IR-VASE can also make spectroscopic ellipsometry measurements. Spectroscopic ellipsometry at room temperature will be used to verify layer thicknesses and derive the optical constants of the constituent materials. These optical constants will be compared to bulk material values found in literature and will help to understand the optical properties observed throughout this study.

Further, the samples will be thermally heated to spectrally analyze the angular emittance characteristics at various high temperatures. This will be accomplished by making IR radiance measurements using an in-house emissometer assembly and MR-154 Bomem Fourier Transform Infrared spectrometer (FTIR). Subsequently, spectral and angular emittance can be derived from these radiance measurements to investigate the

effect of thermally excited surface waves on the radiative properties of each plasmonic structure.

Implications/Applications

Many applications can benefit from research in thermal radiation modification. Most notably, significant implications are possible for solar cell technology, solar energy harvesting, and solar absorbers/reflectors. The anti-reflective (AR) coating industry can benefit from frequency selective films that help eliminate unwanted reflections. These AR coatings have applications in products ranging from optical components in a laboratory, to displays on flat-screen monitors and cell-phones.

Thermal management applications can also be realized from radiative cooling of buildings to almost any electronic device requiring isolation or dissipation of thermal radiation. Having better thermal control of a building will save on energy costs. Overheating caused by thermal energy generation is a major source of device failure in the electronics domain. Also, since conductive and convective thermal energy transport is not possible in a space environment, thermal management problems on space vehicles, where radiative cooling is dominant, can directly benefit from this research.

Preview

Chapter II will provide a general theoretical background on key topics to be discussed in later chapters. Chapter III discusses relevant citations pointing to past works and recent literature, where appropriate. Chapter IV describes the methodology used in designing, fabricating, and characterizing both plasmonic nanostructures — the multilayer resonator and hybrid PC-multilayer. Chapter V discusses the measurements captured and analyzes

the implications of the observed data. Chapter VI summarizes the findings of this study and makes recommendations for future research opportunities. Appendix A discusses initial fabrication results for a 3-D laser lithography tool pursued during the course of this thesis and other nanofabrication topics. Appendix B presents supplemental IR-VASE measurements and modeling results.

II. Theoretical Background

Chapter Overview

This chapter provides a broad theoretical background on conservation of energy, electromagnetic theory, thermal radiation, and surface waves. Relevant citations have been provided to supplement a given discussion or offer a resource for a more detailed development of a specific topic.

Conventions

Due to a multitude of nomenclature and convention variations found in literature, a few assumptions are made here for clarity. Following the Fresnel convention [32], reflection and transmission will be viewed as general processes, while the numerical measurements made on a sample will be referred to as the reflectance and transmittance, respectively. Emittance is the ratio between the exitance of an actual source, and the exitance of a blackbody at the same temperature. The distinction between “emittance” and “emissivity” is not always clear, and both are used interchangeably in literature [33]. For consistency, the term “emittance” will be used throughout this work.

In addition, a distinction between transverse electric (TE) and transverse magnetic (TM) linear polarizations is in order. In electromagnetics, TE waves refer to field configurations whose electric field components are transverse to a given direction, typically chosen as the direction of propagation. Similarly, TM waves would have magnetic field components transverse to a chosen direction [34]. In physics, a Fresnel convention is commonly used where a TE wave refers to a field configuration where the electric field components are orthogonal to the plane of incidence [32]. Thus, the TM

wave would have its electric field components parallel to the plane of incidence. To avoid confusion, the Fresnel convention for linearly-polarized waves will be assumed in this thesis.

Conservation of Energy and Kirchhoff's Law

On a macroscopic level, energy is always conserved. Assuming that a surface is in thermal equilibrium with its environment, conservation of energy requires that the incident energy ($\Phi_{incident}$) be either reflected ($\Phi_{reflected}$), absorbed ($\Phi_{absorbed}$), or transmitted ($\Phi_{transmitted}$):

$$\Phi_{incident} = \Phi_{reflected} + \Phi_{absorbed} + \Phi_{transmitted} \quad (1)$$

Dividing both sides of the equation by $\Phi_{incident}$ results in

$$1 = \rho + \alpha + \tau \quad (2)$$

where ρ is the reflectance, α is the absorptance, and τ is the transmittance. For an opaque surface, no transmitted radiation is expected in theory. Therefore, τ is equal to zero resulting in

$$1 = \rho + \alpha \quad (3)$$

According to Kirchhoff's law, in thermal equilibrium, the emittance ε is equal to the absorptance α , yielding the following equation for emittance

$$\varepsilon = 1 - \rho \quad (4)$$

In the far-field regime, a blackbody source follows a Planckian distribution, providing an upper limit of the overall spectral exitance of a source in thermal equilibrium at a given temperature. Exitance is the amount of power per unit area that leaves a surface. The actual exitance or radiance curve for a real thermal source will be bounded by the corresponding theoretical limit of a Planckian distribution at the source temperature. Radiance is another radiometric quantity that is bounded by this theoretical limit and can also be used to describe a thermal source. Radiance L_λ is the amount of power radiated per unit projected source area, per unit solid angle leaving a surface

$$L_\lambda(\theta, \phi, T) = \frac{2hc^2}{\lambda^5 (e^{hc/\lambda kT} - 1)} \left[\frac{\text{watt}}{\text{cm}^2 - \text{sr} - \mu\text{m}} \right], \quad (5)$$

where θ is the incident zenith, ϕ is the incident azimuth, T is the source temperature, h is Planck's constant, c is the speed of light in vacuum, λ is the wavelength, and k is Boltzmann's constant. The behavior of this radiation spectrum and relationship to a blackbody can be partly described by the source's emittance ε . The formal definition of emittance is a ratio between the exitance, or radiance, of the actual source and that of a blackbody at the same temperature [2]. Thus, emittance is always less than one for actual thermal sources and can be defined as follows for a given solid angle

$$\varepsilon_\lambda(\theta, \phi, T) = \frac{L_\lambda(\theta, \phi, T)}{L_{bb}(\lambda, T_{bb})} \quad (6)$$

where L_λ is the source radiance, L_{bb} is the blackbody radiance, λ is the wavelength, T is the source temperature, and θ and ϕ describe the direction of propagation of radiation with respect to the surface normal as illustrated in Figure 1. A blackbody source will

always have an emittance $\varepsilon = 1$ for all wavelengths. A selective radiator is a source whose emittance will vary spectrally.

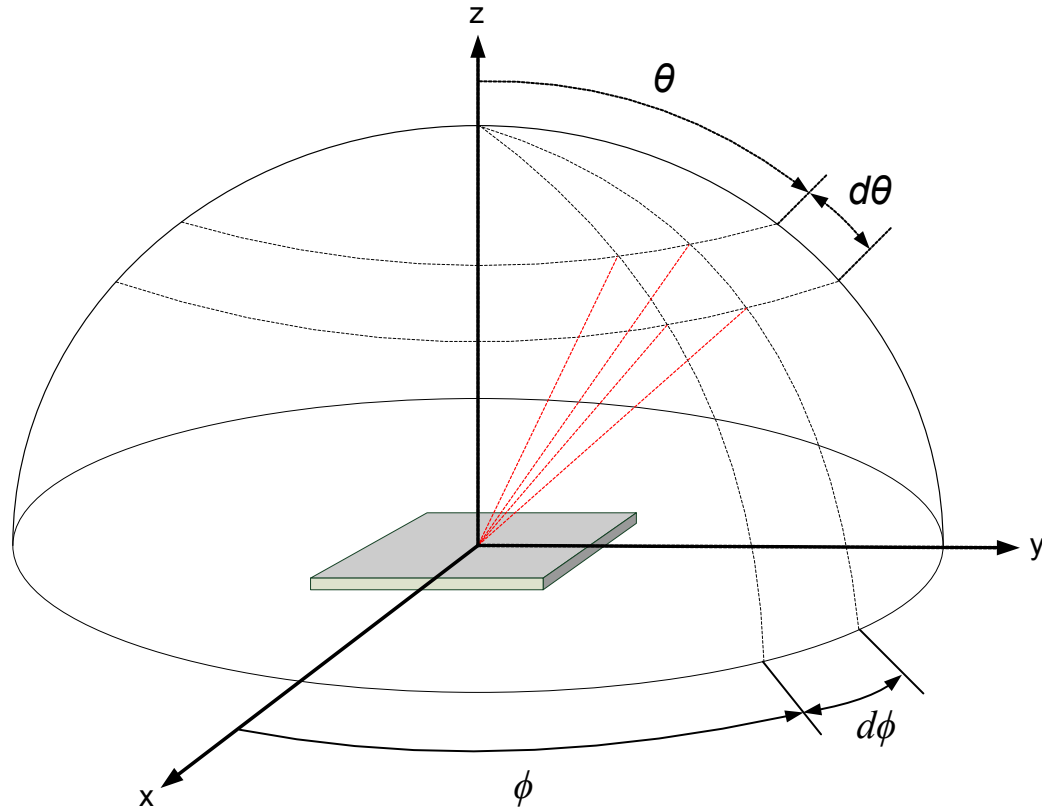


Figure 1. Illustration of the direction of propagation of radiation being emitted from a surface in spherical coordinates. Both θ and ϕ are measured with respect to the local coordinate system constructed from the surface normal.

Electromagnetic Theory and Constitutive Relations

When looking at small distances away from a source with respect to wavelength or when the feature sizes of a structure are on the order of, or smaller than, a wavelength, conventional electromagnetic theory can be applied and observed near the boundary conditions of a given problem. This zone is commonly referred to as the near-field, or

near-zone, and can be quantified to within an order of magnitude, or less, of the design wavelength. When the distance away from a source is much greater than a wavelength, or the feature sizes of a structure are much larger than a wavelength, namely when looking at sizes greater than $\frac{(distance)^2}{\lambda}$, thermal energy exchanges are typically described by the radiative transfer equation and the blackbody Planckian distribution where thermal energy transport is conceptualized as a particle, called a photon [1]. This regime is commonly known as the far-field, or far-zone.

In the far-field, thermal radiation is traditionally considered spectrally and spatially incoherent. In contrast, radiative transfer from laser radiation is considered coherent, and exhibits high directionality and quasi-monochromatic emission. However, coherent thermal emission was recently observed for the first time in the far-field by Greffet *et al.* [35] in 2002. Greffet *et al.* showed that angularly selective emission was possible by ruling a grating on a SiC substrate where surface waves could be supported and coupled to propagating modes observable in the far-field. To understand coherent thermal radiation and this coupling in the near-field, an electromagnetic approach is needed.

The theoretical concepts central to the study of electromagnetics are described by a set of basic laws (Faraday's law, Ampere's law, and Gauss' law, among others) that came about through experiment in the nineteenth century [34]. James Clerk Maxwell combined these original theoretical concepts into a set of equations that describe the physical laws that govern electromagnetic fields, both electric and magnetic. These equations are known as Maxwell's equations. In Maxwell's equations, the electric and

magnetic fields are described with vector quantities, having both magnitude and direction. The differential form of Maxwell's equations is shown here with fictitious magnetic sources, \vec{M}_i and q_{ev} , included [34].

Equation (7) was derived from Faraday's law with an added magnetic displacement current density $\partial\vec{B}/\partial t$ term introduced by Maxwell and can be written as

$$\nabla \times \vec{E} = -\vec{M}_i - \frac{\partial \vec{B}}{\partial t} \quad (7)$$

where \vec{E} is the electric field (volts/meter), \vec{M}_i is the impressed magnetic current density (volts/square meter), and \vec{B} is the magnetic flux density (webers/square meter).

Equation (8) was derived from Ampere's law and can be written as

$$\nabla \times \vec{H} = \vec{J}_i + \vec{J}_c - \frac{\partial \vec{D}}{\partial t} \quad (8)$$

where \vec{H} is the magnetic field (amperes/meter), \vec{J}_i is the impressed electric current density (amperes/square meter), \vec{J}_c is the conduction electric current density (amperes/square meter), and \vec{D} is the electric flux density (coulombs/square meter). The electric and magnetic field equations, shown in Equation (9) respectively, were derived from Gauss' law and can be written as

$$\begin{aligned} \nabla \cdot \vec{D} &= q_{ev} \\ \nabla \cdot \vec{B} &= q_{mv} \end{aligned} \quad (9)$$

where q_{ev} is the electric charge density (coulombs/cubic meter) and q_{mv} is the magnetic charge density (webers/cubic meter). The magnetic sources, \vec{M}_i and q_{ev} , are considered fictitious since they are not physically realizable but they provide a numerical balance for aiding in mathematical solutions to Maxwell's equations. A mode is a particular electromagnetic field configuration that is a solution to Maxwell's equations and associated boundary conditions. Typically, there are many field configurations that satisfy the conditions and these are usually referred to as modes [34].

When a material is subjected to electromagnetic fields, charged particles present in the material will interact with the electromagnetic field vectors. Two of the macroscopic constitutive relations that exist to account for this behavior involve the electric and magnetic flux densities, \vec{D} and \vec{B} , respectively. Assuming linear, homogeneous, and isotropic media, the electric and magnetic fields are related to the electric and magnetic flux densities by

$$\begin{aligned}\vec{D} &= \epsilon \vec{E} \\ \vec{B} &= \mu \vec{H}\end{aligned}\tag{10}$$

where ϵ is the permittivity and the μ is the permeability of the medium. These constitutive parameters are used to characterize the electrical properties of a material and are generally a function of the applied field strength, the position within the medium, the direction of the applied field, polarization, and the frequency of operation [34]. Furthermore, materials whose constitutive parameters are functions of frequency are referred to as dispersive. Dispersion is inherent in all real materials to some degree.

Thermal Radiation

Electromagnetic theory supplies a framework for determining the observed optical properties from surfaces of various materials. Understanding the wave nature of light becomes critical when considering radiative energy transfer at micro- and nano-scales, where the size of the structures is comparable to the wavelength. At these length scales, only through electromagnetic theory can polarization, coherence, and radiative energy transfer be considered in detail [1]. The idea of describing thermal radiation using electromagnetic theory dates back as far as the early 1900s, when Hendrik Lorentz derived the thermal radiation from a random current density in a series of conferences at Columbia University [4]. In the 1950s, Rytov developed electromagnetic models for thermal radiation that were analogous to the Langevin model of Brownian motion [36, 37]. These electromagnetic descriptions of thermal radiation were considered from a fluctuational electrodynamics point of view and link Maxwell's equations to thermal radiation emission. Fluctuational electrodynamics characterizes a thermal source using the fluctuation-dissipation theorem (FDT) where thermal radiation comes about from a superposition of contributions from fluctuating current densities at a given point in free space [33]. Subsequently, a finite spectrum is defined for a random current density that appears as a stochastic source in Maxwell's equations. Thus, FDT provides a bridge between electromagnetic theory and emission of thermal radiation which can be used to analytically verify coherent emission of thermally emitted fields. For more information on derivation and application of FDT, see [1, 29, 33, 37].

Surface Waves

In classical electromagnetic theory, surface waves do not propagate to the far-field because they are bound to interfaces. However, near-field energy transfer through these surface modes is possible given the right boundary conditions. This energy transfer has been referred to as “radiation tunneling” in some cases and leads to heat transfer in the near-field that exceeds that of a blackbody [1, 4]. Using structuring, the right boundary conditions can be introduced to couple the energy from surface waves in the near-field to the propagating radiation observed in the far-field.

Surface waves can be thought of as collective oscillations of electrons that introduce surface modes. These surface modes are evanescent and are typically neglected since their amplitude decreases away from the interface on wavelength scales. Surface waves that result from incident electromagnetic fields causing resonant polarization oscillations in the material are called surface polaritons [38]. At an interface with a dielectric, this is due to coupling of the electromagnetic fields with optical phonons and these resonant oscillations are known as *surface-phonon polaritons*. The optical properties of metals can be described by a plasma model where a free-electron gas is assumed against a fixed background of positive ion cores. Therefore, at an interface with a metal, coupling with the electromagnetic field results in plasma oscillations called *surface-plasmon polaritons*. In this section, surface-plasmon polaritons, or surface plasmons for short, propagating along a plane interface will be discussed.

Surface waves are captured in Maxwell’s equations where surface waves propagate along the interface with evanescent fields decaying exponentially into both mediums. Figure 2 shows a schematic representation of a surface wave at the interface

between a medium that supports surface waves, and a free-space medium. The wave amplitudes decay exponentially with distance from the interface with attenuation constant α and distance to the interface z , as shown in Figure 2.

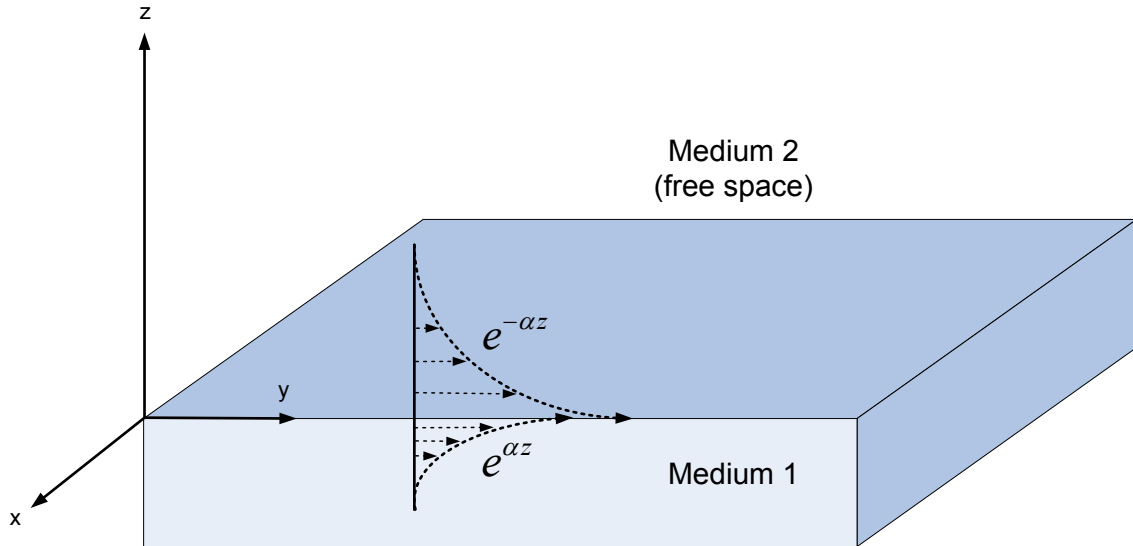


Figure 2. Schematic representation of a surface plasmon at the interface between a surface that supports surface waves (Medium 1) and free space (Medium 2). The wave amplitudes decay exponentially with distance from the interface with decay constant α and distance from the interface z .

TE and TM polarization states can exist for surface waves [39]. For TE (s-polarized or s-pol) surface waves, the electric field is perpendicular, or transverse, to the plane containing the interface. For a TM (p-polarized or p-pol) surface wave, the electric field is parallel to the plane containing the interface. Since non-magnetic materials are assumed at optical frequencies, TE-polarized surface waves are not supported [38]. A diagram of a TM surface wave supported by bare metal is shown in Figure 3.

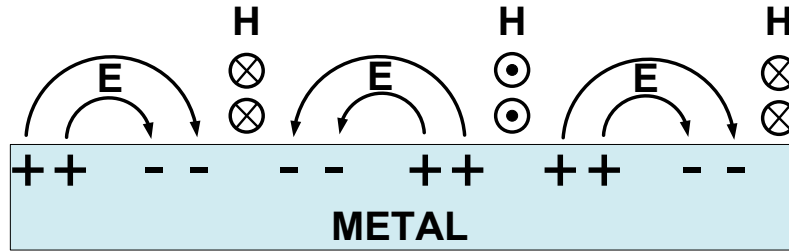


Figure 3. Illustration of a transverse magnetic (TM) surface wave on a bare metal interface.

Designing a Thermal Emitter

Designing selective thermal emitters is a multi-disciplinary problem. It requires knowledge in electromagnetics, thermodynamics, material science, electrodynamics, and mechanics. Multiphysics simulation programs such as COMSOL, CADFEM, and CST can be utilized to capture the numerous physical phenomena and their interactions to help complement an analytical development. The aforementioned programs have frequency domain solvers and utilize a numerical technique called the Finite Elements Method, or FEM. However, due to varying material and geometric properties in some electromagnetic problems, this may not be the most efficient method depending on a given material. For example, time-domain techniques such as Finite Difference Time Domain (FDTD), Finite Integral Technique in Time Domain, (FIT-TD), Finite Volume Time Domain (FVTD), and Finite Elements Method in Time Domain (FEM-TD) are preferred when dealing with non-linear materials [40]. In general, FDTD software programs like Lumerical are typically chosen for their relative simplicity and speed in calculation when it comes to non-linear materials, or more complex geometries [40]. Frequency domain methods, like Finite Difference Frequency Domain (FDFD), are typically not used unless material dispersion is strong. FDFD can also be utilized when

time domain methods become too expensive or inaccurate. The flagship of CST's many solvers is based on the Finite Integration Technique (FIT) but only CST's Frequency Domain solver is capable of illuminating and evaluating off-normal incident angles.

A rigorous analytical technique from first principles can also be used to design a thermal emitter. A transfer matrix method can be implemented by discretizing Maxwell's equations, but this approach is limited in that the initial excitation can only be monochromatic. Rigorous coupled-wave analysis (RCWA), also called the Fourier Modal Method (FMM), numerically solves for the diffraction of periodic structures but offers an efficient way to evaluate the electromagnetic fields over a wide angular range and spectral bandwidth. It is an exact solution of Maxwell's equations for the reflected and transmitted electromagnetic fields. A full derivation of the RCWA solutions, starting with Maxwell's equations, can be found in [41] and [42]. From these calculated fields, diffraction efficiencies by grating structures or uniform homogeneous multilayers can be derived. The RCWA method assumes ideal coherence and an infinitely periodic structure. This rigorous technique uses a layer-by-layer construct to effectively take 2-D slices of a given structure and approximate its geometric profile. The RCWA algorithm is widely used for its good convergence and simple implementation. The implementation used in this work follows a modified formulation of the RCWA algorithm introduced by Moharam and Gaylord (1986) [42] but leverages a numerical adaptation provided by Lifeng (1996) [43] that allows for faster convergence of the RCWA method.

Scatterometry

To gain physical insight into phenomena related to optical observables, scatterometry can be utilized. Optical scatterometry is a characterization technique that measures the directional scattered radiation from a surface. Surfaces such as those constructed of PCs or metamaterials can have unique optical properties seldom found in natural materials. The optical signatures measured will largely be determined by the characteristics of that unique surface, such as roughness, particulates, defects, and surface-bulk interactions. Traditionally, these measurements encompass both reflected and transmitted signatures with attention towards angle-of-incidence sensitivity.

Spectroscopic Ellipsometry

The technique used for material deposition has a significant impact on the optical constants of that material. Since all evaporated films are amorphous to some degree, the resulting microstructure of the material will affect the way light interacts with the material. Ellipsometry measures a change in polarization as light propagates through a material. As light becomes reflected, transmitted, or absorbed due to the material structure, the polarization change can be represented using two variables, the amplitude ratio Ψ and the phase difference Δ . The measured response of these variables depends on the optical properties and thickness of each individual material, to include the substrate for translucent structures. This technique can be used to not only extract the optical constants of a given material, but also to estimate the thicknesses of those material layers. For an in-depth discussion on determining optical properties by ellipsometry, see [44].

Summary

The presented background theory provides a basis for undertaking the design, fabrication, and characterization of infrared nanoplasmonic structures. Relevant publications were highlighted for further in-depth background into the subject matter. A look at recent literature in the next chapter will offer context to this research problem and provide a guide through previous investigations in this area.

III. Literature Review

The ability of complex media and metamaterials to coherently affect thermal radiative properties by means of thermally excited surface waves has only recently been explored within the last two decades. This is partly due to advancement in fabrication techniques and near-field thermal microscopy, leading to more investigations to further understand the influence of patterning at micro- and nano-scales on thermal radiative properties. The scope of this review encompasses those selective emitters that leverage the coherence properties of thermal radiation, and subsequently result in radiative transfer observed in the far-field.

Review Papers

Scklover *et al.* (2008) [45] extensively discusses many published high-temperature optical structure designs with an eye toward practical applications in environments of extreme temperature. In some cases, the optical structures were heated in excess of 1000 degrees (°) Celsius (C). A review published by Fu and Zhang (2009) [27] focused on thermal radiative properties of metamaterials and other nanostructured materials. Fu and Zhang were interested in these structures for applications in radiative energy transfer and energy conversion systems. Soukoulis and Wegener (2011) [26] describe past experimental achievements and discuss the future challenges associated with photonic metamaterials.

Relevant Research

Coherent thermal emission has been demonstrated from numerous types of structures of varying complexities. Planar multilayer structures, from a bi-layer to truncated PCs have been proposed [6-12, 14, 15]. Several authors have experimentally demonstrated coherent thermal emission from thermally excited surface waves using 3-D structures [3, 16, 18, 28, 29, 35, 46, 47]. Also, several discussions of surface plasmons at metal interfaces and in thin films can be found in [38, 48, 49].

Among the planar coherent thermal emitters mentioned above, the designs that were based on interference effects, versus thermally exciting surface waves, included Kollyukh *et al.*'s (2003) [50] parallel plate structure using semiconductors and various multilayer resonator designs with highly reflective coatings [9, 11, 12, 30, 51]. The majority of these multilayer resonator designs incorporated complex reflective layers consisting of Bragg reflectors or PCs [12, 30, 51]. The remaining two designs utilized a simple tri-layer structure using a metal as the reflecting boundaries of the resonant cavity [9, 11]. Of these simpler tri-layer designs, only one of these papers investigated angle-of-incidence and polarization sensitivities while considering a gold- silicon dioxide-gold (Au-SiO₂-Au) resonator [11]. Figure 4 shows the calculated angular emittance of a Au-SiO₂-Au tri-layer resonator for (a) TM- and (b) TE- polarized waves. Wang *et al* [11] did not thermally heat this structure.

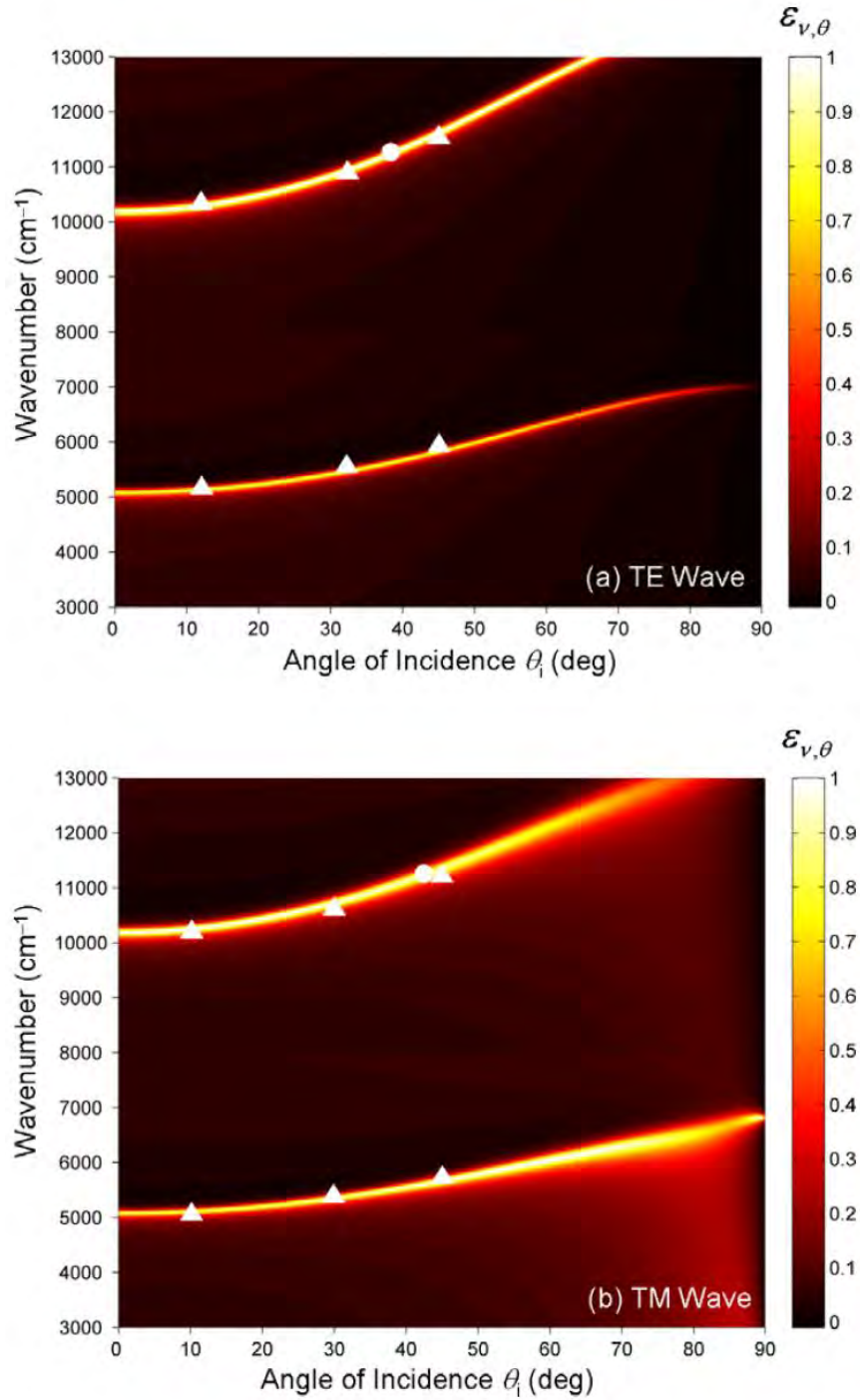


Figure 4. Calculated angular emittance of a Au-SiO₂-Au tri-layer resonator for (a) TM and (b) TE polarizations. The triangles and circles represent the measured reflectance dips obtained by an FTIR spectrometer and a laser scatterometer, respectively. From [11].

Both of the previous tri-layer designs used SiO₂ as the transparent medium between the reflective layers of the resonant cavity. However, their analysis and performance was limited to the near-IR (as defined by [2]) since the transmission range of the dielectric SiO₂ is limited to approximately 180 nm to 2.2 μm (3.5 μm for crystalline quartz). In this thesis, emission in the mid- to far-IR wavelength range will be designed for, requiring different materials to be considered and utilized. Furthermore, broader resonances are preferred for those applications where higher bandwidth is desired. Lastly, near-isotropic emission at specific design wavelengths, invariant to incident angles of radiation, will be investigated in this thesis.

Summary

This literature search is not meant to be an all-inclusive review but provides some background on earlier examinations into the design, fabrication, and characterization of high-temperature optical structures. The references to past and recent literature provide a guide through previous investigations in this area and offer context to this research problem. Given this perspective, the approach and processes chosen for further investigation of coherent thermal emission will be explained next.

IV. Methodology

Chapter Overview

The objectives of this study are to design, fabricate, and measure the performance of a nanostructured surface that acts as a selective emitter, both spectrally and directionally, at infrared wavelengths of interest when thermally excited. The mid-IR to far-IR wavelength band, from 2-30 μm , as defined by [2], is where all finite temperature biological materials and mechanical objects emit thermal radiation. Hence, mid-IR wavelengths were chosen as the design wavelengths of interest given their relevance in practical thermal radiation emission and detection problems. The thermal emitters were also expected to perform in a high temperature environment, up to 900 Kelvin (K), so the constituent materials were required to be thermally stable when heated. This made high melting points and thermally matched expansion coefficients between constituent materials necessary to prevent destruction and delamination of the samples. In addition, this work took an emphasis on robust designs that can be reproduced over large-scale surface areas.

The optical structures discussed here have scales of periodicity that are on the order of the design wavelength in the mid- to far-IR regime. The words “on the order of the design wavelength” are differentiated here to distinguish PC structures from metamaterials. The term “metamaterials” is reserved for nano-structured materials with sub-wavelength features that are less than 1/10 the design wavelength. This is done so that designed effects are not attributable to Bragg diffraction. However, note that not all research entities use this same demarcation in terminology.

Two thermal emitter designs are proposed in this work – a truncated multilayer resonator and a hybrid PC-multilayer. Technically, these structures would fall under the metamaterial umbrella owing to the sub-wavelength thicknesses of each material layer (sub-wavelength in 1-D). To avoid superfluous terminology, the word “metamaterial” will be left out for the remainder of this document. The methodology behind each of these thermal emitter designs is described below in detail with associated fabrication and characterization techniques.

Truncated Multilayer Resonator

The first thermal emitter design is a truncated resonator design based on a multilayer resonator. This planar structure was chosen for its relative ease in fabrication while still achieving coherent thermal radiative properties through wave interference effects. The resonant cavity is formed by sandwiching a transparent medium between two reflective mediums. One of the reflective mediums is optically thick, while the other is optically thin (thickness below intrinsic penetration depth). Figure 5 shows an illustration of a truncated multilayer resonator.

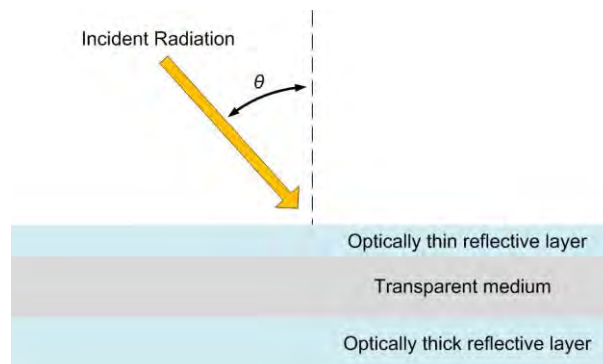


Figure 5. Illustration of a truncated multilayer resonator.

Constituent Material Properties

At optical frequencies, use of a lossy (high attenuation) metal like tungsten (W), although very appealing given its high melting point (~ 4000 K) and low thermal expansion coefficient, would have resulted in broader spectral resonances than those observed in low-loss metals such as silver (Ag) and Au. As previously mentioned, the material properties of dielectrics, semiconductors, and metals are temperature dependent. Optical properties of many materials are often not well characterized in literature, especially with respect to high temperatures. Often, different results are reported from different sources for the same material. Therefore, to account for these temperature sensitivities, two models will be used to predict the optical properties at temperatures at and above room temperature – a temperature-dependent Sellmeier equation and the free-electron/Drude model.

A semiconductor, germanium (Ge), was the material chosen for the transparent medium of the resonant cavity for its appealing inherent material properties and expected performance enhancement while operating at high temperatures. Germanium is a high refractive index semiconductor that is used in many infrared applications, from substrates for optical filters and lenses to attenuated total reflection prisms for spectroscopy [52]. Its transmission range is between 1.8 and 23 μm , minimizing attenuation of incident radiation in this medium. Representative values of thermal expansion, melting point, electrical conductivity, and thermal conductivity for crystalline Ge are given in Table 1.

Table 1. Electrical and Thermal Properties of Crystalline Germanium (Ge).

	Crystalline Germanium (Ge)
Thermal Expansion Coefficient (per K) [52]	6.1×10^{-6}
Melting Point (K)	1211
Electrical Conductivity (S/m) [34]	2.227
Thermal conductivity (Watts/m K) [52]	77

Since these thermal emitters would be tested at temperatures higher than room temperature (~294 K), temperature-dependent optical constants were desired for germanium. Barnes and Piltch (1979) [53] calculated temperature-dependent coefficients from accepted empirical optical constants for the Sellmeier equation

$$n^2(\lambda) = A + \frac{B\lambda^2}{(\lambda^2 - C)} + D\lambda^2(\lambda^2 - E), \quad (11)$$

where n is the real part of the refractive index, and A , B , C , D , and E are Sellmeier coefficients. Using temperature-dependent values of refractive index n , Barnes and Piltch calculated the following values for the Sellmeier coefficients:

$$\begin{aligned} A(T) &= -6.040 \times 10^{-3}T + 11.05128, \\ B(T) &= 9.295 \times 10^{-3}T + 4.00536, \\ C(T) &= -5.392 \times 10^{-4}T + 0.5999034, \\ D(T) &= 4.151 \times 10^{-4}T + 0.09145, \\ E(T) &= 1.51408T + 3426.5. \end{aligned} \quad (12)$$

Potter (1985) [54] evaluated the Sellmeier equation at room temperature (291 K) over a large range of infrared wavelengths and these data can be found in Palik's *Handbook of Optical Constants for Solids* (1985) [44].

Figure 6 compares the calculated refractive index for Ge found using the Sellmeier equation at 294 K, 500 K, and 1000 K along with the measured refractive index

values published by Li (1980) [55] for intrinsic Ge at 500 K. The measured and modeled refractive index values for Ge at 500 K are observed to be in close agreement with an average root mean square (RMS) of 0.0057.

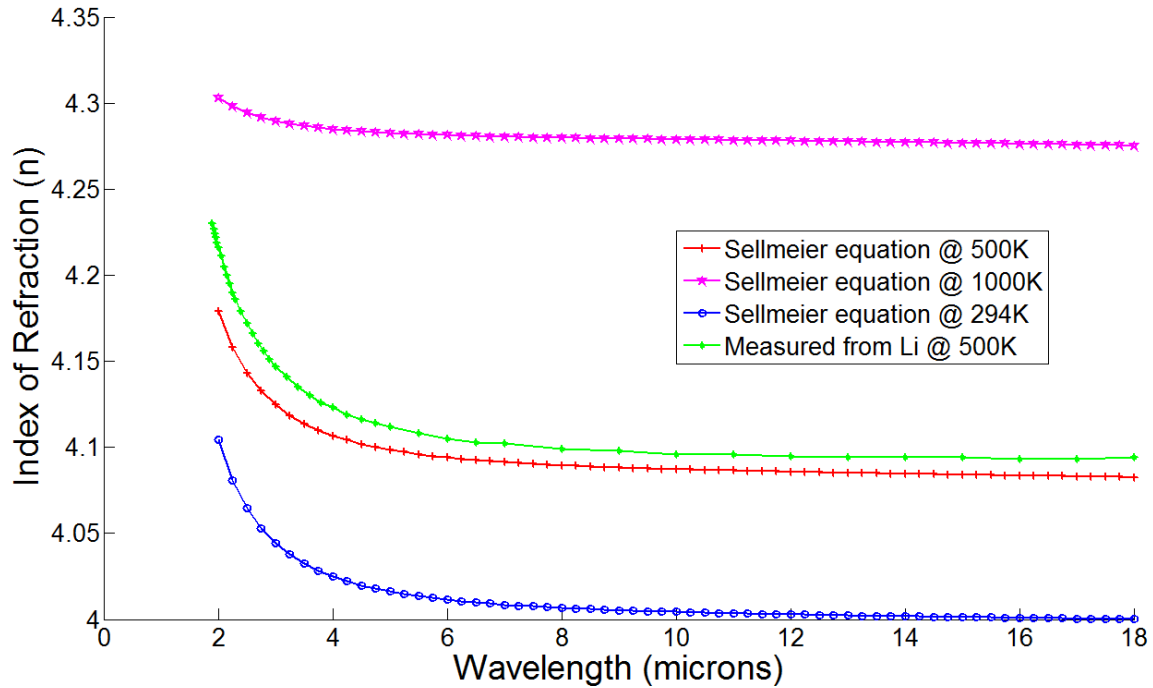


Figure 6. Index of refraction for Germanium using a temperature-dependent Sellmeier equation versus measured values reported by Li [55].

Silver, exhibiting the highest electrical and thermal conductivities of all metals, was chosen for the reflective layers of the resonator. High reflectivity is desired for sharp spectral responses of the cavity. However, reflectivity of metals in the IR wavelength range is a decreasing function of temperature [18, 30, 56]. The reduction of reflectivity as temperature rises is lower at longer wavelengths (2% for aluminum, 10.6 μm , 925 K). At shorter wavelengths, reflectivity could reduce by as much as 30% (aluminum, 0.69 μm , 925 K) depending on the metal and the temperature [56]. The reduction in

reflectivity with rising temperature at 0.69 and 10.6 μm for Ag, Au, sodium (Na), copper (Cu), potassium (K), and aluminum (Al) is shown in Figure 7.

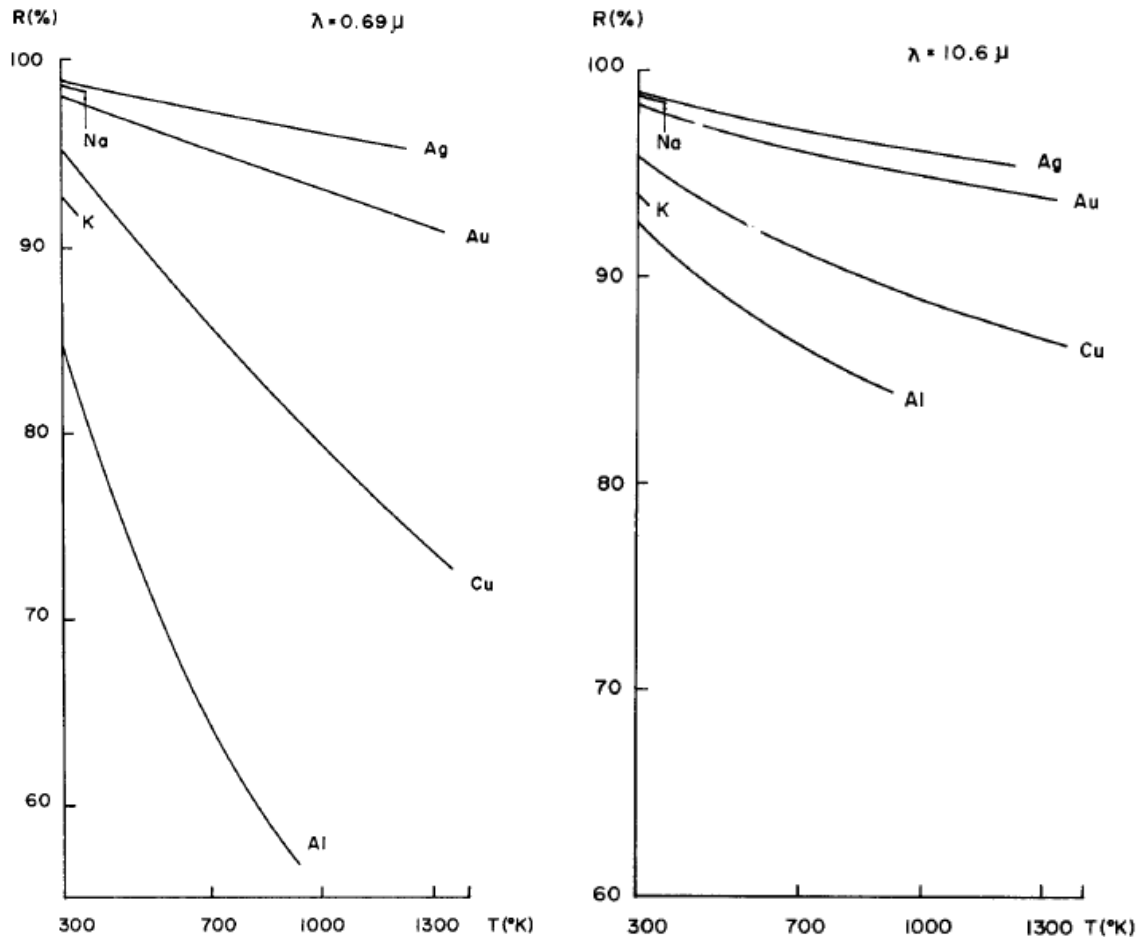


Figure 7. Reduction in reflectivity with rising temperature at 0.69 (left) and 10.6 μm (right) for silver (Ag), gold (Au), sodium (Na), copper (Cu), potassium (K), and aluminum (Al). From [56].

For metals like gold and silver, reduction in reflectivity with temperature rise is almost negligible, especially over the longer IR wavelengths. This makes silver an ideal choice as a reflective boundary in high-temperature environments. Representative values of thermal expansion, melting point, electrical conductivity, and thermal conductivity of bulk Ag are given in Table 2.

Table 2. Electrical and Thermal Properties of Bulk Silver (Ag).

	Bulk Silver (Ag)
Thermal Expansion Coefficient (per K) [52]	19.2×10^{-6}
Melting Point (K)	1230
Electrical Conductivity (S/m) [34]	6.12×10^7
Thermal conductivity (Watts/m K) [52]	427

A model was used to approximate the optical constants of silver at high temperatures. This was accomplished by using a dielectric function given by the free-electron/Drude model

$$\varepsilon(\omega) = 1 - \left(\frac{\omega_p^2}{\omega(\omega - i\omega_c)} \right), \quad (13)$$

where ω is frequency, ω_p is plasma frequency, and ω_c is electron collision frequency [56, 57]. As temperature increases, so does the electron collision frequency ω_c [56]. This results in increased absorption of the metal at high temperatures which directly affects cavity losses. The temperature dependence of the plasma frequency ω_p is very small due to volume expansion, consequently ω_p can be approximated as a constant [56]. Thus, the silver dielectric function can be approximately modeled using the $\omega_p = 8.28$ eV and $\omega_c = (0.048/300^{1.3}) T^{1.3}$, where T is temperature [30]. Figure 8 shows the real and imaginary parts of the complex dielectric function of silver at 294 K (room temperature) and 1000 K as calculated from the free-electron/Drude model from 1-10 μm .

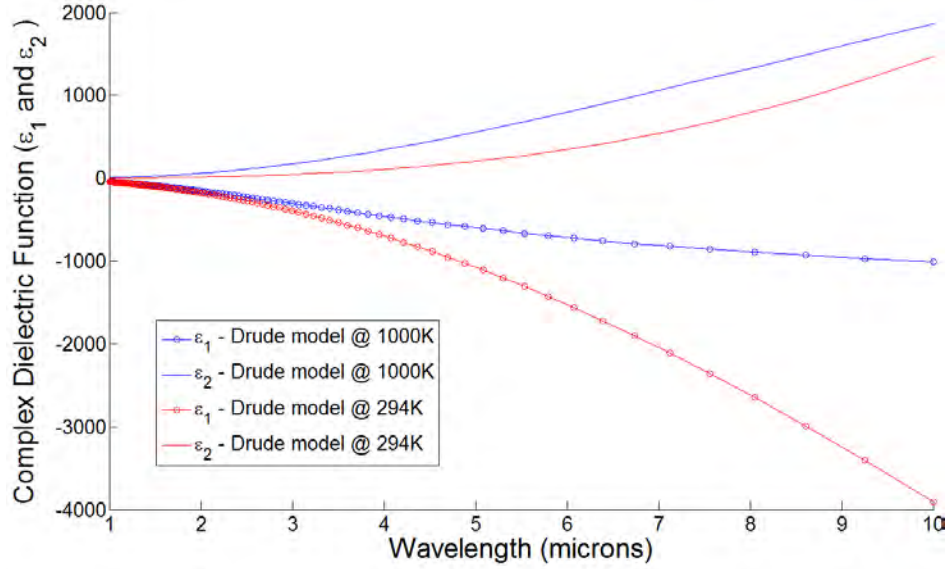


Figure 8. Real and imaginary parts of the complex dielectric function of silver at room 294 K (room temperature) and 1000 K as calculated from the free-electron/Drude.

The complex dielectric constant ε of a material is equal to the square of the complex index of refraction, determining the optical constants of the material. The choice of using $n - ik$ or $n + ik$, where k is the imaginary part of the refractive index (extinction coefficient), depends on the sign of the assumed plane-wave solution in Maxwell's equations. For this effort, a forward propagating wave is chosen to have the form $e^{-j\vec{k}\cdot\vec{r}}$, where \vec{k} is the direction of propagation and \vec{r} is the position vector. Thus, the $n - ik$ convention will be chosen here. The relationship between the real (ε_1) and imaginary (ε_2) parts of the complex dielectric constant and the complex refractive index is

$$\varepsilon = \varepsilon_1 - i\varepsilon_2 = (n - ik)^2. \quad (14)$$

From the free-electron/Drude model above, the real and imaginary parts of the dielectric constant were solved for over a range of IR frequencies at a given temperature T .

Accounting for the frequency-dependence of the complex dielectric constant yields the following expressions for the real and imaginary parts of the complex index of refraction as a function of frequency ω ,

$$n(\omega) = \sqrt{\frac{1}{2} \{ \epsilon_1(\omega) + [\epsilon_1^2(\omega) + \epsilon_2^2(\omega)]^{\frac{1}{2}} \}} \quad (15)$$

and

$$k(\omega) = \sqrt{\frac{1}{2} \{ [\epsilon_1^2(\omega) + \epsilon_2^2(\omega)]^{\frac{1}{2}} - \epsilon_1 \}}. \quad (16)$$

Finally, temperature-dependent optical constants for silver were calculated at various high temperatures. Figure 9 compares the complex refractive index of bulk Ag at room temperature to several high temperatures over a range of IR wavelengths.

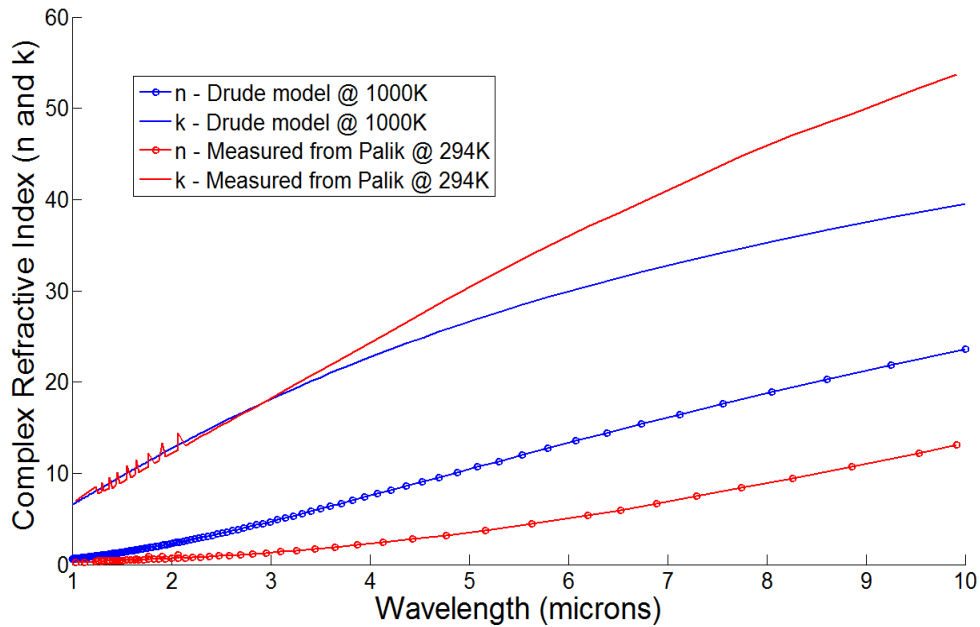


Figure 9. Complex refractive index for Silver (Ag) using a free-electron/Drude model at 1000 K plotted with measured bulk values reported in Palik [44].

Angular Reflectance and Emittance of Ag

The calculated high-temperature optical constants for germanium and silver were then compiled into MATLAB® where RCWA formulations were used to solve for the electromagnetic fields of the truncated resonator problem. The bottom silver layer must be opaque allowing negligible transmission of incident radiation through the cavity. The typical skin depth of silver at optical frequencies is approximately 22-30 nm at room temperature. In general, the skin depth of a metal increases as temperature increases and this is numerically observed to be most prevalent at longer wavelengths [56]. For example at 10.6 μm , the skin depth of Ag monotonically rises from 26 nm near room temperature (300 K) to 55 nm near its melting point (1230 K) [56]. When metal is deposited, the atomic structure of the material is amorphous allowing electromagnetic energy to penetrate deeper into the metal than would be expected for a bulk metal. A thickness between 200-300 nm of silver was targeted to ensure that the bottom reflective layer was predominantly opaque with respect to IR wavelengths.

The resonator is a planar structure made up of three uniform homogeneous layers, silver-germanium-silver (Ag-Ge-Ag). Assuming the top silver layer is optically smooth, only the dominant specular reflection is considered and expected to dominant the scattering response of the structure. The RCWA, implemented in MATLAB®, is set up to calculate bi-static specular reflectance (0th diffraction order) over a wide range of wavelengths and angles of incidence. The top, optically thin Ag layer will have a TM polarized (p-pol) plane wave incident upon it from free space at an angle θ measured from surface normal. The RCWA method makes no approximation to the material properties of a given structure. This allows the user to input modeled or empirical

complex refractive index values for all constituent materials, such as those calculated for high-temperature applications.

After calculating the reflected and transmitted fields, a dispersion relationship can be generated showing the specular reflectance over a range of incident angles. The p-pol specular reflectance for Ag at room temperature (294 K) between 0.1-10 μm is shown in Figure 10. The plasma frequency of Ag, calculated by RCWA, is observed at about 350 nm, which is in agreement with literature. At longer wavelengths, high reflectance is observed to be ubiquitous as expected for a metal above its plasma frequency. This is more easily visible in Figure 11 where a close-up of the spectral reflectance is shown between 0.1-0.5 μm .

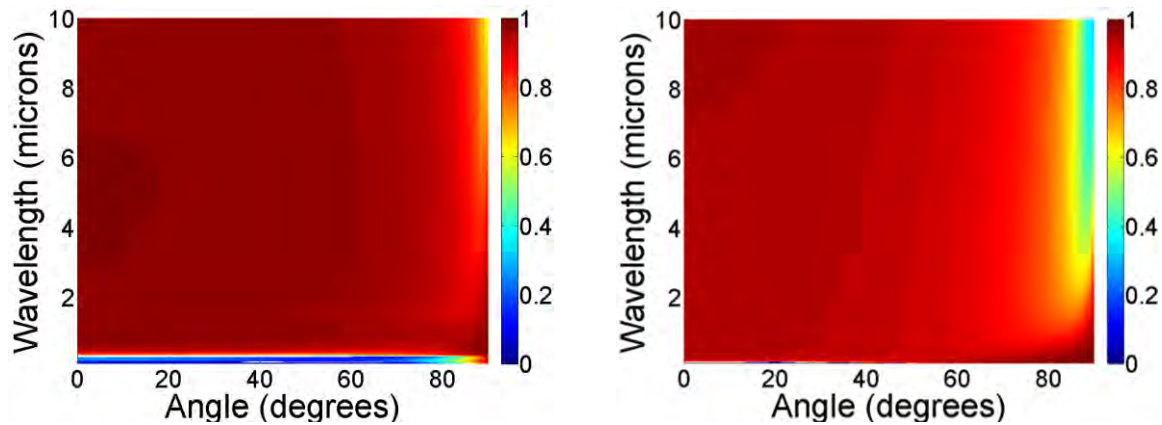


Figure 10. Calculated specular reflectance (p-pol) for Ag at 294 K (left) and 1000 K (right) from 0.1-10 μm . Specular reflectance at 294 K was calculated using complex refractive index from Palik [44]. Specular reflectance at 1000 K was calculated using complex refractive index values using a Drude model.

At finite temperatures above 0 K, the material properties of metals are known to not only vary spectrally, but also with increasing temperature. The difference between the dispersions of Ag at 294 K and 1000 K is compared in Figure 10 where the optical constants for each temperature were acquired from Palik's Handbook [44] and the Drude

model, respectively. Note the decrease in reflectance at grazing incident angles as longer IR wavelengths are approached. The plasma frequency of Ag is observed to shift towards shorter wavelengths, commonly referred to as “blue-shifted”, with the increase in temperature. This is shown in Figure 11.

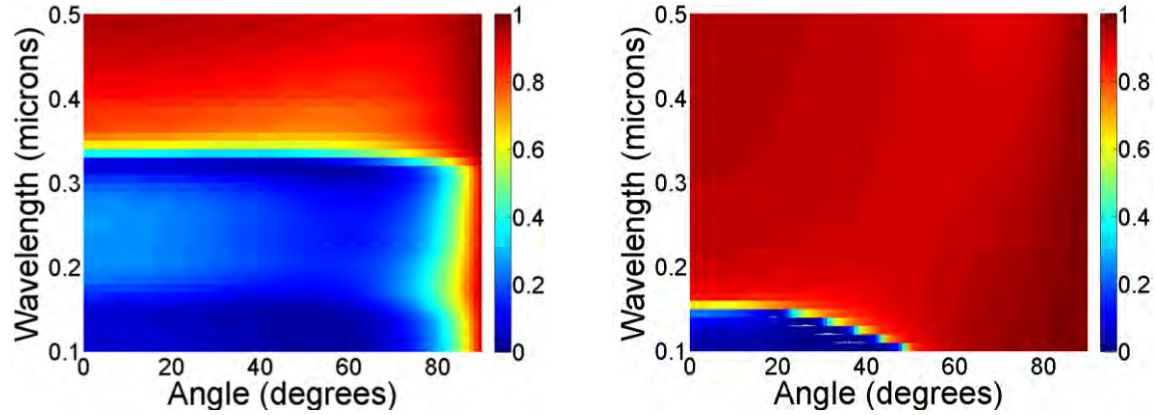


Figure 11. Calculated specular reflectance (p-pol) for Ag at 294 K (left) and 1000 K (right) from 0.1-0.5 μm . Specular reflectance at 294 K was calculated using complex refractive index from Palik [44]. Specular reflectance at 1000 K was calculated using complex refractive index values using a Drude model.

From conservation of energy, assuming an opaque structure with zero transmission allows absorption to be found using Equation (3), $\alpha = 1 - \rho$. Invoking Kirchhoff’s Law, emittance is assumed to equal absorptance $\alpha = \varepsilon$ and subsequently the spectral angular emittance of the structure can be derived. An example of the angular emittance of Ag at 1000 K over a range of IR wavelengths is shown in Figure 12.

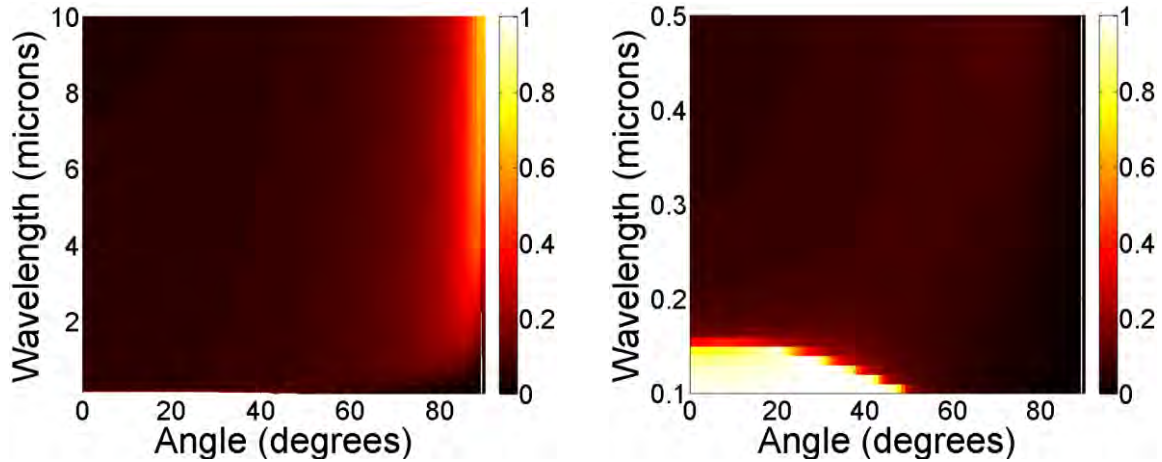


Figure 12. Calculated specular emittance (p-pol) for Ag at 1000 K over two wavelength bands, 0.1-10 μm (left) and 0.1-0.5 μm (right). Specular emittance was calculated using complex refractive index values using a Drude model.

This representation of the calculated spectral emittance expected from a structure over a wide range of incident angles will be used from here on out. The original intent of this RCWA approach from [42] was to calculate the diffraction efficiencies for metallic surface-relief gratings made up of one material. For this effort, multiple materials would be incorporated into a single design so the original code was modified to handle multiple materials, each with its own complex permittivity. The RCWA code was validated by comparing its results to published analytical results and to those calculated using commercial software (*e.g.* CST and Essential Macleod). Using this design tool, two multilayer resonator samples with differing Ge thicknesses will be proposed and analyzed in the next chapter.

Fabrication

There are a plethora of nano-fabrication techniques used to create micro- and nano-scaled optical structures, to include electron-beam lithography, direct laser writing, and other templating approaches [26]. Fabrication efforts from this work will be conducted using

both the AFIT Class 1000 Clean Room and AFRL facilities. Known fabrication tools owned by AFRL at Wright-Patterson AFB include a Nanoscribe 3D laser lithography system, FEI Quanta dual-beam focused ion milling system, and Nanonex nano-imprint lithography (NIL) system.

Material deposition will be accomplished in collaboration with the AFRL, Materials and Manufacturing Directorate. Substrates consisted of p-type (boron doped) silicon (Si) wafers having Prime grade, 1-10 Ω resistivity, and (100) orientation. These Si wafers were acquired by AFRL from *University Wafer*. For both thermal emitters, a HIPIMS deposition technique will be utilized for layering the Ag and Ge. HIPIMS is an ionized plasma vapor deposition technique, capable of depositing dense, uniform films at room temperature [58, 59]. Material deposition was within a high-vacuum chamber, evacuated to a pressure below 1.0×10^{-6} Torr. Figure 13 shows an SEM micrograph of the cross-section of a Ge sample deposited using the same conditions and equipment mentioned above. A dense, columnar microstructure can be observed for HIPIMS-deposited Ge [60].

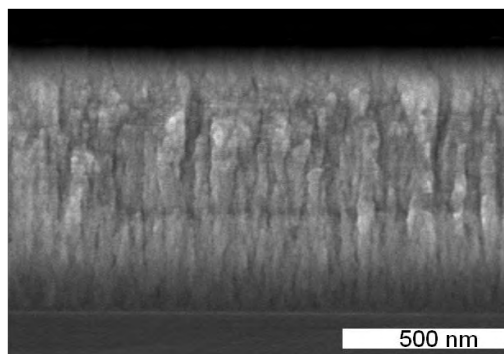


Figure 13. Scanning Electron Microscope (SEM) micrograph of the cross-section of a Ge sample deposited on a Si wafer and prepared by the Air Force Research Laboratory (AFRL) using a High Power Impulse Magnetron Sputtering (HIPIMS) technique. From [60].

Hybrid PC–Multilayer

A PC is a class of complex media in which the electromagnetic properties of the material are tunable over various frequencies and length scales. Thirty years previous, Yablonovitch [61] and John [62] were credited with the novelty and experimental realization of PCs. While some traditional views would only consider dielectric systems as PCs, this thesis includes metal-dielectric systems in the PC class of structures. The optical structures discussed here have scales of periodicity that are on the order of the design wavelength in the IR regime so the term, PC, is chosen. This section details the design and fabrication of a hybrid structure constructed of a hole array embedded inside of a truncated multilayer resonator. Hence, for the remaining portion of this document, this structure will be referred to as a PC-multilayer. An illustration of the PC-multilayer is shown in Figure 14.

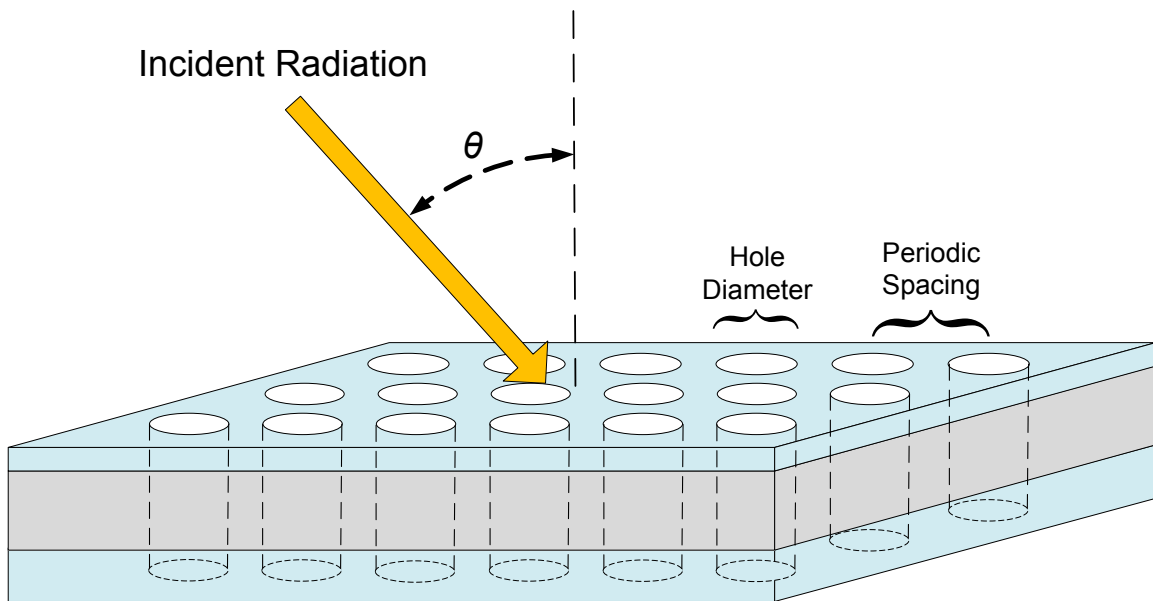


Figure 14. Illustration of a photonic crystal-multilayer hybrid structure constructed of a circular hole array embedded inside of a truncated multilayer resonator.

Design

The RCWA approach used in designing the multilayer resonator is capable of handling periodic geometries only along one dimension. The PC-multilayer has a periodic geometry (circular holes) in two dimensions. Therefore, computer simulations through CST will be utilized for this more complex geometrical problem. An illustration showing a finite portion of the PC-multilayer, as viewed from surface normal, is shown in Figure 15, where a is the period between each hole and d is the diameter of each hole.

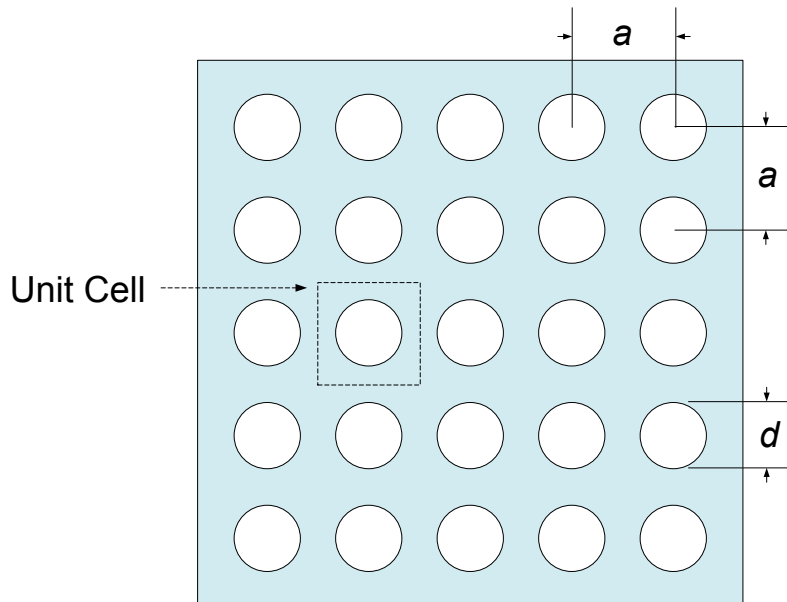


Figure 15. Illustration of a photonic crystal-multilayer hybrid structure constructed of a square array of circular holes embedded inside of a multilayer, where a is the period between each hole and d is the diameter of each hole. View is from surface normal of the structure.

Fabrication

Fabrication of the hybrid PC-multilayer structure will involve both HIPIMS deposition and a FIB milling system. After HIPIMS material deposition, milling will occur using a FEI Quanta Dual Beam FIB system located in the AFRL Material Characterization

Facility (MCF). This tool uses focused ions to ablate material away with high precision. Grayscale milling is possible, where a bitmap image can be loaded into the system to mill a predetermined pattern. Depending on the scale of gray in the bitmap image, the FIB system will adjust its power accordingly. Newer FIB systems are capable of generating patterns automatically through pattern generator tools. Currently, the AFRL MCF does not have a FIB system equipped with a pattern generator, so the patterns to be milled for this effort will be generated manually.

Reflectance/Ellipsometric Measurements

The J. A. Woollam IR-VASE is capable of measuring reflection and transmission characteristics from a surface. Transmittance measurements are limited to surface normal on this instrument. Reflectance measurements can be taken from angles of incidence between 25-90° from wavelengths 1-40 μm . Due to inherent noise of the system, the optimum wavelength range for analyzing reflection data will be from wavelengths 1.7-20 μm . Due to the finite width of the samples, incident angles between 25-80° will be measured in 1° increments.

The purpose of taking ellipsometric measurements is two-fold. First, using J. A. Woollam modeling tools, the actual thicknesses resulting from the HIPIMS deposition process can be verified. Second, using these same modeling tools, the material properties can be extracted from the ellipsometric measurements and provide a basis of comparison to bulk values published in Palik's *Handbook of Optical Constants of Solids* (1985) [44] and other reported optical constants. The models will be fit using preloaded materials from J. A. Woollam's IR library. The optical constants found in Palik's extensive

inventory of materials are observed to be the most prevalent in literature. Palik does quote some temperature-dependent optical constants, but these are sparse in comparison to room-temperature values due to the rarity of high-temperature investigations into such areas.

Spectroscopic ellipsometric measurements will be made over a range of IR wavelengths using the IR-VASE on the sample substrate and constituent materials making up the multilayer resonator. The advantages of IR-VASE include its wide spectral range from wavelengths 1.7-20 μm and the capability to acquire full ellipsometric measurements at multiple angles. This enables the IR-VASE to determine both complex refractive index and complex permittivity for materials over its entire spectral range with high accuracy. The thicknesses and effects of native oxides observed on each of the layers will also be investigated.

Calculating Emittance

Emittance associated with thermally heated structures will be derived from radiance measurements taken using an in-house AFIT emissometer. This assembly consists of a rotation-controlled thermoelectric heating stage, MR-154 Bomem FTIR, and off-axis parabolic mirror. Using this experimental setup, observations of the spectral and angular characteristics of a surface's emittance will be made while a sample is thermally excited to varying degrees of high temperature.

First, two calibration points for the MR-154 will be made using a calibrated blackbody. This calibration set provides hot and cold temperature references that bound the expected brightness temperature for a given scene. During calibration, the blackbody

will be positioned so that it fills the field of view (FOV) of the instrument. This calibration technique is recommended by the Bomem user's guide when the samples are expected to also fill the FOV [63]. This calibration method will be used for all measurements made during this experiment. After calibration, each sample will be elevated in temperature to various high temperatures using a hot plate. Using a thermocouple, the temperature of the sample's surface will be verified before each radiance measurement.

If the source, or sample, being measured fills the entire FOV, the expected radiance contributions seen by the instrument will come from sample self-emissions and background reflections. Assuming ϕ variations (see Chapter II, Figure 1) and radiance of the path are negligible for this analysis, the measured radiance can be expressed as

$$L_{meas}(\lambda, \theta, T_{samp}) = L_{back}(\lambda, \theta, T_{back}) + L_{samp}(\lambda, \theta, T_{samp}) \quad (17)$$

where L_{meas} is the measured radiance, L_{back} is the radiance of the background, L_{samp} is the radiance of the sample, T_{back} is the temperature of the background, T_{samp} is the temperature of the sample and θ is the zenith angle as described in Chapter II, Figure 1. The background is assumed to be uniform in this calculation. Utilizing Equation (4) for the sample reflectance and substituting Equation (6) in for the sample radiance, the equation for measured radiance now becomes

$$L_{meas}(\lambda, \theta, T_{samp}) = [1 - \varepsilon_{samp}(\lambda, \theta, T_{samp})]L_{bb}(\lambda, T_{back}) + \varepsilon_{samp}(\lambda, \theta, T_{samp})L_{bb}(\lambda, T_{samp}). \quad (18)$$

Solving for $\varepsilon_{samp}(\lambda, \theta, T_{samp})$ yields the following expression for emittance of the sample

$$\varepsilon_{\text{samp}}(\lambda, \theta, T_{\text{samp}}) = \frac{L_{\text{meas}}(\lambda, \theta, T_{\text{samp}}) - L_{\text{bb}}(\lambda, T_{\text{back}})}{L_{\text{bb}}(\lambda, T_{\text{samp}}) - L_{\text{bb}}(\lambda, T_{\text{back}})}. \quad (19)$$

As a result, emittance as a function of wavelength and angle can be calculated from the radiance measurements obtained from AFIT's emissometer for a sample above the background temperature. This operation will be carried out for each sample at several high temperatures above ambient.

Summary

The purpose of this chapter was to define the approach selected for the design, fabrication, and characterization of two thermal selective emitters. The associated processes were briefly described for each of these phases. With this in mind, the next chapter will follow-up with the resulting analytical designs for each thermal emitter. Fabrication results will be presented. Finally, measurements for each sample will be analyzed and compared to those expected from theory.

V. Analysis and Results – Truncated Resonator

Chapter Overview

This chapter is split into three main sections. The reflectance and emittance findings for the truncated resonator are discussed first, beginning with the final designs that would be carried forward to fabrication and measurement. The second section reports the ellipsometric measurements taken for the constituent materials used in each design. A comparison between derived optical constants and those acquired from published sources is made. The third section highlights the design and initial fabrication results associated with the PC-multilayer.

Truncated Multilayer Resonator Design

Spectrally selective absorption centered at $6\ \mu\text{m}$ was desired for this structure. This mid-IR wavelength was chosen since the temperature associated with a peak Planckian distribution at $6\ \mu\text{m}$ is 483 K. This temperature is practically realizable in a laboratory experiment and is still relevant with respect to those wavelengths (2-20 μm) where all finite temperature biological materials and mechanical objects emit thermal radiation [3]. Thus, the original design called for a thick Ge layer for the middle transparent medium of the resonator around 740 nm. However, due to the dynamic environment of the deposition process, the first sample came out with a Ge thickness closer to 240 nm. The second sample had a 600 nm Ge layer. Therefore, this section describes the design, fabrication, and characterization of two Ag-Ge-Ag resonating structures with layer thicknesses of 6-240-160 nm for one sample and 6-700-200 nm for the other.

Sample 1: 6-240-160 nm (Ag-Ge-Ag)

A thickness between 150-200 nm of Ag was targeted to ensure that the bottom reflective layer was predominantly opaque with respect to IR wavelengths. The thickness of the transparent medium made up of Ge was examined at 240 nm. Several thicknesses were considered for the top, optically thin Ag layer. Lee and Zhang's (2006) [9] Ag-SiO₂-Ag resonant cavity used a thickness of 22 nm for their top Ag layer but they wanted 15 nm. Wang *et al.*'s (2009) [11] cavities, constructed of Au-SiO₂-Au, had thicknesses between 21 and 30 nm. Chang *et al.* (2009) used 11- and 15-nm thick Ag layer thicknesses on their Ag-SiO₂-Ag thermal emitter. To the best of the author's knowledge, this is the only published work to utilize a top reflective layer that was below the penetration depth of the associated metal.

A comparison of calculated angular emittance spectra of this truncated resonator with several different thicknesses from 6-50 μm for the top Ag layer is shown in Figure 16. In general, an increase in calculated angular emittance was observed as the thickness of the top Ag layer decreased, especially near normal at longer IR wavelengths. For this effort, a thickness of 6 nm was chosen to analyze the effects of using an ultra thin layer of metal for the top reflective layer of the resonator. This was also the thinnest Ag thickness achievable using the HIPIMS deposition technique. Based on empirical results from this same equipment and deposition technique, thin layers of Ag below 6 nm tended to form "islands" of Ag particles causing a non-uniform film to develop [60].

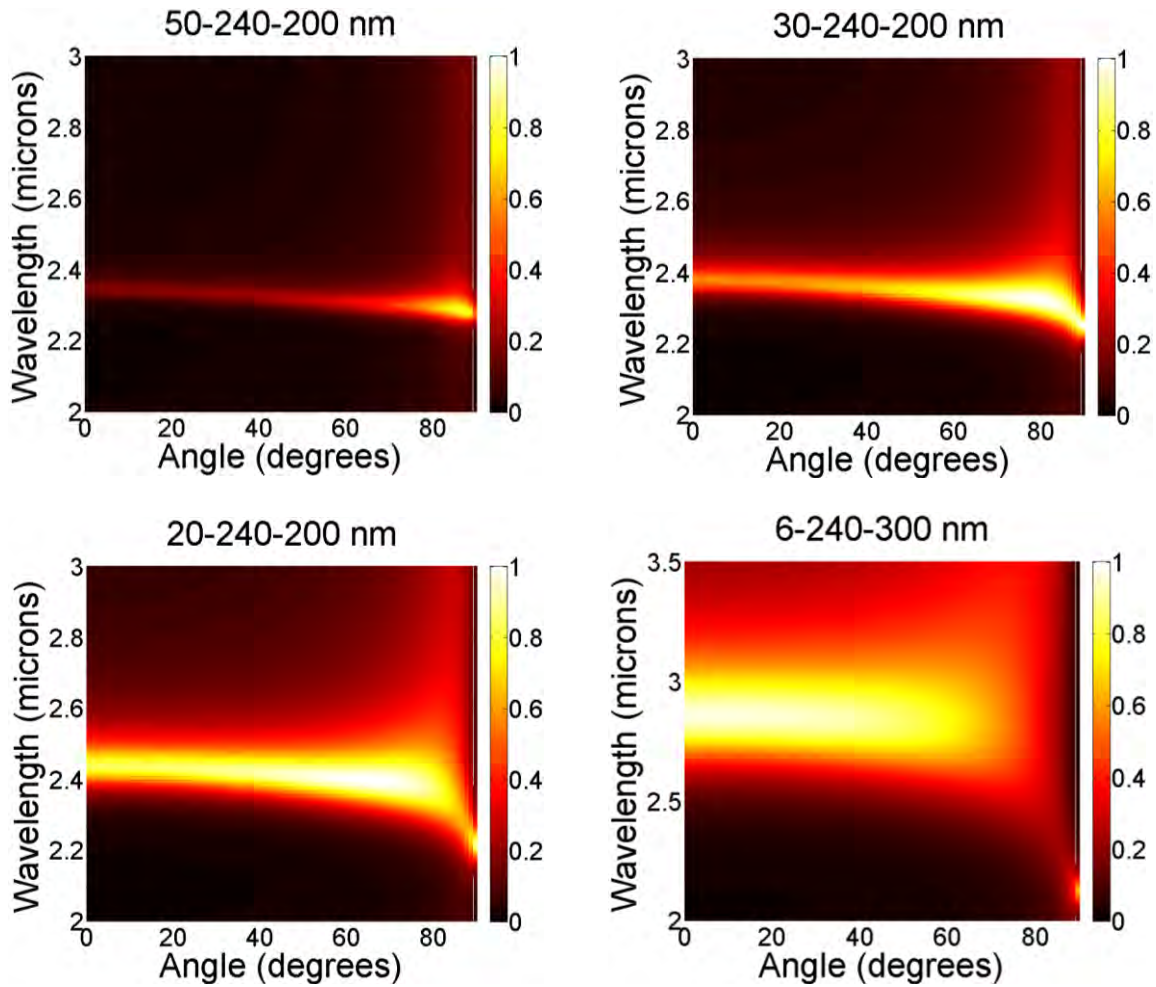


Figure 16. Comparison of the calculated angular emittance (p-pol) spectra of a Ag-Ge-Ag truncated multilayer resonator with varying thicknesses for the top, optically thin Ag layer.

The resulting dispersions in the 2-10- μm wavelength band of interest expected for a 6-240-160-nm (Ag-Ge-Ag) resonating structure at 294 K (room temperature) and 500 K are shown in Figure 17 and Figure 18, respectively. Increased emittance, centered at 2.75 μm , was observed over a wider range of incident angles for Sample 1 when the temperature increased from room temperature to 500 K.

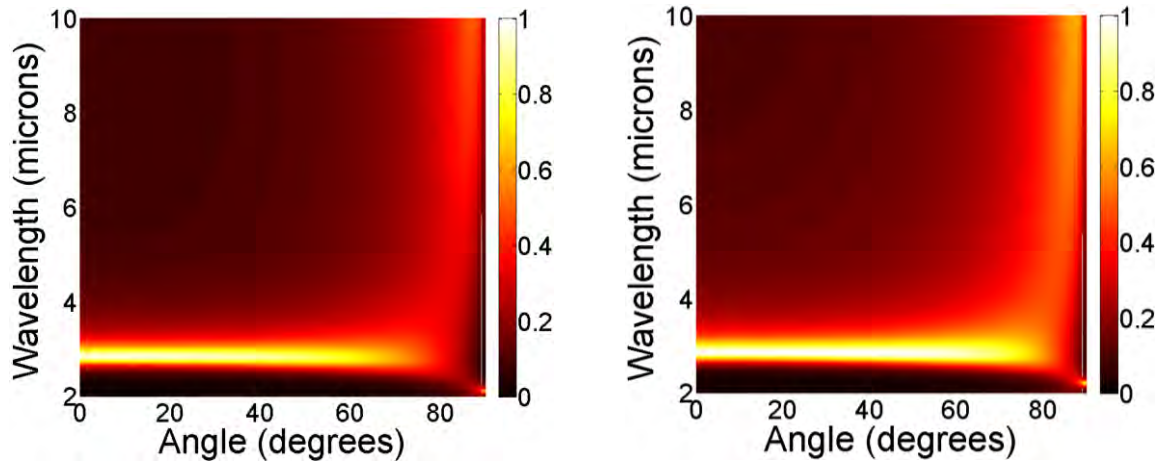


Figure 17. Calculated angular emittance (p-pol) for a Ag-Ge-Ag resonating structure at 294 K (left) and 500 K (right) from 2-10 μm . Thicknesses of constituent materials are 6-240-160 nm, respectively.

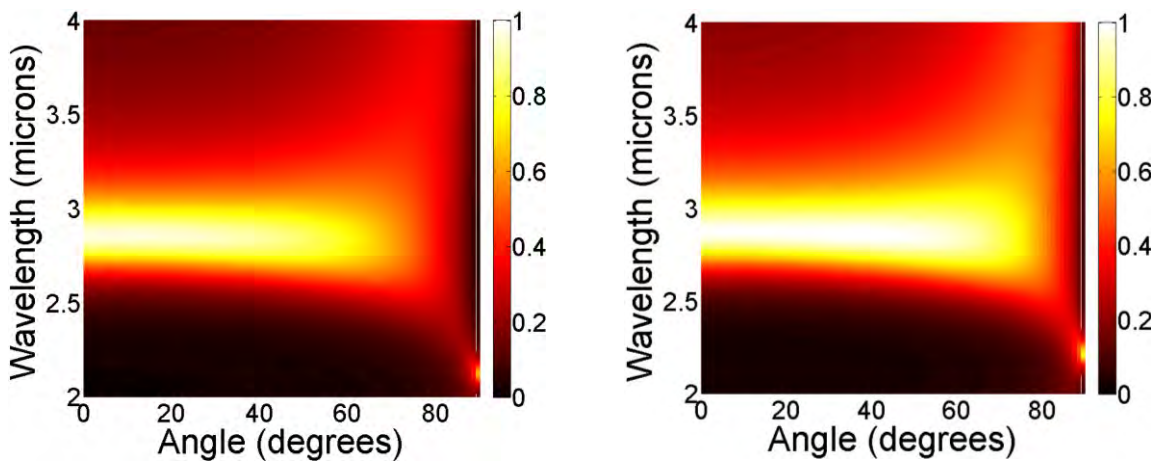


Figure 18. Calculated specular emittance (p-pol) for a Ag-Ge-Ag resonating structure at 294 K (left) and 500 K (right) from 2-4 μm . Thicknesses of constituent materials are 6-240-160 nm, respectively.

Sample 1: Fabrication Results

The truncated resonator design called for an opaque layer of Ag to be deposited first on the Si substrate. This would ensure that negligible transmission would be expected through the multilayer. Next, an IR transparent medium would be deposited made up of Ge. This layer was designed for a thickness of 240 nm in the previous section. Last, a 6-

nm optically thin layer of Ag would be deposited to complete the cavity. All three layers were deposited using a HIPIMS deposition technique. An SEM micrograph of Sample 1 at 100,000× magnification is shown in Figure 19.

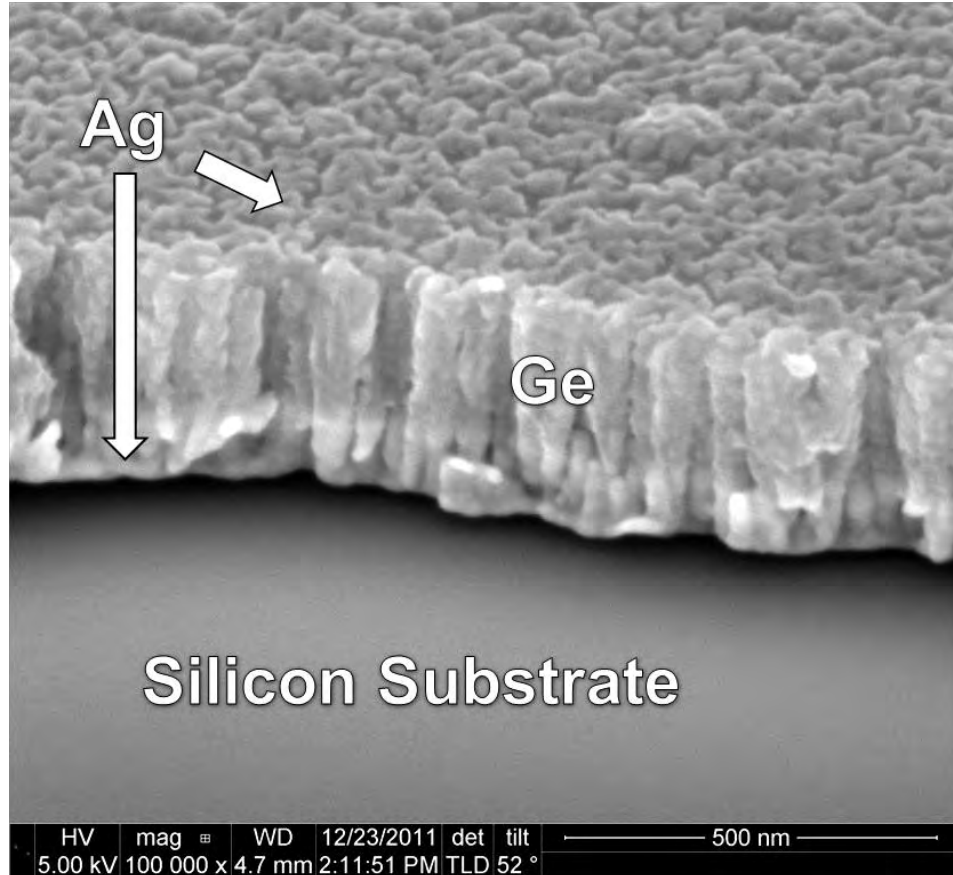


Figure 19. SEM micrograph of a Ag-Ge-Ag truncated resonator (6-240-160 nm) on a silicon substrate. Ag and Ge layers were deposited via a High Power Impulse Magnetron Sputtering (HIPIMS) technique. Micrograph was taken at 100,000× magnification and at an angle of 52° from surface normal.

Since the micrograph was taken at an elevated angle (52° tilt), the absolute top and bottom of the structure could not be ascertained. Thus, the exact dimensions could not be determined from the SEM alone for Sample 1. Figure 20 shows a micrograph of Sample 1 at 75,000× magnification using a different SEM and at a different location on

the sample. The yellow marked scales shown on the micrograph were made with the SEM dimensioning software and show measurement estimates for the total height of the structure.

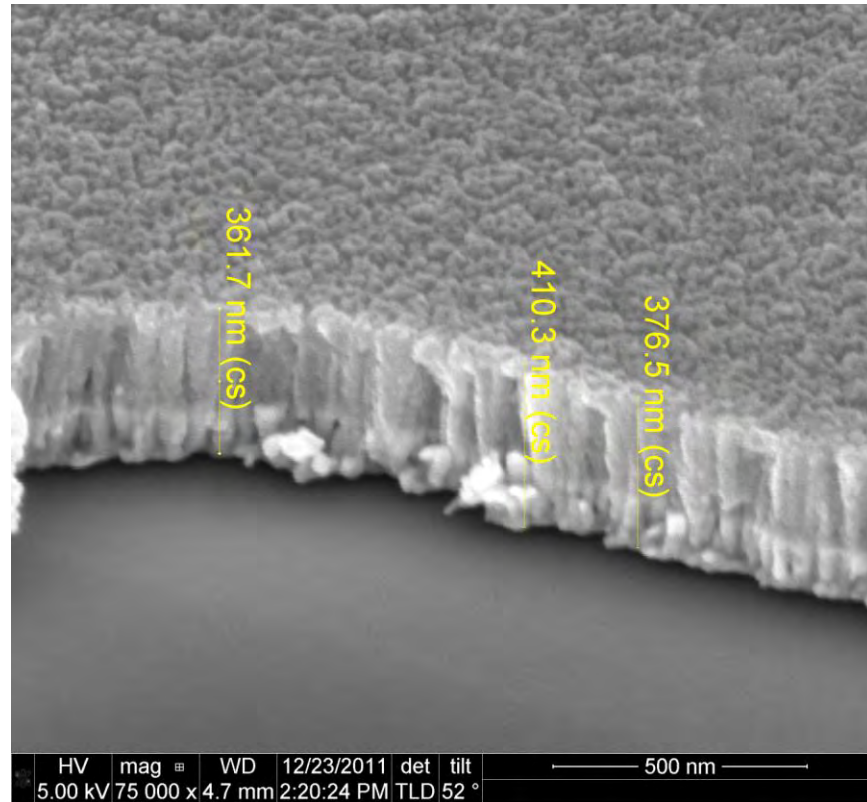


Figure 20. SEM micrograph of a Ag-Ge-Ag truncated resonator (6-240-160 nm) on a silicon substrate. Measurements shown on the micrograph were made with the SEM showing several different estimates of the total height of the structure. Ag and Ge layers were deposited via a High Power Impulse Magnetron Sputtering (HIPIMS) technique. Micrograph was taken at 75,000 \times magnification and at an angle of 52 $^\circ$ from surface normal.

Based on the yellow scale bars, the bottom layer of Ag was estimated at 160 nm and the Ge layer was estimated at 240 nm. Both the opaque Ag and transparent Ge layers were amorphous and exhibited a dense columnar microstructure. The thickness of the optically thin layer of Ag on top of the Ge was not discernible. However, the uniformity

of the top Ag layer appeared perturbed. This was speculated to be a side-effect of the uneven geometry of the underlying columnar Ge layer on which it was deposited on.

Sample 1: Reflectance Measurements

Reflectance measurements were taken using a IR-VASE owned by AFRL. These reflectance measurements were made in 1° increments starting at a 25° incident angle and ending at 80°. Spectral reflectance from wavelengths 1.4-20 μm for Sample 1 from 25-80° in 1° increments is shown in Figure 21.

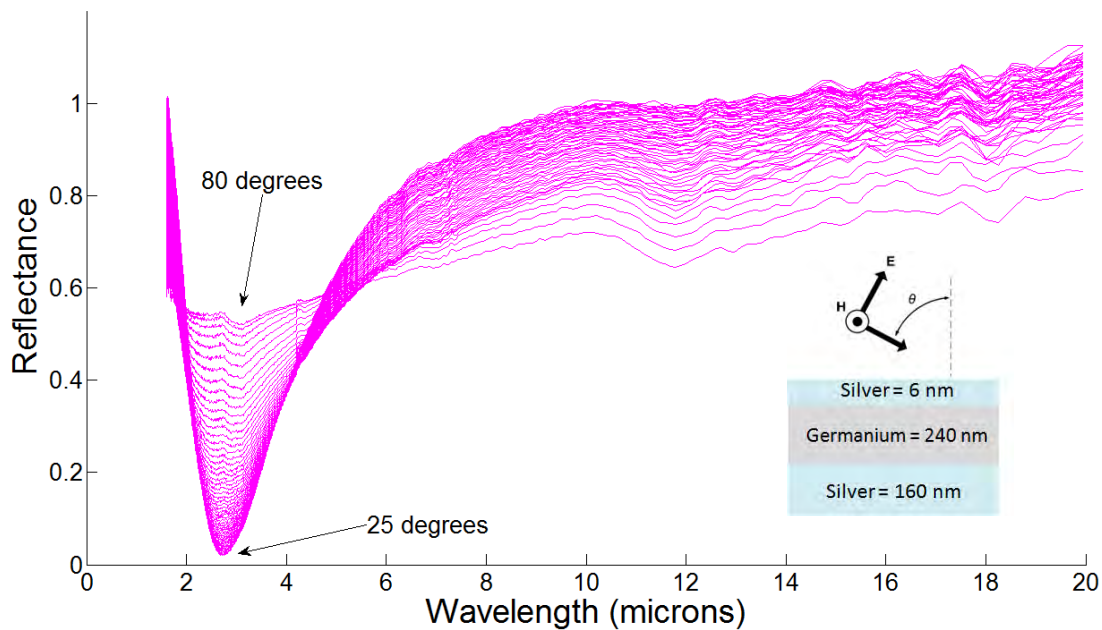


Figure 21. Spectral reflectance (p-pol) of a Ag-Ge-Ag truncated resonator (6-240-160 nm) between 1.4 and 20 μm. Reflectance measurements were taken using a J. A. Woollam Infrared – Variable Angle Spectroscopic Ellipsometer (IR-VASE).

An absorption band is clearly visible and centered at approximately 2.75 μm. The reflectance dip is deepest near normal at 25° and decreases as a function of increasing incident angle as it approaches 80°. Figure 22 shows a close-up of the reflectance dip due

to selective absorption from the resonating structure. Ten-degree increments are shown here from 25-75°.

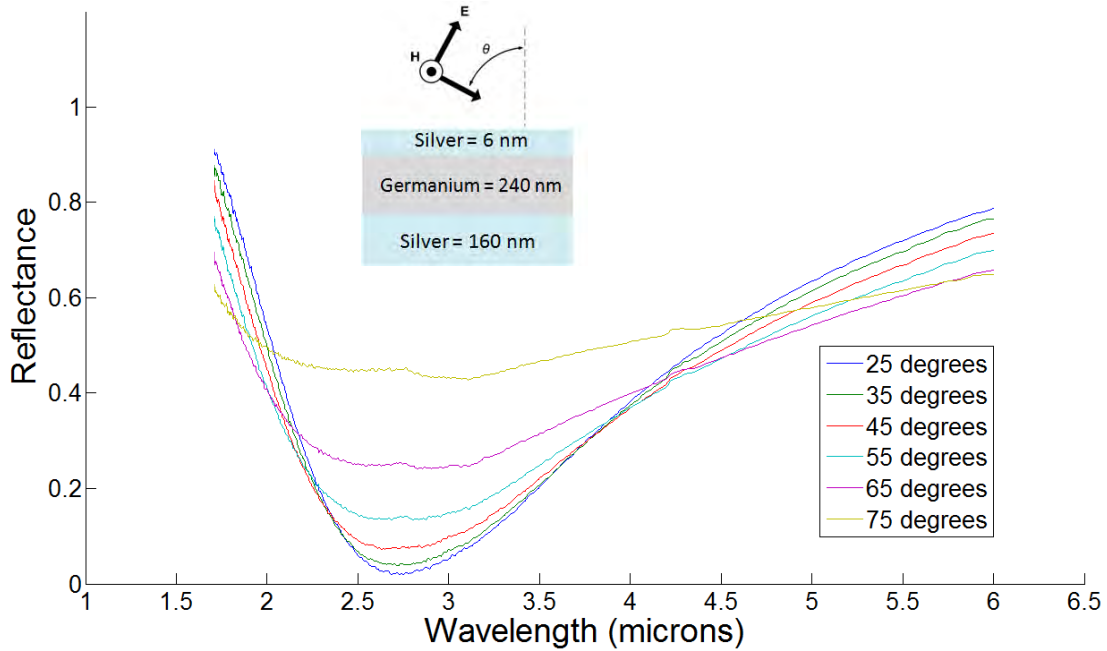


Figure 22. Spectral reflectance (p-pol) of a Ag-Ge-Ag truncated resonator (6-240-160 nm) on silicon between 1.7 and 6 μm. Reflectance measurements were taken using a J. A. Woollam Infrared – Variable Angle Spectroscopic Ellipsometer (IR-VASE).

Assuming an opaque structure with zero transmission allows absorptance to be found using Equation (3), $\alpha = 1 - \rho$, from conservation of energy. Thus, the absorptance can be calculated from the measured reflectance values from the IR-VASE. From Kirchhoff's Law, emittance can be equated to absorptance $\varepsilon = \alpha$ for a structure in thermal equilibrium. Hence, the spectral angular emittance of the multilayer resonator can be described using the IR-VASE reflectance data. A comparison between theoretical emittance results calculated through RCWA and experimental emittance results calculated from IR-VASE reflectance measurements is shown in Figure 23 for Sample 1.

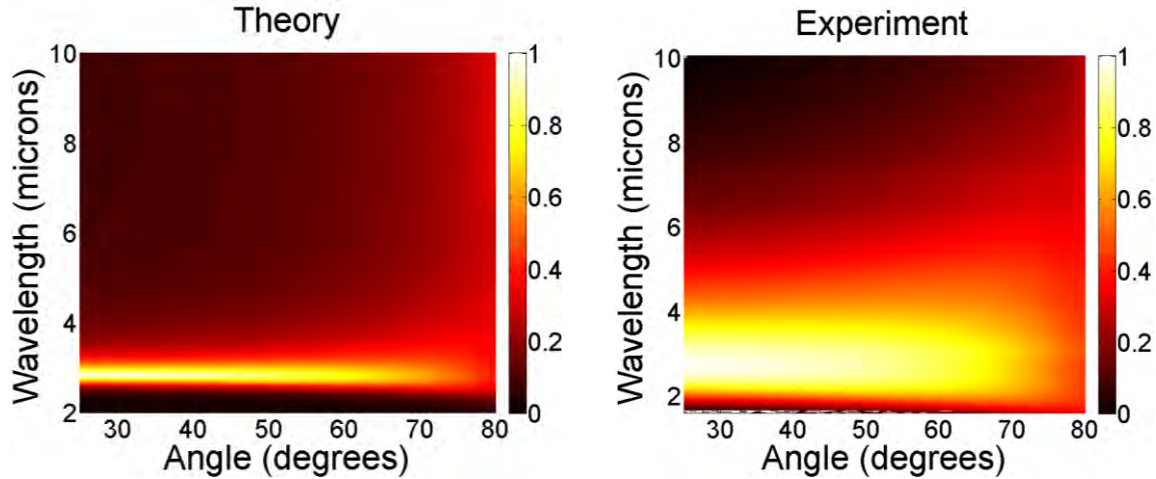


Figure 23. Comparison (p-pol) between theoretical emittance results (left) and experimental emittance results (right) found through measurements taken using a J. A. Woollam Infrared Variable Angle Spectroscopic Ellipsometer (IR-VASE) for a Ag-Ge-Ag resonating structure with thicknesses 6-240-160 nm, respectively.

The emittance peak was centered at 2.75 μm as expected but a broadening of the emittance band was observed. Lower experimental emittance near normal at longer wavelengths from 8-10 μm was also observed when compared to theory. Since bulk optical constants from Palik [44] were used to calculate the analytical results at room temperature for this comparison, it is possible that the deposited Ag and Ge may exhibit different material properties to some degree. This will be explored later in this chapter when analyzing the spectroscopic ellipsometry measurements to derive the actual optical constants of the constituent materials. Fabrication error may also be a culprit in the disparate results. As an example, Figure 16 indicates a thinner top Ag layer leads to broader emittance bands. It is possible the top Ag layer is even thinner than 6 nm. Another explanation for the broadened emittance band is the lack of a continuous top Ag layer.

Sample 2: 6-700-200 nm (Ag-Ge-Ag)

The second Ag-Ge-Ag multilayer resonator, Sample 2, had thicknesses of 6, 700, and 200 nm for the constituent materials, respectively. The dispersions in the 2-20- μm wavelength band expected for Sample 2 at 294 K (room temperature) and 500 K are shown in Figure 24. Decreased calculated emittance was observed near normal at the 7- μm absorption band for this structure when the temperature increased from room temperature to 500 K. At longer wavelengths above 15 μm , calculated emittance was significantly higher, especially towards grazing angles of incidence.

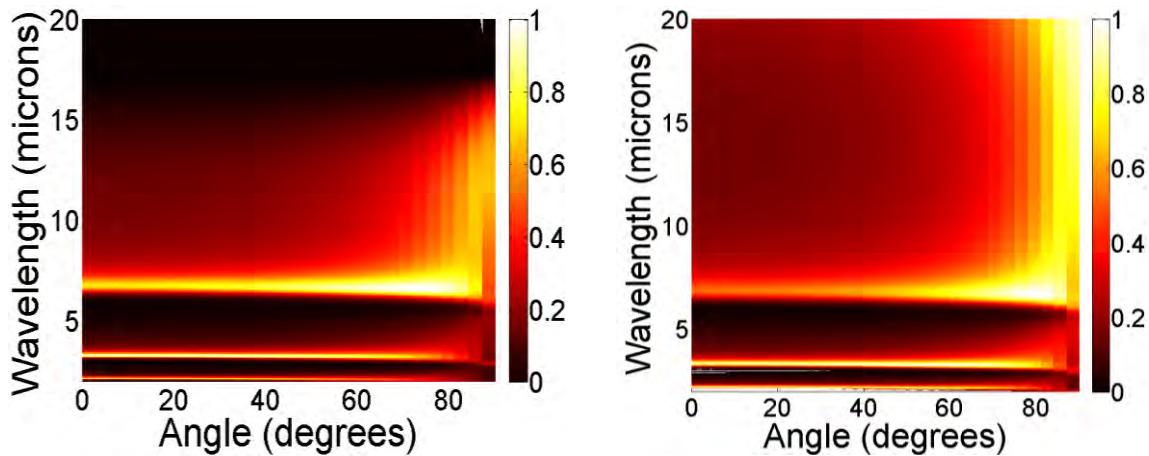


Figure 24. Calculated specular emittance (p-pol) for a Ag-Ge-Ag resonating structure at 294 K (left) and 500 K (right) between 2-20 μm . Thicknesses of constituent materials are 6-700-200 nm, respectively.

Sample 2: Fabrication

The Ag and Ge layers of Sample 2 were also deposited using a HIPIMS deposition technique. An SEM micrograph of Sample 2 looking down along surface normal at 45,000 \times magnification is shown in Figure 25. Surface roughness of the top Ag layer again appeared negligible with respect to IR wavelengths.

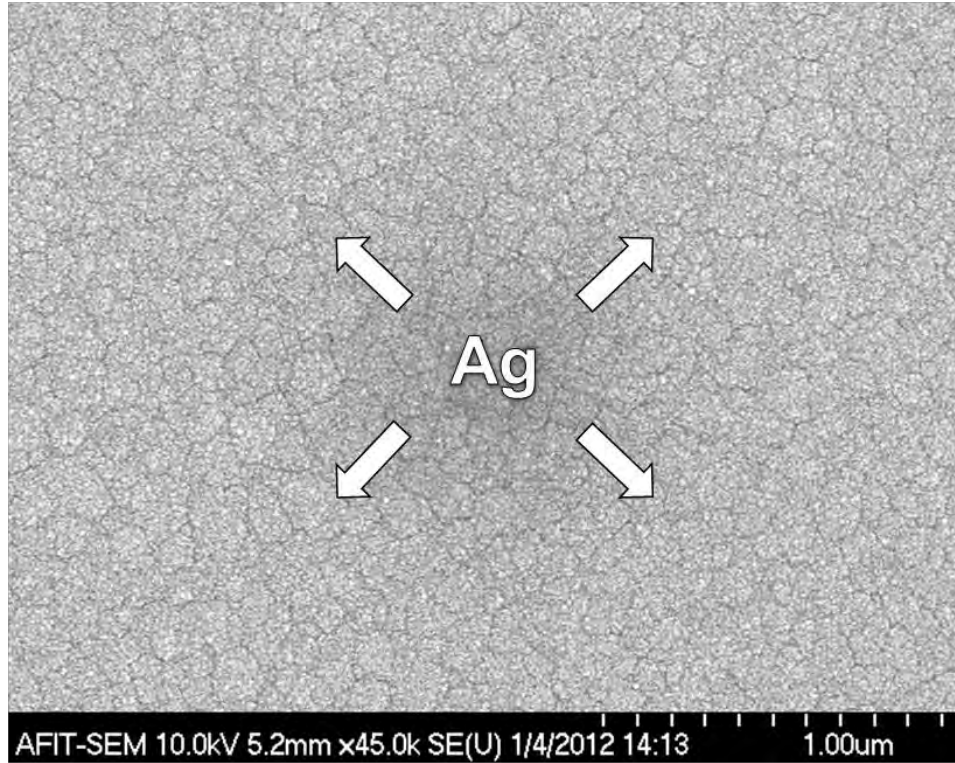


Figure 25. SEM micrograph of the top Ag surface of a Ag-Ge-Ag multilayer with thicknesses 6-700-200 nm, respectively. Ag and Ge layers were deposited via a High Power Impulse Magnetron Sputtering (HIPIMS) technique. Micrograph was taken at 45,000 \times magnification.

Sample 2: Reflectance Measurements

Reflectance measurements for this sample were also taken using the IR-VASE. Spectral reflectance of this truncated resonator from 1.7-29 μm is shown in Figure 26. As with Sample 1, these data were collected in 1 $^\circ$ increments from 25-80 $^\circ$ (from surface normal). Reflectance dips were observed at 2.6, 7.8, and 12 μm . The absorption bands encountered at 2.6 and 7.8 μm are attributed to cavity resonances that are inherently reliant on the length of the cavity, specifically the thickness of the IR-transparent Ge medium where the cavity response is the primary means of spectrally selective absorptance.

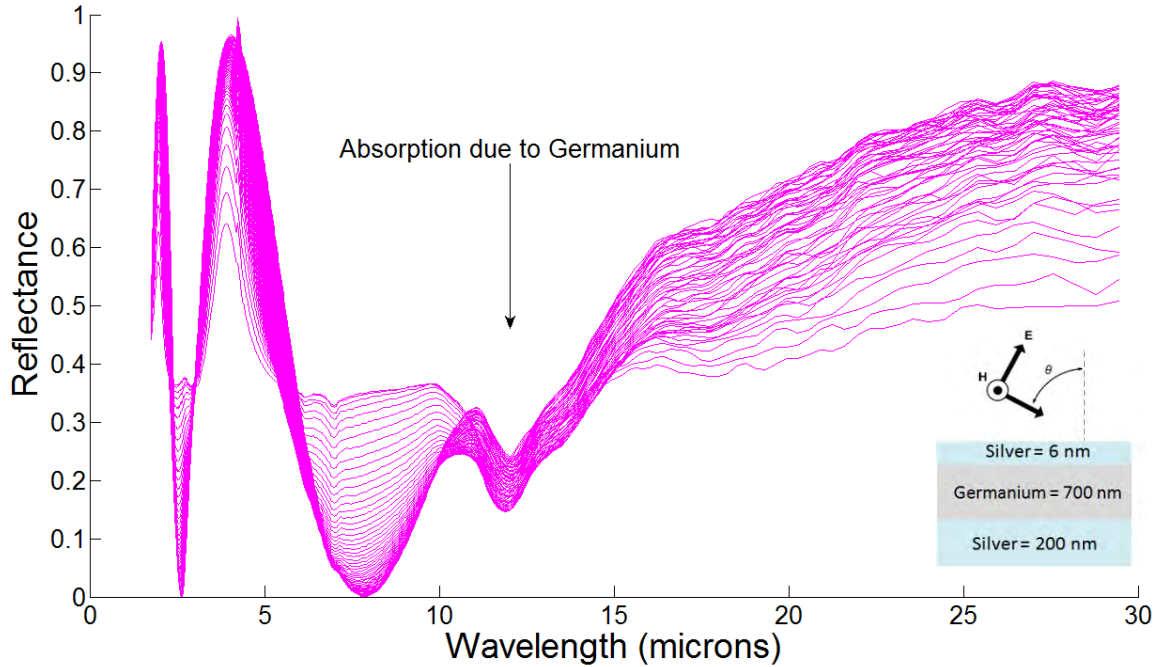


Figure 26. Spectral reflectance (p-pol) of a Ag-Ge-Ag truncated resonator (6-700-200 nm) between 1.7 and 29 μm . Reflectance measurements were taken using a J. A. Woollam Infrared Variable Angle Spectroscopic Ellipsometer (IR-VASE).

Ultimately, absorption around 12 μm will be attributed to an inherent property of the HIPIMS-deposited Ge. Bulk Ge is not known to be absorptive at this wavelength. This absorption was evident in the reflectance results for the thinner Sample 1 (6-240-160 nm) but not to the same degree seen in Sample 2's results. The stronger absorption seen in Sample 2's measurements is thought to stem from a Ge layer that is approximately three times thicker relative to Sample 1's Ge layer. The amorphous microstructure of the deposited Ge may be the driver for this unexpected absorption. Rationale for this speculation will be discussed later.

Figure 27 shows a close-up of the spectral reflectance from 1.7-15 μm in 10° increments between 25-75°. The sharp increase (spike) in measured reflectance at 4.26 μm is due to absorption of the carbon dioxide (CO_2) molecule in the ambient air.

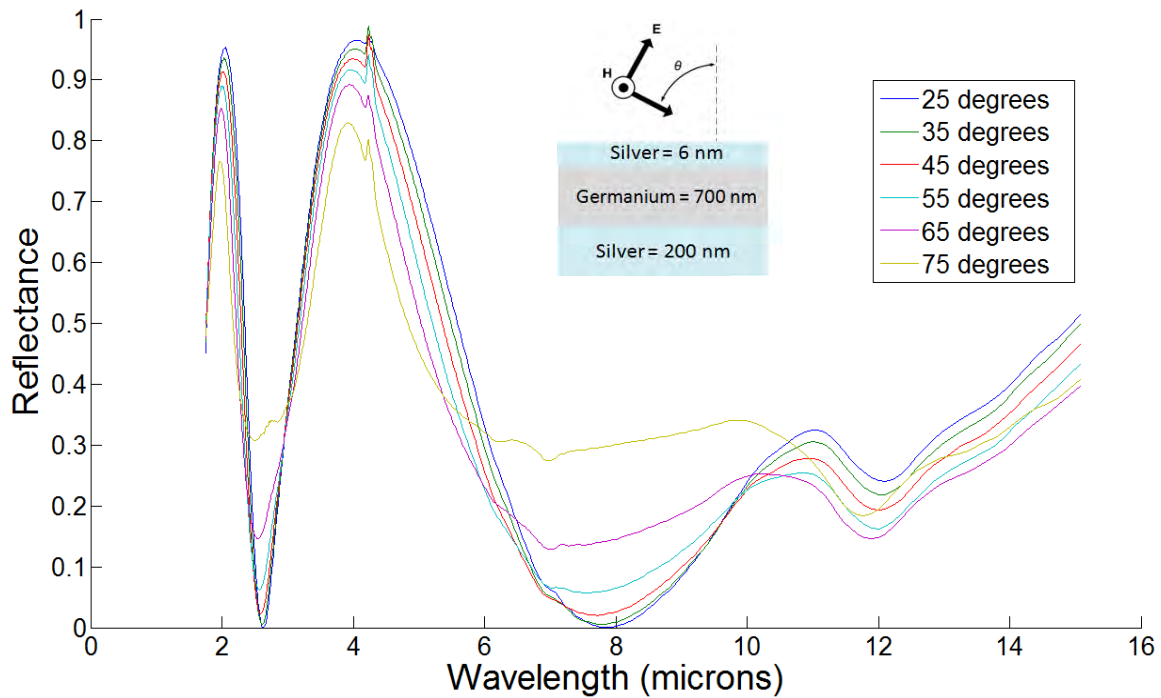


Figure 27. Spectral reflectance (p-pol) of a Ag-Ge-Ag truncated resonator (6-700-200 nm) between 1.7 and 15 μm . Reflectance measurements were taken using the J. A. Woollam Infrared Variable Angle Spectroscopic Ellipsometer (IR-VASE).

Invoking Kirchhoff's law again, spectral angular emittance is assumed to equal one minus reflectance. Figure 28 shows a comparison between spectral emittance calculated with theory to that derived from spectral reflectance of Sample 2 measured using the IR-VASE.

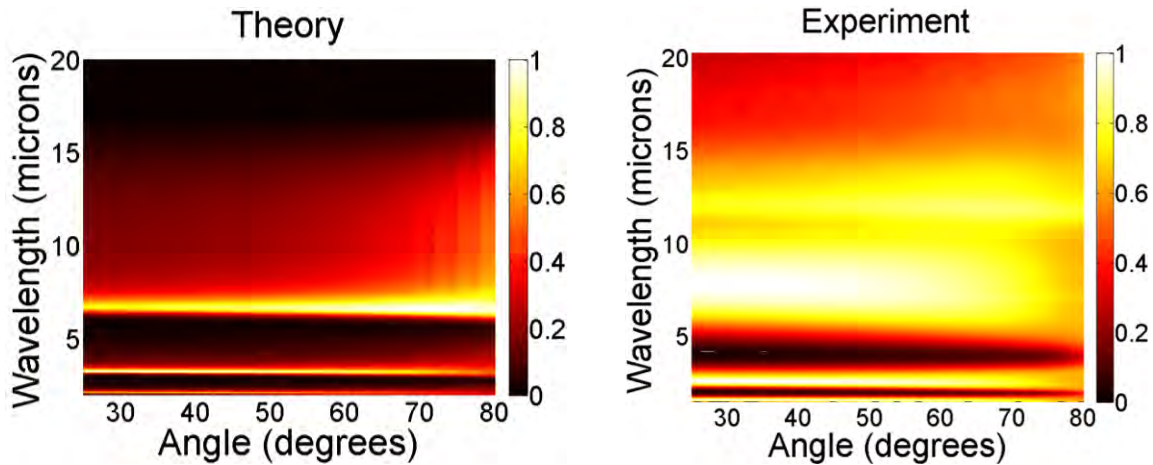


Figure 28. Comparison (p-pol) between the theoretical emittance results (left) and experimental emittance results (right) found through measurements taken using a J. A. Woollam Infrared Variable Angle Spectroscopic Ellipsometer (IR-VASE) for a Ag-Ge-Ag resonating structure with thicknesses 6-700-200 nm, respectively.

There were three resonances observed between 2 and 20 μm , and centered at 1.6, 2.64, and 7.75 μm . The measured emittance band centered at 7.75 μm was five times the spectral bandwidth of the calculated emittance centered at 7 μm that used bulk optical constants from Palik [44]. Since this sample was deposited using the same equipment and conditions as Sample 1, it is also possible here that the optical constants of the HIPIMS-deposited Ag and Ge are different from those published in Palik. Spectroscopic ellipsometry will be discussed next to verify the thicknesses of the constituent materials and derive respective optical constants to further investigate the cause of the differing results.

Spectroscopic Ellipsometry

Ellipsometric measurements were taken for Sample 1 from wavelengths 1.7-20 μm using the IR-VASE. Using J. A. Woollam's VASE32 software, models were fit to the ellipsometric measurements to extract the optical constants of the HIPIMS-deposited

materials. The VASE32 modeling tool also helped to verify the thicknesses of the individual layers since layer thickness is one of many parameters that can be fit.

The VASE32 software comes with a default library of models for common dielectrics, metals, and semiconductors applicable to IR wavelengths. These models can be based on published material properties or empirical data. Default Ge and Ag models from the IR library were used as a baseline for building a final model representative of the actual structure. New models were generated for the HIPIMS-deposited Ge and Ag called “mcconnell ge 2” and “mcconnell silver 2”, respectively. Figure 29 shows a screen capture of the layered structure used to model Sample 1 (6-240-160 nm) using VASE32 with associated thicknesses.

2	(mcconnell silver 2) Coupled to #0	2.541 nm
1	mcconnell ge 2	199.985 nm
0	mcconnell silver 2	1 mm

Figure 29. Screen capture from the J. A. Woollam VASE32 software of a modeled multilayer structure with associated thicknesses.

The thinner top Ag layer (2.541 nm) was coupled to the bottom “mcconnell silver 2” layer (1 mm) since they were the same material and this helped the convergence of the fitted model to the measured results. Determining the thickness of the constituent materials requires that a portion of the IR radiation travel through the entire film and return back through the structure to the detector. With the presence of absorption in Sample 1, this likely affected the layer thicknesses fit in the model. Therefore, the layer thicknesses that are determined from a given model will not always be exact. The ellipsometric measurements, amplitude ratio Ψ and phase difference Δ , made using the

IR-VASE on Sample 1 are shown with their associated fitted models in Figure 30. Note that three angles of incidence were used to collect ellipsometric data. Use of multiple data sets in the regression analysis increased confidence in the uniqueness of the resulting optical constants.

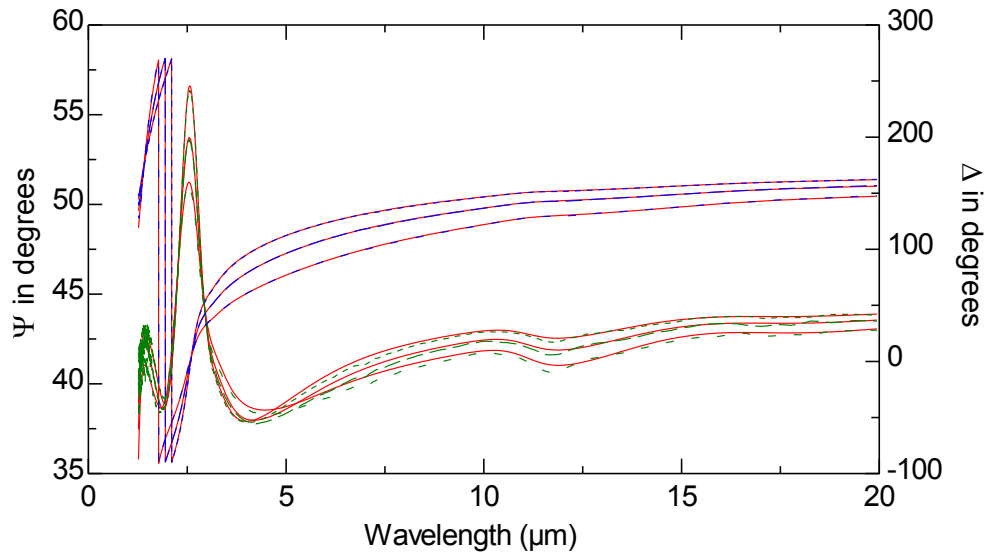


Figure 30. Amplitude ratio Ψ (green) and phase difference Δ (blue) ellipsometric measurements made using a J. A. Woollam Infrared Variable Angle Spectroscopic Ellipsometer (IR-VASE) on a Ag-Ge-Ag truncated resonator, Sample 1 (6-240-160 nm), with associated model fits (red).

Mean square error of the fitted model using the VASE32 software was 1.675° .

Thirty-two different parameters were used to fit this model to the measured ellipsometric data. From the fitted model and thickness predictions, wavelength-dependent optical constants of the constituent materials can be derived. Figure 31 and Figure 32 show the calculated complex index of refraction for the HIPIMS-deposited Ag (mcconnell silver 2) and Ge (mcconnell ge 2), respectively.

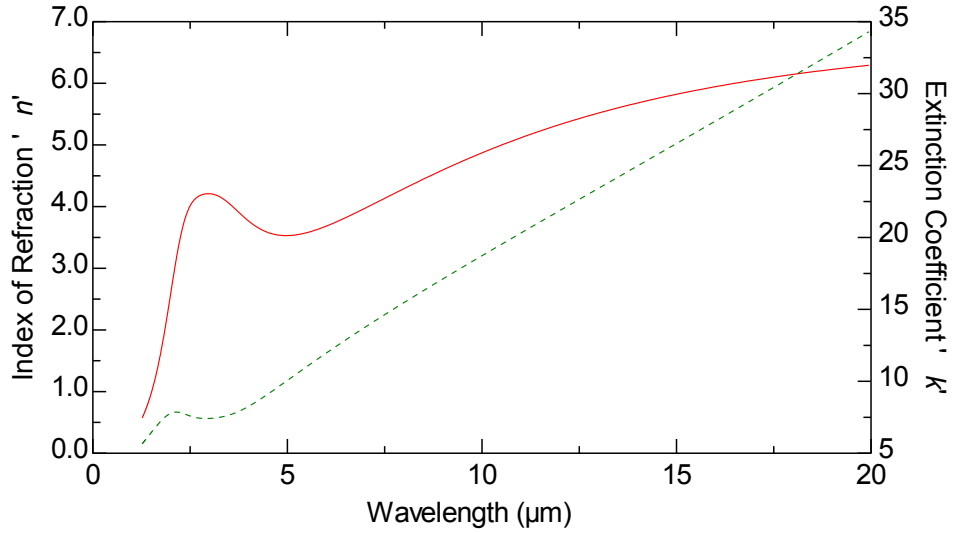


Figure 31. Calculated complex index of refraction, n (red) and k (green), for a Ag layer deposited via a High Power Impulse Magnetron Sputtering (HIPIMS) technique.



Figure 32. Calculated complex index of refraction, n (red) and k (green), for a Ge layer deposited via a High Power Impulse Magnetron Sputtering (HIPIMS) technique.

An evaluation of calculated complex index of refraction for the HIPIMS-deposited Ag layers is plotted in Figure 33 and Figure 34 and compared against the bulk

optical constants reported in Palik [44] for real and imaginary parts of the refractive index n and k , respectively.

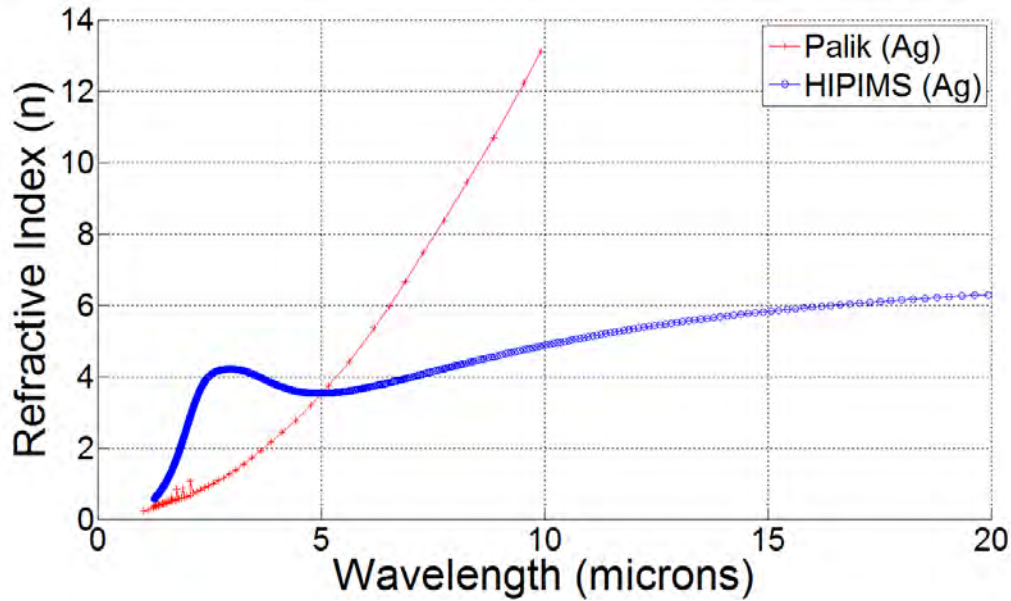


Figure 33. The real part of the index of refraction (n) for HIPIMS-deposited Ag compared with bulk optical constants reported in Palik [44] over IR wavelengths.

HIPIMS values for refractive index n deviated significantly from the literature values, especially around the absorbing region of Sample 2 at approximately $3 \mu\text{m}$. The Palik values rose quickly with increasing wavelength while the HIPIMS data leveled to a value of 6 toward longer IR wavelengths. For the imaginary part of the refractive index k shown in Figure 34, the HIPIMS values tended towards the literature values from $1\text{-}2 \mu\text{m}$. Beyond $2 \mu\text{m}$, the HIPIMS-deposited Ag deviated to far lower values when compared to Palik data. Refractive index values n and k for Ge are compared in Figure 35 and Figure 36, respectively.

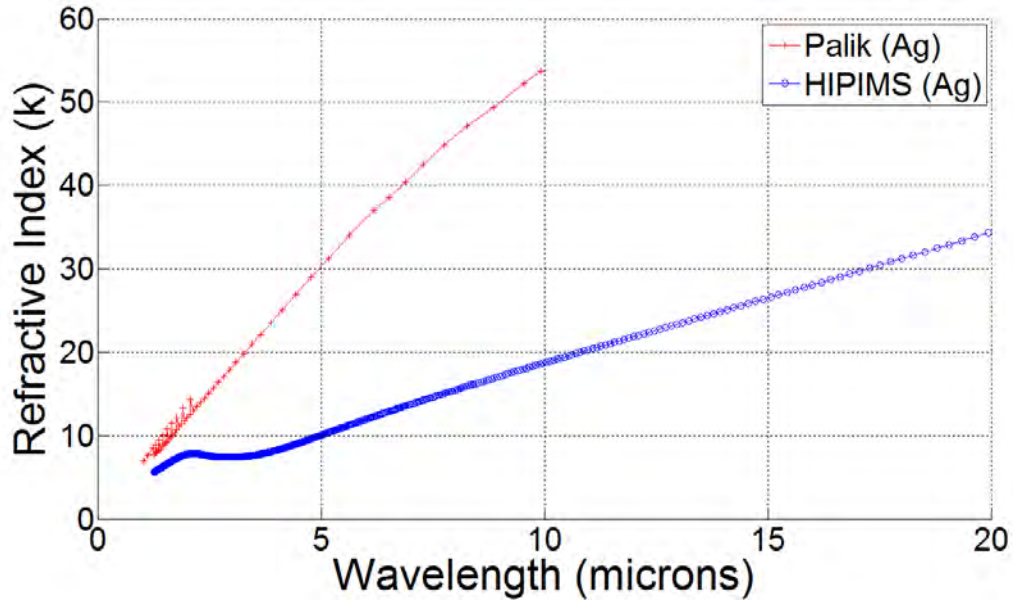


Figure 34. The imaginary part of the index of refraction (k) for HIPIMS-deposited Ag compared with bulk optical constants reported in Palik [44] over IR wavelengths.

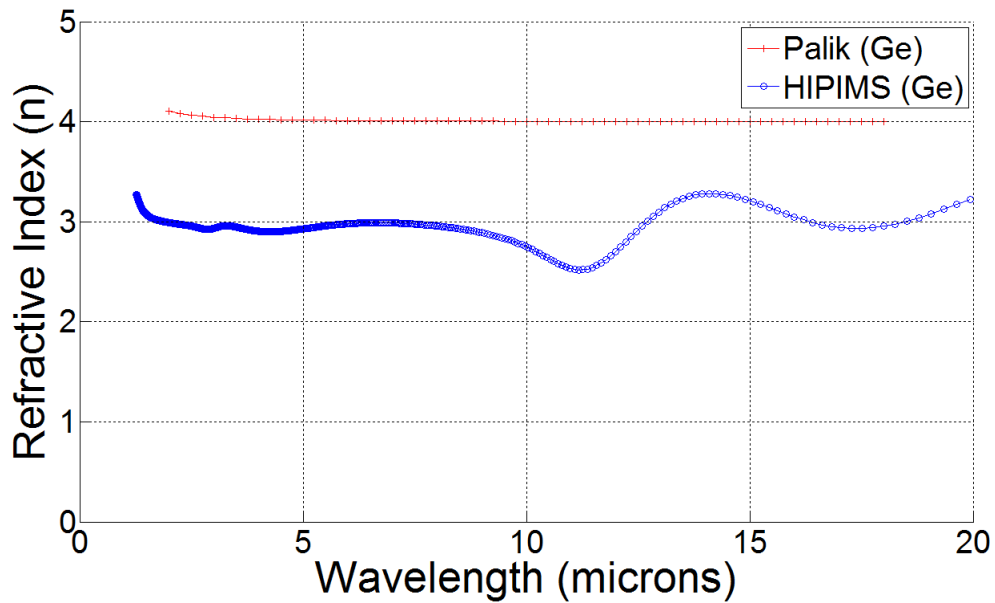


Figure 35. The real part of the index of refraction (n) for HIPIMS-deposited Ge compared with bulk optical constants reported in Palik [44] over IR wavelengths.

HIPIMS values for the refractive index n were lower than the crystalline values in Palik for Ge across all measured IR wavelengths. The HIPIMS values also exhibited an

oscillatory behavior around the 12- μm band where the inherent absorption in the deposited Ge was speculated (Figure 26). Typically, the imaginary component of germanium's refractive index is considered negligible at IR wavelengths. However, the calculated HIPIMS values for the imaginary part of the refractive index k were non-zero over the majority of IR wavelengths where the ellipsometric data was measured.

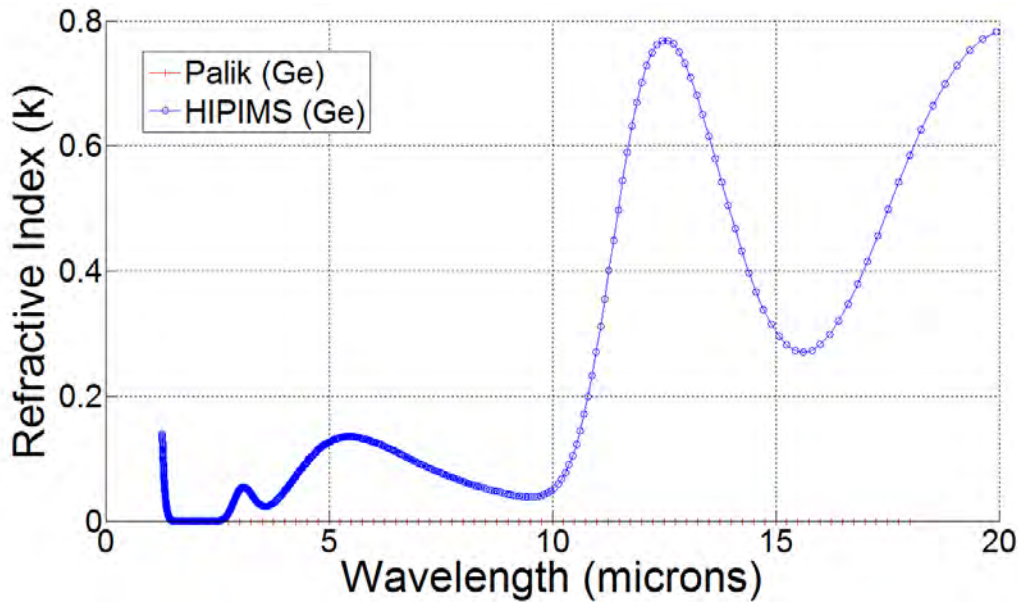


Figure 36. The imaginary part of the index of refraction (k) for HIPIMS-deposited Ge compared with bulk optical constants reported in Palik [44] over IR wavelengths.

Finally, these derived optical constants were fed back into the theoretical model for the truncated resonator using the MATLAB® implemented RCWA. Figure 37 shows a comparison of the new theoretical model, with derived optical constants for the HIPIMS-deposited Ag and Ge, to the emittance results calculated from IR-VASE measurements for Sample 1 (6-240-160 nm). This new model computed expected results that were closer to those observed from the IR-VASE experiment.

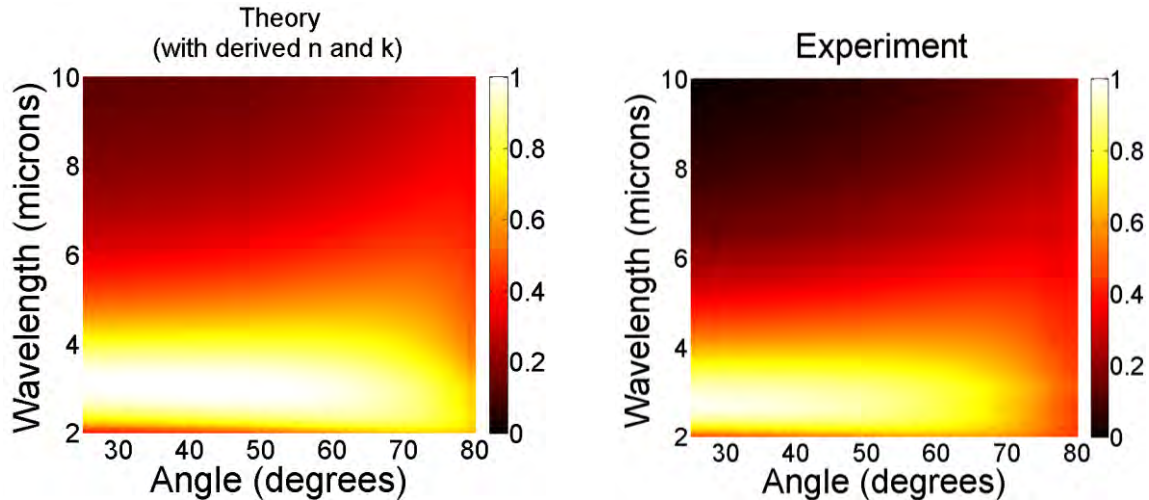


Figure 37. Comparison (p-pol) between new theoretical emittance predictions that include derived optical constants (n and k) for the HIPIMS-deposited materials (left) to those calculated (right) from measurements taken using a J. A. Woollam Infrared Variable Angle Spectroscopic Ellipsometer (IR-VASE) for a Ag-Ge-Ag resonating structure with thicknesses 6-240-160 nm, respectively.

Bulk optical constants from Palik [44] were used to calculate the original analytical design (Figure 28). Since any deposited material is amorphous to some degree, the material properties can be anticipated to vary due to contrasts in microstructure and purity. The accuracy of derived optical constants from spectroscopic ellipsometry is highly dependent on the accuracy of the model built to fit the results. These effective optical constants do not assume over-layers due to oxidation or surface roughness unless specifically accounted for in the model. For Sample 2 (6-700-200 nm), Figure 38 shows a comparison of the new model to experimental results. Again, the new model that accounted for the composition of the HIPIMS-deposited Ag and Ge yielded a dispersion relationship closer to that observed from the IR-VASE experiment. Intrinsic Ge absorption at 12 μm that was not present in a previous comparison (Figure 28) is now accounted for here, but note that emittance is significantly less pronounced in the

theoretical model in comparison to the experimental measurements taken with the IR-VASE.

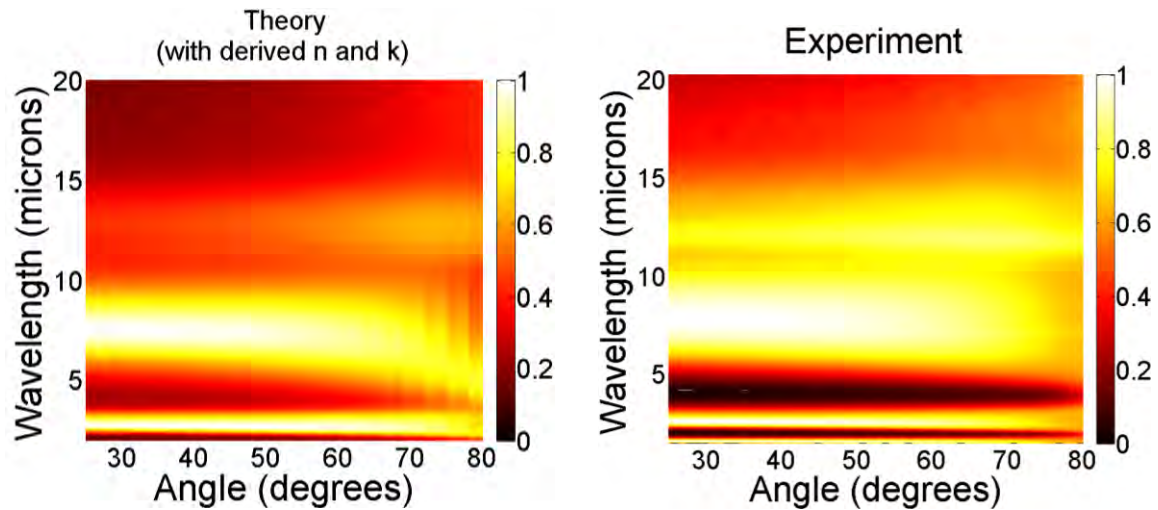


Figure 38. Comparison (p-pol) between new theoretical emittance predictions that include derived optical constants (n and k) for the HIPIMS-deposited materials (left) to those calculated (right) from measurements taken using a J. A. Woollam Infrared Variable Angle Spectroscopic Ellipsometer (IR-VASE) for a Ag-Ge-Ag resonating structure with thicknesses 6-700-200 nm, respectively.

Radiance Measurements and Calculating Emittance

Spectral emittance associated with thermally heated structures was derived from radiance measurements taken using an in-house AFIT emissometer. Sample 2 was thermally excited to various temperatures and its radiance was measured by a Bomem FTIR spectrometer. Figure 39 shows the measured spectral radiance captured by the Bomem FTIR spectrometer for Sample 2 at normal incidence and room temperature (297 K), overlaid with the theoretical radiance of an ideal blackbody also at 297 K.

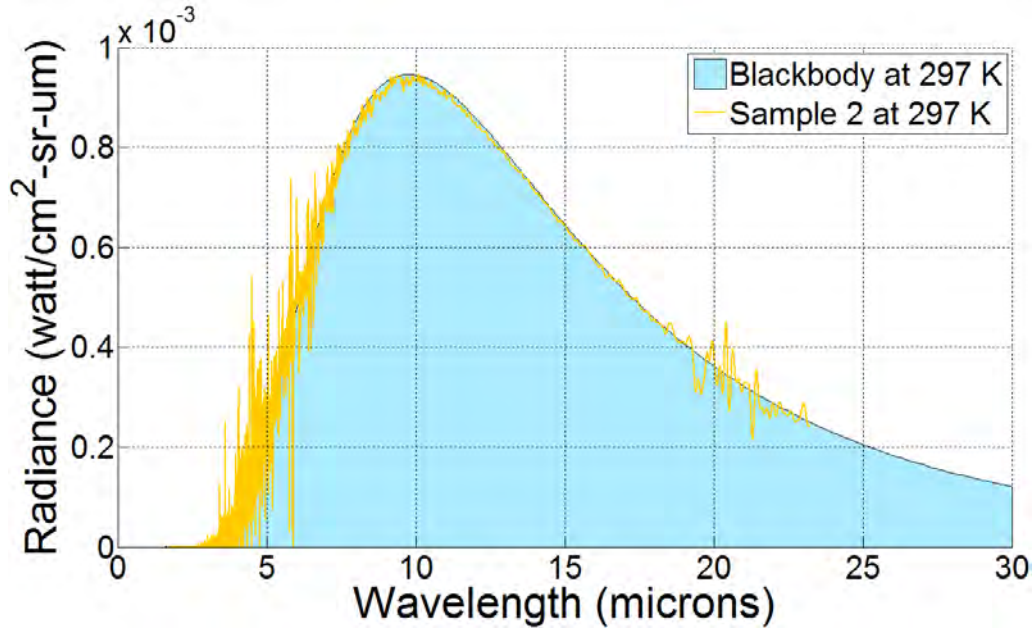


Figure 39. Spectral radiance measured by a MR-154 Bomem Fourier transform infrared (FTIR) spectrometer for Ag-Ge-Ag truncated resonator, Sample 2 (6-700-200 nm), at room temperature (297 K) overlaid with the theoretical radiance of an ideal blackbody also at 297 K.

The measured radiance of Sample 2 included contributions from self emission and the background reflecting off the sample back to the spectrometer. Significant noise was observed from 3-7 μm and 19-23 μm . Figure 39 shows that the radiance of the background dominated the spectral radiance measured by the spectrometer with the measured radiance trending very closely to the envelope of the Planckian distribution. The background was not blocked for this ambient measurement, so this was expected at room temperature where Sample 2 is in thermal equilibrium with the background.

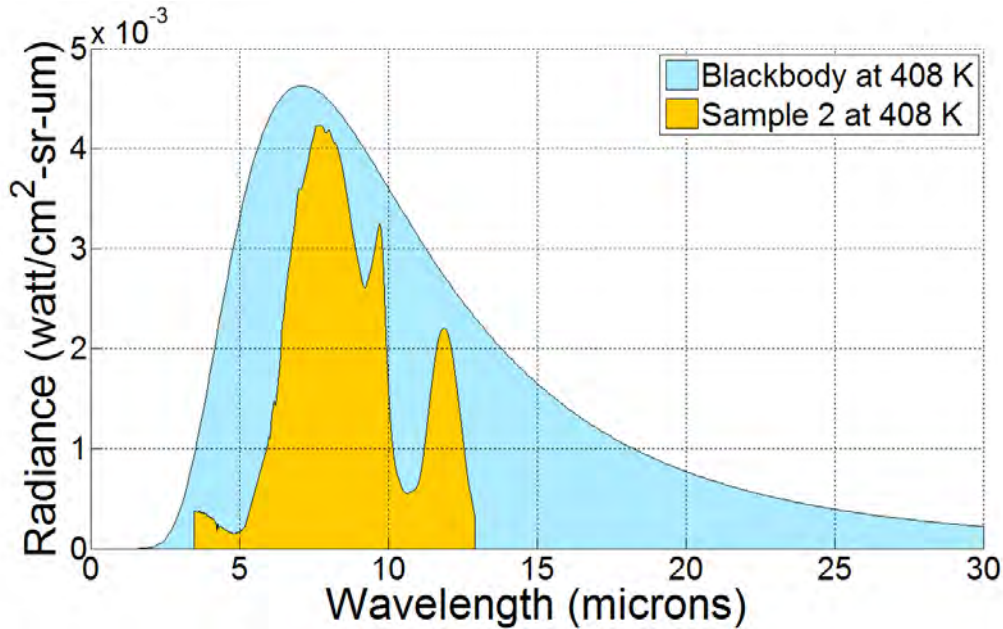


Figure 40. Spectral radiance measured by a MR-154 Bomem Fourier transform infrared (FTIR) spectrometer for Ag-Ge-Ag truncated resonator, Sample 2 (6-700-200 nm), at 408 K overlaid with the theoretical radiance of an ideal blackbody also at 408 K.

Figure 40 shows the measured spectral radiance for Sample 2 at 408 K overlaid with the theoretical radiance of a blackbody also at 408 K. Sample 2's measured radiance (orange) shown in Figure 40 is only shown for the measurement range captured by the Bomem FTIR. The measured radiance of Sample 2 exhibited behavior akin to a selective emitter when thermally excited above room temperature to 408 K. Further, Sample 2's selective emission occurred approximately near the same wavelengths predicted by inferring emittance from reflectance measurements where the 7.8- μm emission peak was attributed to a cavity resonance and the 12- μm emission peak was attributed to intrinsic absorption in the HIPIMS-deposited Ge layer. An emission peak at approximately 9.7 μm was also observed from Sample 2 under thermal excitation that did not exist in the calculated emittance results using reflectance measurements. This

contribution could be attributed to strong, unaccounted tri-oxide, or O₃ (ozone), emittance at 9.7 μm that was excited through conduction to the air from the hot plate.

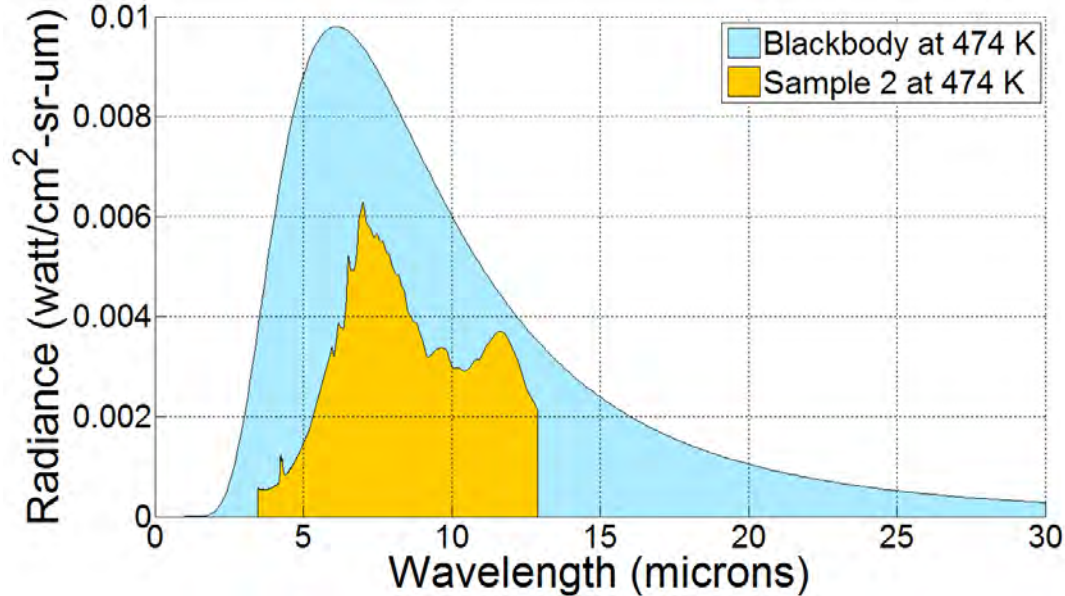


Figure 41. Spectral radiance measured by a MR-154 Bomem Fourier transform infrared (FTIR) spectrometer for Ag-Ge-Ag truncated resonator, Sample 2 (6-700-200 nm), at 473 K overlaid with the theoretical radiance of an ideal blackbody also at 473 K.

Figure 41 shows the measured radiance for Sample 2 at 473 K overlaid with the radiance of a blackbody also at 473 K. At 473 K, Sample 2 continued to behave as a selective emitter but the selectivity was less pronounced. At this temperature, Sample 2's radiance still tends towards the theoretical results predicted for this resonating structure with emission dominating at around 7.8 and 12 μm.

Figure 42 shows the measured radiance for Sample 2 thermally excited to 601 K and overlaid with the radiance distribution for a blackbody at 601 K. Sample 2's radiative behavior remained selective at 601 K with distinct emission peaks 7 and 12 μm.

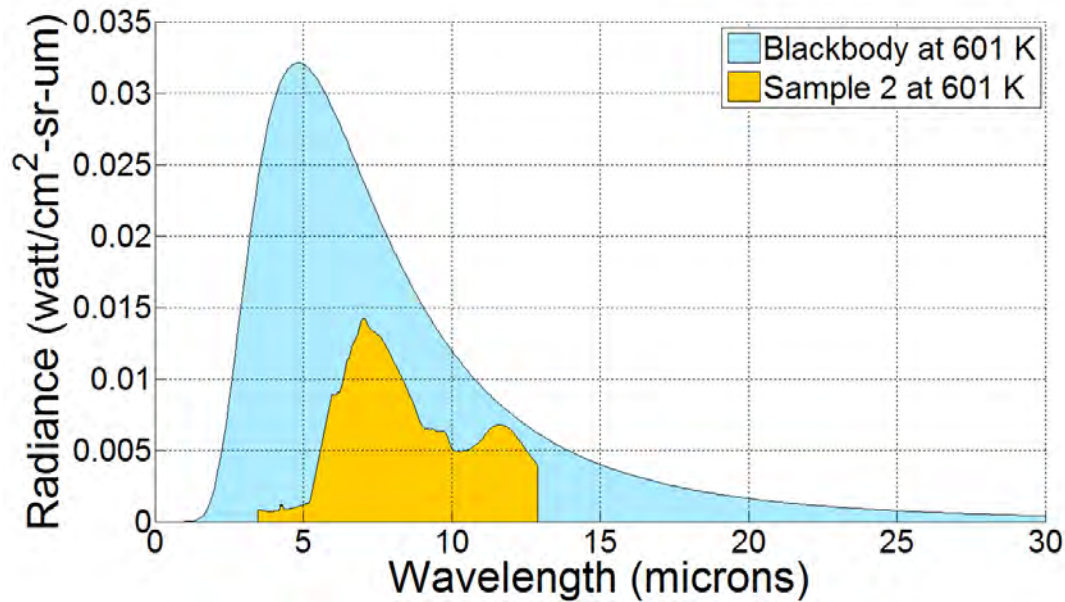


Figure 42. Spectral radiance measured by a MR-154 Bomem Fourier transform infrared (FTIR) spectrometer for Ag-Ge-Ag truncated resonator, Sample 2 (6-700-200 nm), at 601 K overlaid with the theoretical radiance of an ideal blackbody also at 601 K.

Using Equation (22), emittance as a function of wavelength was calculated from the radiance measurements obtained from AFIT's emissometer instrument. Two different sets of calculated emittance results for Sample 2 are shown in Figure 43. The blue data set was calculated from reflectance measurements taken with the IR-VASE and invoking Kirchhoff's law to assume that the radiation selectively absorbed by Sample 2 would also be selectively emitted for a body in thermal equilibrium (297 K in this case). The red data set represents the calculated emittance derived from radiance measurements of Sample 2 while thermally excited to 408 K.

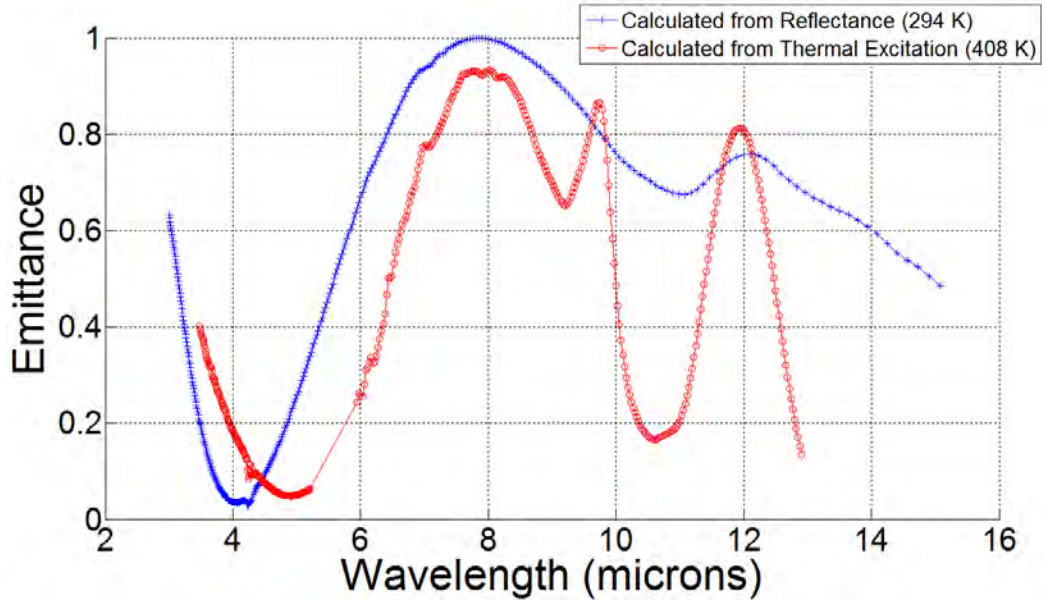


Figure 43. Calculated emittance results for Ag-Ge-Ag truncated resonator, Sample 2 (6-700-200 nm), from two data sets, one was calculated from reflectance measurements and invoking Kirchhoff's law to assume that the radiation selectively absorbed by Sample 2 at room temperature (297 K) is also selectively emitted (blue), and the other data set represents the calculated emittance derived from radiance measurements of Sample 2 while thermally excited to 408 K (red).

The two sets of emittance results shown in Figure 43 followed the same general behavior. The 7.8- μm and 12- μm emittance peaks observed during thermal excitation were centered at that same peaks predicted from inferred emittance. The emittance peak at 9.7 μm , attributed to strong O_3 interactions, was also evident in the emittance calculated from thermal excitation. This was expected from the radiance measurements observed Figure 40. This phenomenon did not exist in any form in the calculated results using reflectance measurements from the IR-VASE.

Figure 44 shows the same comparison of calculated emittance results for Sample 2 except the emittance was derived from radiance measurements taken while Sample 2 was heated to 473 K.

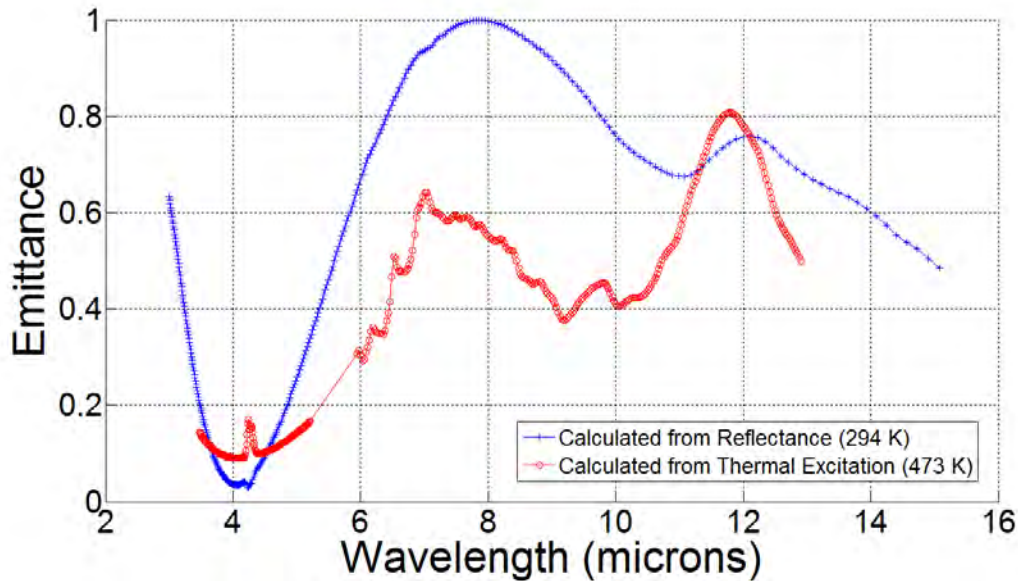


Figure 44. Calculated emittance results for Ag-Ge-Ag truncated resonator, Sample 2 (6-700-200 nm), from two data sets, one was calculated from reflectance measurements and invoking Kirchhoff's law to assume that the radiation selectively absorbed by Sample 2 at room temperature (297 K) is selectively emitted (blue), and the other data set represents the calculated emittance derived from radiance measurements of Sample 2 while thermally excited to 473 K (red).

The 473-K emittance data sets follow the same general behavior. However, direct calculation of emittance from thermal excitation did not align with the indirectly calculated emittance as well as it did while Sample 2 was at 408 K. Significant suppression of the emittance peak centered at 7.75 μm predicted from reflectance measurements was observed. On average, the emittance between 6 and 10 μm calculated from thermal excitation was 40% lower than that calculated from reflectance. The high emittance (0.8) at 12 μm was the dominant emittance peak at this temperature. CO_2 absorption spike at 4.26 μm was clearly obvious in Figure 44.

Figure 45 shows a final comparison of Sample 2 calculated emittance results after heating the structure to 601 K. Again, selective radiative behavior was observed for Sample 2 and it behaved in a similar manner to that exhibited while at 473 K. The

emittance peak at 12 μm was approximately 0.05 higher than that observed in Figure 44. The emittance peak predicted from reflectance measurements and invoking Kirchhoff's law centered at 7.75 μm was present but was also 40% lower on average between 6 and 10 μm .

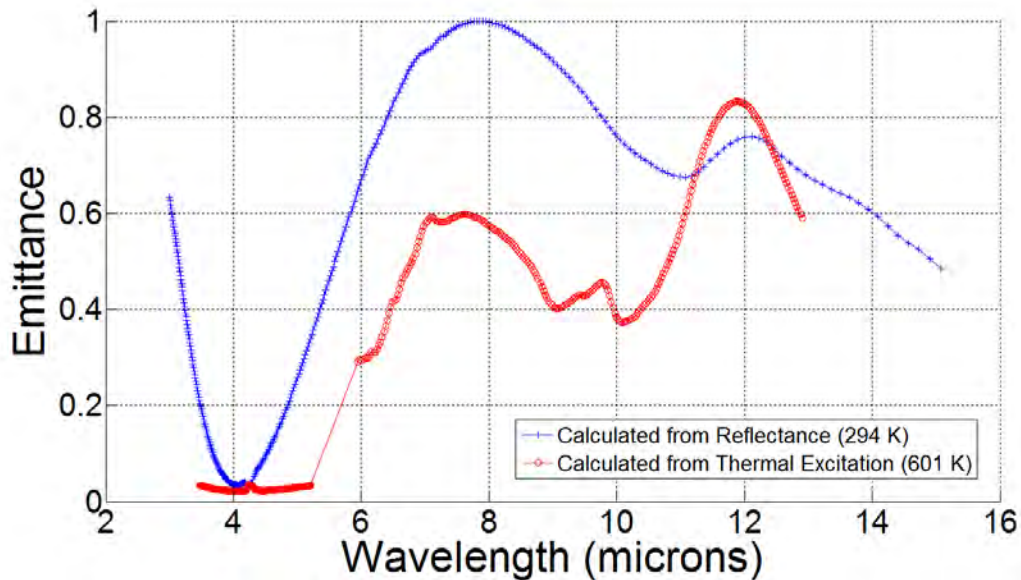


Figure 45. Calculated emittance results for Ag-Ge-Ag truncated resonator, Sample 2 (6-700-200 nm), from two data sets, one was calculated from reflectance measurements and invoking Kirchhoff's law to assume that the radiation selectively absorbed by Sample 2 at room temperature (297 K) is selectively emitted (blue), and the other data set represents the calculated emittance derived from radiance measurements of Sample 2 while thermally excited to 601 K (red).

To pinpoint the cause of the contrasting emittance results, new SEM micrographs were taken of both samples to examine the surface morphology and overall microstructure of the tri-layer. Figure 46 shows an SEM micrograph of Sample 1 after it was thermally excited to 408 K using a hot plate. The surface geometry of the truncated resonator had indeed changed from its original state seen in Figure 19. The surface of Sample 1 appeared to be no longer uniform and instead consisted of spherical collections of Ag particles ranging from 10-40 nm in diameter. Both samples reached thermal

equilibrium with the hot plate very rapidly given their small size (approximately 2.5 cm × 2.5 cm) and thin profile. Sample 1 reached thermal equilibrium with the hot plate at 408 K for approximately 2 minutes before it was allowed to cool.

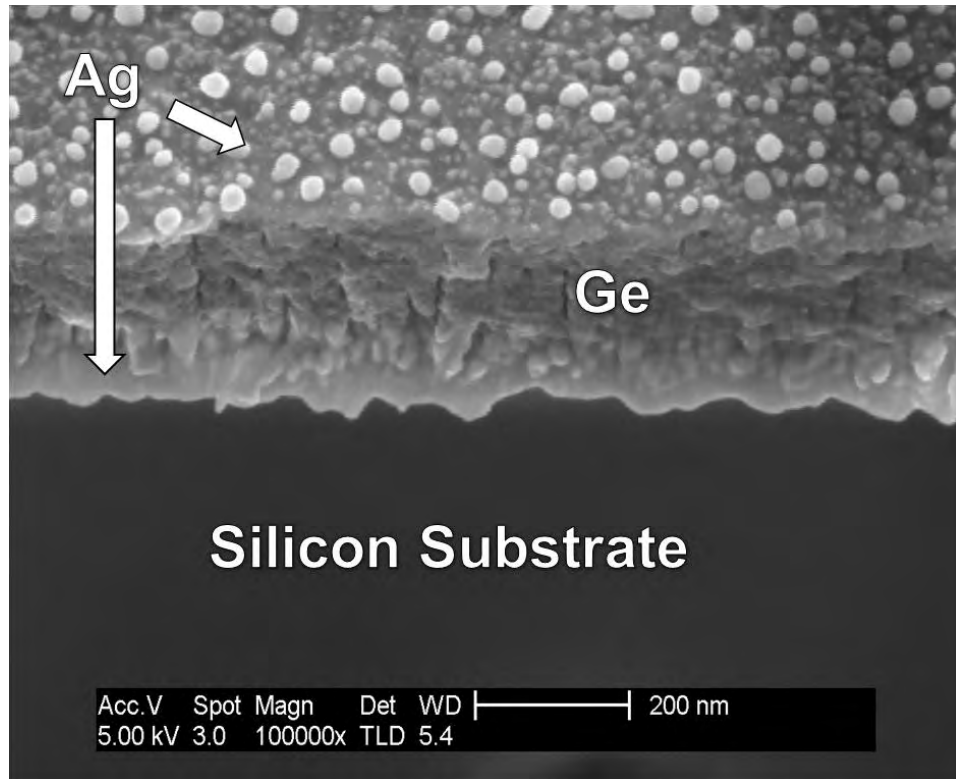


Figure 46. SEM micrograph of a Ag-Ge-Ag truncated resonator (6-240-160 nm) on a silicon substrate after being thermally excited to 408 K. Ag and Ge layers were deposited via a High Power Impulse Magnetron Sputtering (HIPIMS) technique. Micrograph was taken at 100,000× magnification and at an angle of 35° from surface normal.

To characterize the effect of this new surface morphology on Sample 1's performance, IR-VASE reflectance measurements were retaken. Figure 47 shows the measured spectral reflectance of Sample 1 from 1.7-6 μm in 10° increments from 25-75° before (blue) and after (red) being thermally excited to 408 K.

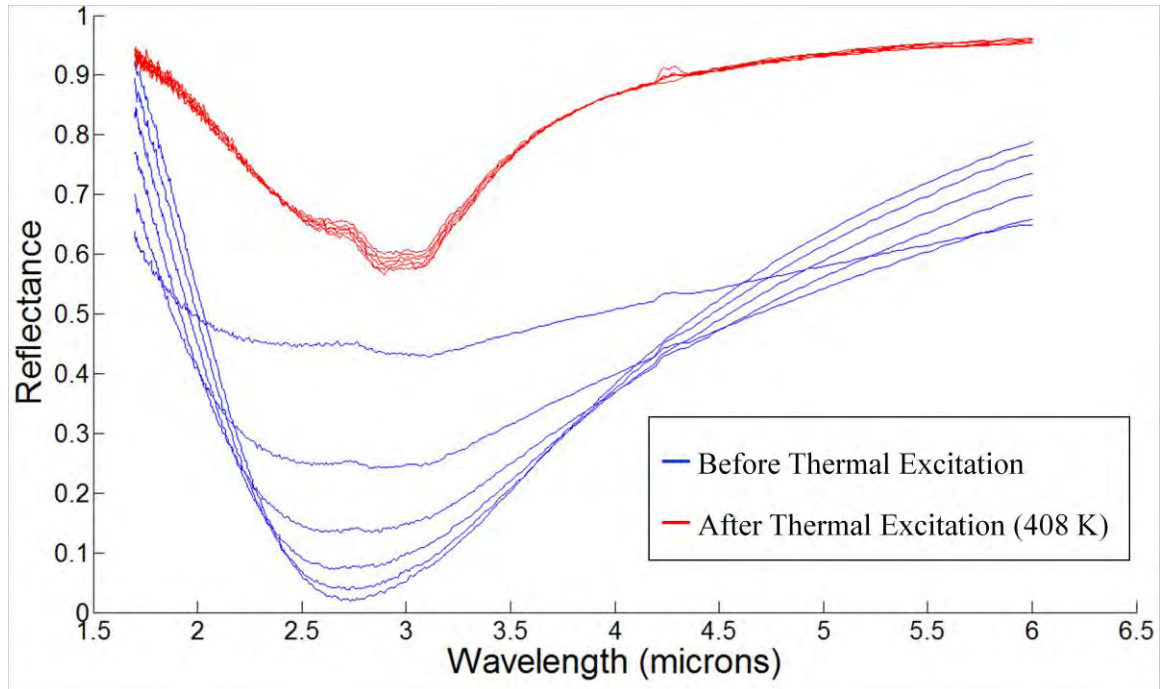


Figure 47. Measured spectral reflectance (p-pol) of a Ag-Ge-Ag truncated resonator (6-240-160 nm) between 1.7 and 6 μm and in 10° increments between $25\text{-}75^\circ$ of incident angle before (blue) and after (red) being thermally excited to 408 K. Reflectance measurements were taken using the J. A. Woollam Infrared Variable Angle Spectroscopic Ellipsometer (IR-VASE).

Sample 1's spectral reflectance was significantly impacted by the new surface morphology. The previously observed reflectance dip at 2.6 μm climbed from a minimum of 0.025 before thermal excitation, to 0.575 after. Also shown in Figure 47, the angular sensitivity after thermal excitation of Sample 1 was negligible compared to its angular response before.

An SEM micrograph of Sample 2 after it was thermally excited to 601 K is shown Figure 48. The surface of Sample 2 also consisted of spherical collections of Ag particles, except these aggregates were not as densely arranged as those found on Sample 1. The diameter of each Ag sphere again ranged from approximately 10-40 nm. The Ge layer and bottom Ag layer seen here are less amorphous than previously observed in Figure 19. The columnar microstructure that existed before being thermally excited is

not as distinct now. Sample 2 reached thermal equilibrium with the hot plate at three different temperatures above ambient, 408 K, 473 K and 601 K, each time for approximately 2 minutes.

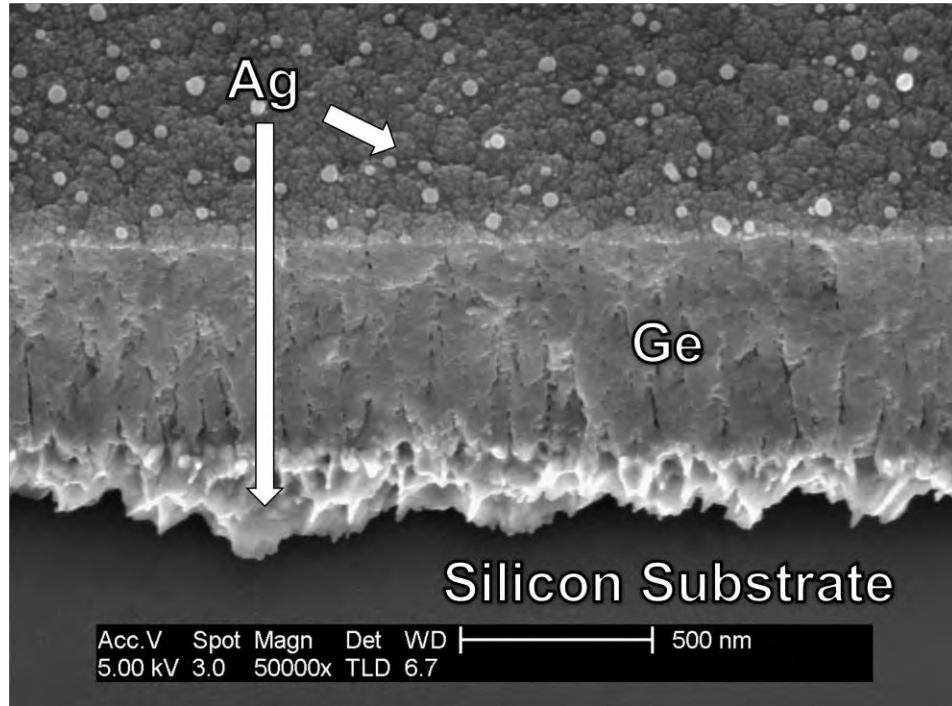


Figure 48. SEM micrograph of a Ag-Ge-Ag truncated resonator (6-700-200 nm) on a silicon substrate after being thermally excited to 601 K. Ag and Ge layers were deposited via a High Power Impulse Magnetron Sputtering (HIPIMS) technique. Micrograph was taken at 50,000 \times magnification and at an angle of 35 $^\circ$ from surface normal.

Figure 49 shows Sample 2's associated measured spectral reflectance from 1.7-15 μm in 10 $^\circ$ increments from 25-75 $^\circ$ before (blue) and after (red) being thermally excited to 601 K. The reflectance dip at 2.6 μm was less pronounced after thermal excitation but still reached a minimum of 0.35 at 25 $^\circ$. This was not the case for the resonance at 7.75 μm where the measured reflectance value went from approximately 0 to 0.6.

Furthermore, the absorption at 12 μm due to the HIPIMS-deposited Ge was not

appreciably affected but the reflectance did rise by 0.1-0.2 depending on the incident angle. The CO₂ spike was lower in magnitude after thermal excitation. In addition, a small dip at 7 μm was more distinct in the measured reflectance with respect to the results before heating Sample 2. This is attributed to absorption by H₂O molecules in the ambient air.

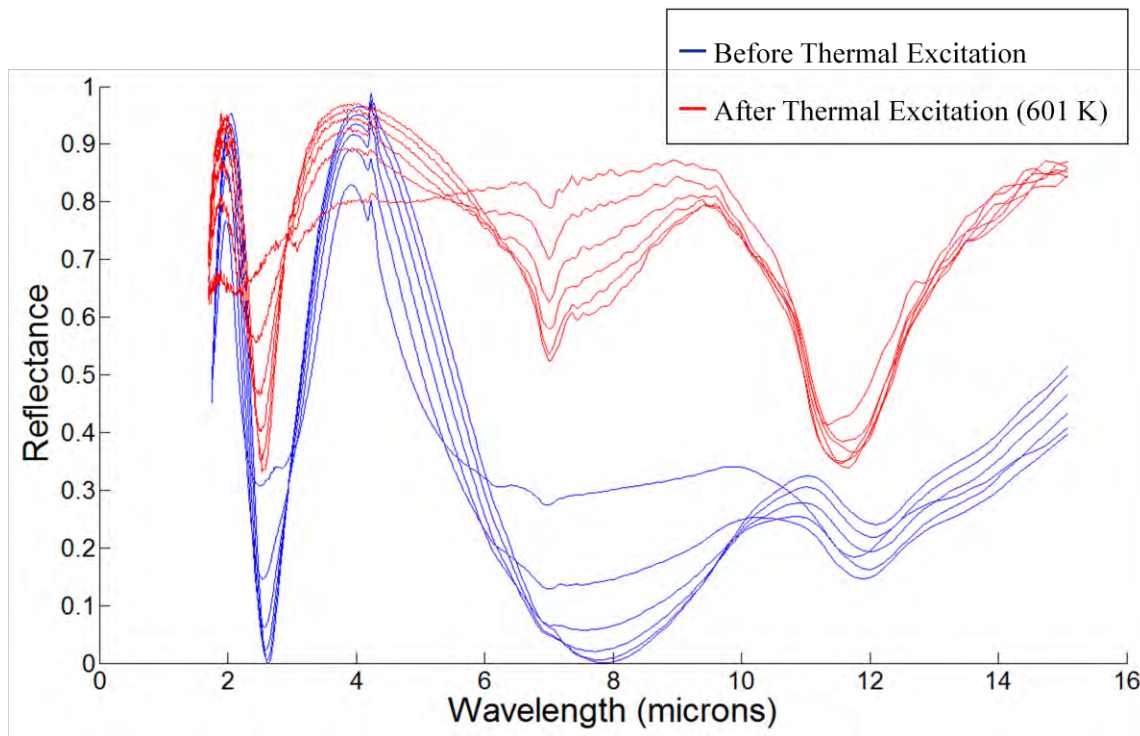


Figure 49. Measured spectral reflectance (p-pol) of a Ag-Ge-Ag truncated resonator (6-700-200 nm) between 1.7 and 15 μm and in 10° increments between 25-75° of incident angle before (blue) and after (red) being thermally excited to 601 K. Reflectance measurements were taken using the J. A. Woollam Infrared Variable Angle Spectroscopic Ellipsometer (IR-VASE).

Figure 50 shows a final comparison between emittance directly calculated from thermal excitation versus inferred emittances calculated from IR-VASE reflectance measurements before and after a 601 K heat treatment. The emittance calculated indirectly from reflectance after the heat treatment process tends closer to the calculated

emittance found under thermal excitation. This was expected given the change in Sample 2's surface morphology. Conversely, the inferred emittance post-heat did underestimate the emittance directly observed at 601 K. The contrasting emittance results are attributed to the temperature-dependent optical constants of the HIPIMS-deposited Ag and Ge materials.

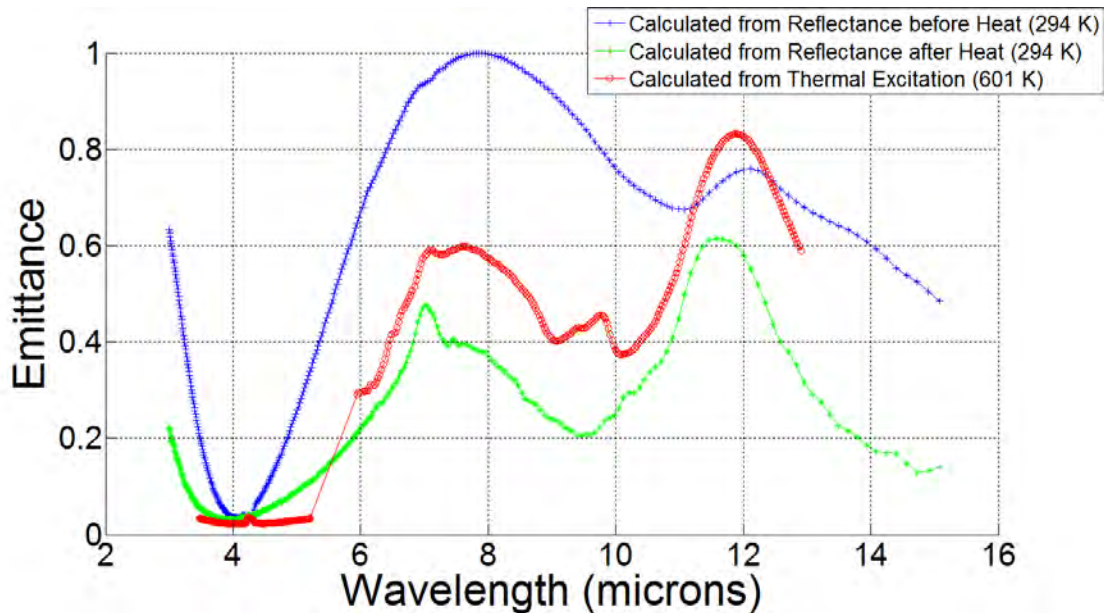


Figure 50. Calculated emittance results for Ag-Ge-Ag truncated resonator, Sample 2 (6-700-200 nm), from three data sets – two data sets were calculated from reflectance measurements before (blue) and after (green) being thermally excited to 601 K and invoking Kirchhoff's law to assume that the radiation selectively absorbed by Sample 2 at room temperature (297 K) is selectively emitted, and the last data set represents the calculated emittance derived from radiance measurements of Sample 2 while thermally excited to 601 K (red).

The Sellmeier and free-electron/Drude models were used to find temperature-dependent optical constants for Ag and Ge in Chapter IV. The specular emittance contour plots for Sample 2 shown in Figure 24 were calculated at room temperature using published optical constants from Palik [44] and at 500 K using modeled high-temperature optical constants. Based on the normal emittance trend between the 294 K and 500 K

contour plots shown in Figure 24, the emittance was expected to decrease at IR wavelengths above 6 μm . In contrast, the calculated emittance from 601 K thermal excitation was higher for almost all represented wavelengths when compared to emittance calculated from invoking Kirchhoff's law. To rigorously characterize the true high-temperature refractive index of the HIPIMS-deposited materials, ellipsometric measurements made at requisite high temperatures would be necessary to accurately predict the emittance of this structure.

Summary

This chapter discussed the design, fabrication, and characterization of two truncated multilayer resonator samples, Samples 1 (6-240-160 nm) and 2 (6-700-200 nm). Spectroscopic ellipsometry was used to verify the material properties of the actual materials used and helped to understand the optical observables measured using the IR-VASE and emissometer. Lastly, inferred emittance was compared to directly calculated emittance to investigate the validity of invoking Kirchhoff's law to find the expected emission of a given structure. In the next chapter, findings from a 3-D patterned thermal emitter will be presented.

VI. Analysis and Results – Hybrid PC-Multilayer

Chapter Overview

This chapter describes the design considerations and initial fabrication results for a 3-D hybrid PC-multilayer structure.

Hybrid PC-Multilayer Design

RCWA is very efficient when it comes to calculating diffraction efficiencies over a wide range of incident angles and wavelengths. However, RCWA is somewhat limited to simpler multi-dimensional geometries such as grating structures. Arbitrary shapes can be modeled to a degree but they require their geometric profiles to be discretized, which introduces numerous discontinuities in the calculation which may lead to unphysical results. Multiphysics simulation and modeling tools are useful for the case of arbitrary geometries and sometimes offer visual depictions of physical phenomena that can be helpful. For this reason, CST was utilized to simulate the performance of the PC-multilayer structure. Spectrally and spatially selective emittance centered at $6\ \mu\text{m}$ was the objective for this 3-D structure. In addition, a realistic design using FIB milling was desired for eventual fabrication of this hybrid thermal emitter using local resources at AFRL's MCF.

Dielectric and magnetic dispersive materials can be represented in CST using built-in dispersion models such as Debye, Drude, Lorentz, and Gyrotropic. However, incorporating highly dispersive material parameters that were user-defined significantly increased the computation time of the 3-D CST simulation. In the interest of time, the optical constants from Palik [44] and those ellipsometrically obtained as in Chapter V

were not used in CST for the following simulations. The implication of not using user-defined dispersive materials and using the default “Lossy” type materials from the CST material library is that the dispersive nature of the respective optical constants are approximated using a 1-D surface impedance model. This will account for electric fields penetrating into the material but only to within a skin depth δ of a given material whose thickness is represented by the following formula

$$\delta = \sqrt{\frac{2}{\omega\mu\sigma}}, \quad (20)$$

where σ is the electric conductivity. Further, due to this approximation, inherent absorption by conducting materials was not fully captured in these simulations. To further drive the 3-D CST simulation time down, the Ag-Ge-Ag multilayer with embedded square hole array was approximated as a single slab of Ag with embedded hole array. Thus, the structure of the original design was retained but the selective emittance that came as a result of the multilayer would not be represented in these simulations.

To validate that the single Ag slab approximation with non-dispersive material properties would offer results representative of those acquired using with the full Ag-Ge-Ag structure with Palik’s dispersive values, both structures were simulated for a p-pol (TM) normally incident plane wave. The period between each hole was 6 μm and the diameter of each hole was 3 μm for both structures. In Figure 51, CST simulated reflectance at normal incidence for a Ag-Ge-Ag (6-240-160 nm) hole array structure using Palik data is compared to a single Ag (400 nm) slab hole array structure using the default Ag from the CST material library. Note that the reflectance dip at 6.5 μm is retained in the results from the approximated structure. As expected, the reflectance dip

at 2.6 μm is not represented in the approximated structure with a single layer of Ag since the cavity set up by the Ag-Ge-Ag multilayer does not exist. Since the overall behavior of the approximated hole array structure was retained, this construct was utilized for the remainder of this chapter.

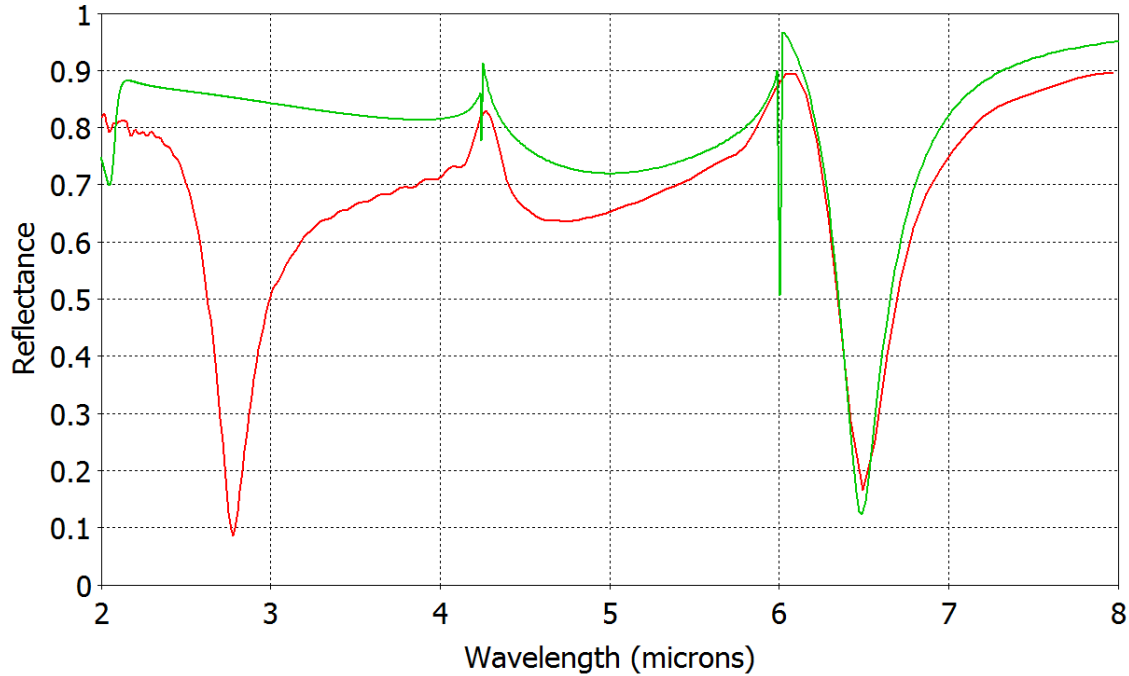


Figure 51. CST simulated reflectance at normal incidence for a Ag-Ge-Ag (6-240-160 nm) hole array structure (red) using optical constants from literature (Palik) and a single Ag (400 nm) slab hole array structure (green) using the default Ag from the CST material library.

Realistically, the PC-multilayer will reside on some substrate during fabrication. To account for this, a 20-nm Si substrate was added to the model. Though this substrate thickness is not actually realistic, its purpose was to emulate the physical structure more closely to capture as much physical phenomena as possible without greatly increasing the computational time of the simulation. For the PC-multilayer, the simulated model consisted of two layers, a single Ag slab and a Si substrate, using the “Silver (lossy)” and

“Silicon (lossy)” CST materials, respectively. The Ag layer was a $6 \times 6\text{-}\mu\text{m}^2$ slab, 400-nm thick, with a 3- μm diameter hole in the center of the slab. The Si layer was also $6 \times 6\text{-}\mu\text{m}^2$, 20-nm thick, and was homogeneous throughout. Figure 52 shows one unit cell of the PC-multilayer structure that was constructed in the CST simulation environment.

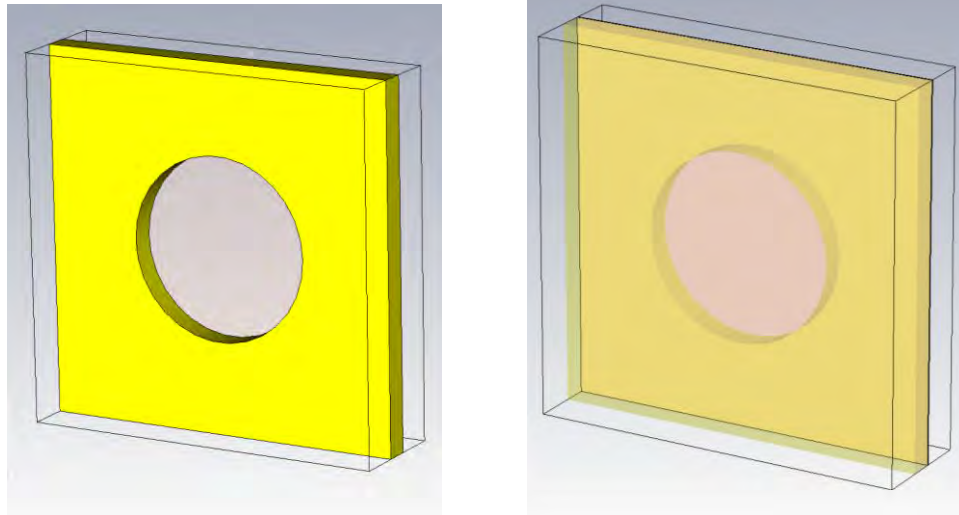


Figure 52. Illustration of one unit cell of the PC-multilayer structure as constructed in the CST simulation environment. The Ag slab with hole at its center is highlighted on the left with a transparent Si substrate behind it. On the right, the Si substrate is highlighted behind the transparent Ag layer.

CST’s frequency-solver (f-solver) was used since it is capable of off-normal plane wave illumination. Unit Cell boundary conditions were used to repeat the structure, seen in Figure 52, periodically along the x and y axes to model a square array. The PC-multilayer was illuminated with both p-pol (TM) and s-pol (TE) plane waves for θ from $0\text{-}60^\circ$ in 5° increments, and for ϕ equal to 0° and 45° . Figure 53 illustrates the periodic boundary conditions implemented in CST and the respective coordinate system superimposed over the PC-multilayer unit cell.

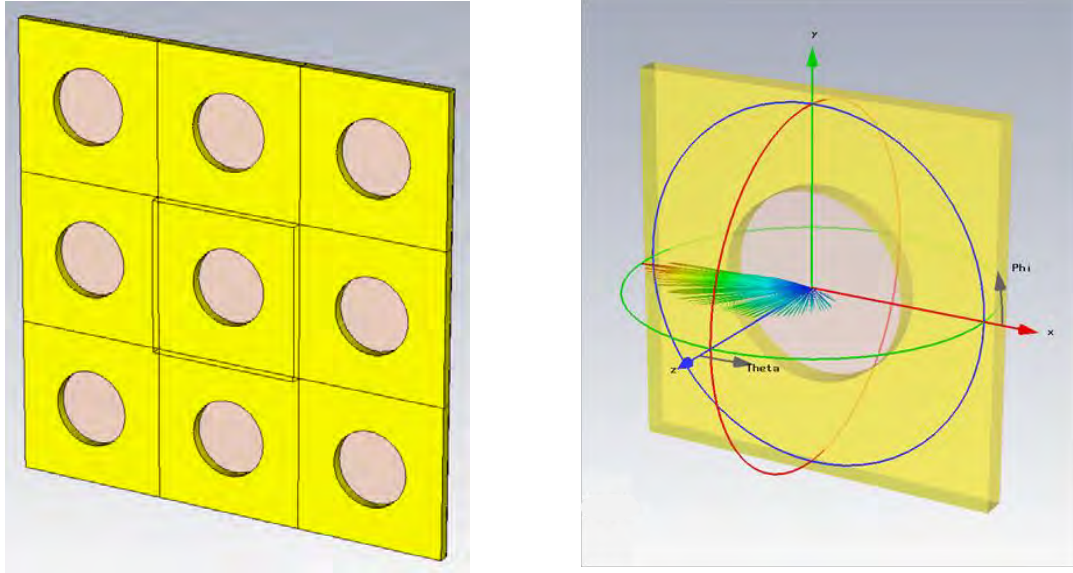


Figure 53. Illustration of the periodic boundary conditions implemented on the hybrid photonic crystal-multilayer in CST (left) and the respective coordinate system superimposed over one unit cell (right).

For a p-pol plane wave incident at $\phi = 0^\circ$, Figure 54 shows the simulated spectral reflectance and transmittance from the PC-multilayer for θ from 0-60°. This structure behaves as a transmission filter, selectively reflecting most wavelengths, but allowing some wavelengths to transmit through the structure. For s-pol incident radiation, Figure 55 shows the simulated spectral reflectance and transmittance from the PC-multilayer for θ from 0-60° for a plane wave also incident at $\phi = 0^\circ$.

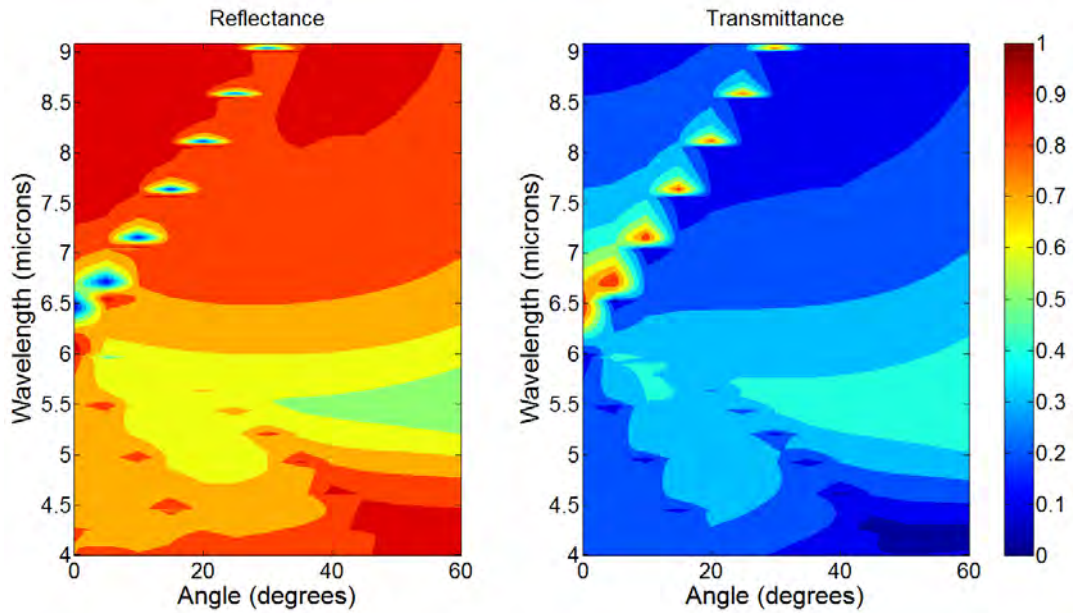


Figure 54. Simulated spectral reflectance and transmittance from the hybrid photonic crystal-multilayer for θ from 0-60° from a p-pol (TM) plane wave incident at $\phi = 0^\circ$.

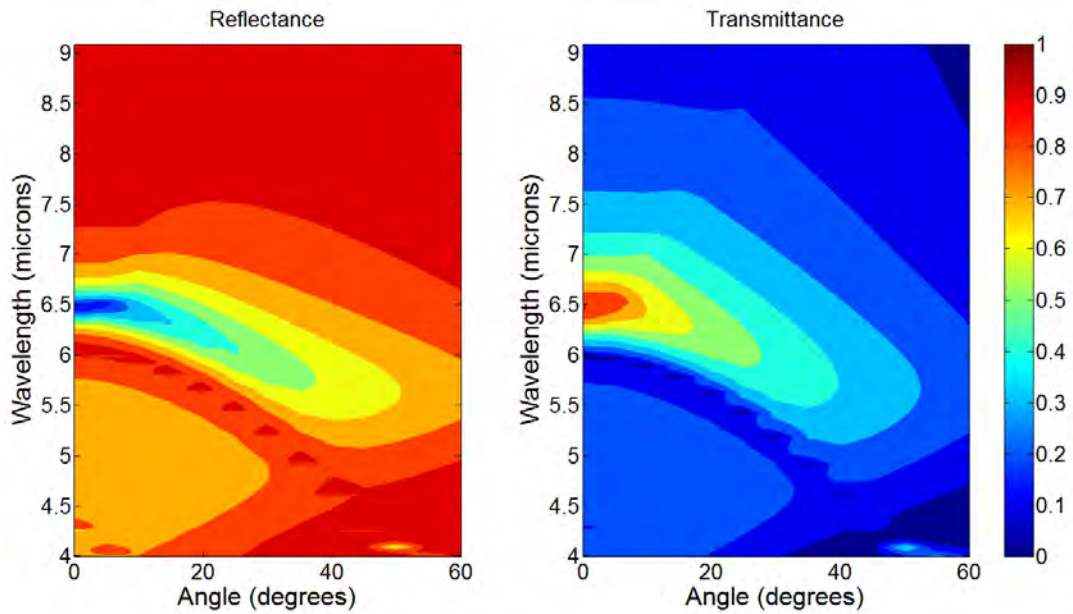


Figure 55. Simulated spectral reflectance and transmittance from the hybrid photonic crystal-multilayer for θ from 0-60° from a s-pol (TE) plane wave incident at $\phi = 0^\circ$.

At normal incidence, transmission through the structure was observed at $6.5 \mu\text{m}$. The propagating modes near normal to 60° are recognized as cylindrical waveguide modes through the circular apertures considering their presence for s- and p-pol incident radiation and for both azimuthal orientations. The transmitted modes occurring at off-normal incident angles are attributed to plasmonic modes. Sub-wavelength hole arrays may perform as a band-pass filter, allowing longer wavelength to propagate while rejecting shorter wavelengths [64]. For bare, non-magnetic materials, TE-polarized (s-pol) surface waves are typically not supported [38]. Under s-pol incident radiation, it was apparent that most of the off-normal plasmonic propagating modes were suppressed except at shorter wavelengths below $6 \mu\text{m}$. Those propagating modes that are observed were attributed to constructive and destructive wave interference effects between neighboring holes in the square array. Further, increased angular transmittance at near-normal incident angles was observed for s-pol. This transmission band extended out to approximately 10° over a narrow band of wavelengths centered at $6.5 \mu\text{m}$.

For a p-pol plane wave incident at $\phi = 45^\circ$, Figure 56 shows the simulated spectral reflectance and transmittance from the PC-multilayer for θ from $0-60^\circ$. Figure 57 shows the simulated spectral reflectance and transmittance from the PC-multilayer for θ from $0-60^\circ$ for a s-pol plane wave also incident at $\phi = 45^\circ$. The dispersion of propagating modes at this azimuthal orientation did change. This was expected given the change in problem geometry at $\phi = 45^\circ$. Here, cylindrical waveguide modes and plasmonic modes are evident for both polarizations. However, the s-pol surface waves that were thought to be suppressed, clearly exist for incident polarization. Therefore, the

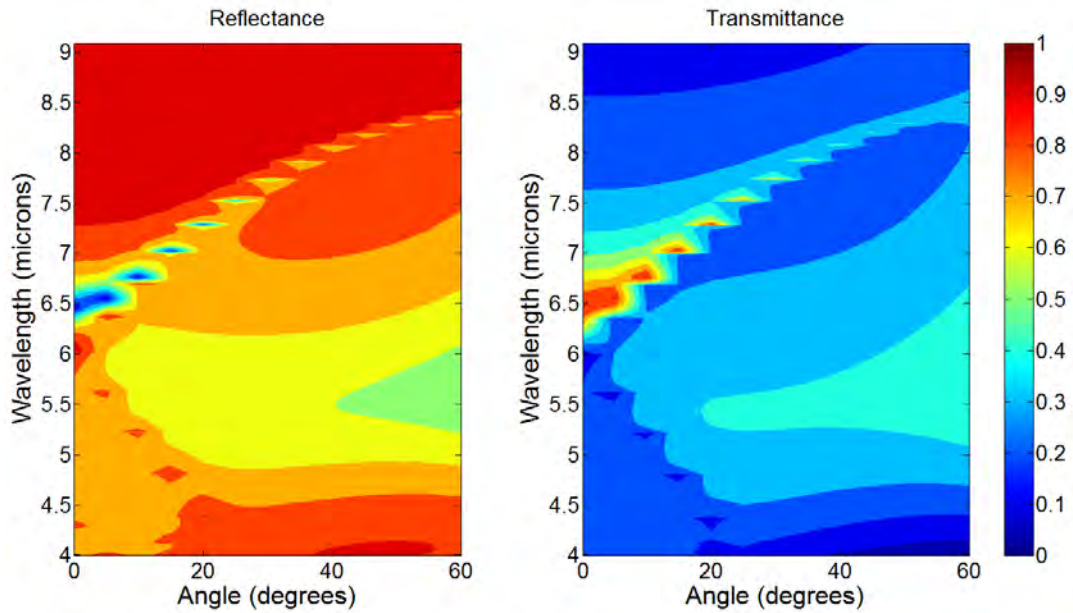


Figure 56. Simulated spectral reflectance and transmittance from the hybrid photonic crystal-multilayer for θ from 0-60° from a p-pol (TM) plane wave incident at $\phi = 45^\circ$.

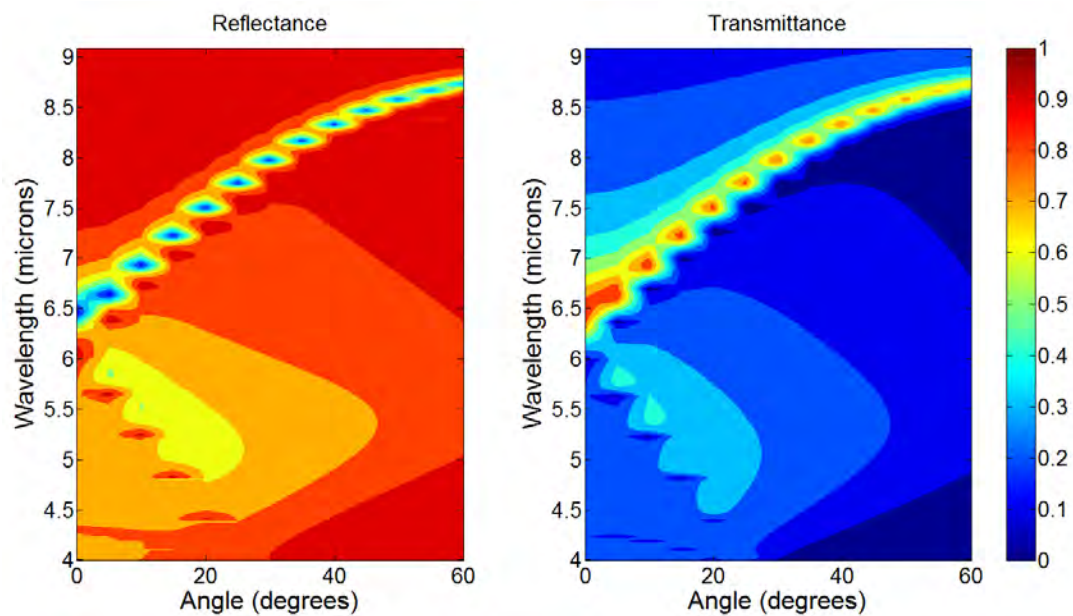


Figure 57. Simulated spectral reflectance and transmittance from the hybrid photonic crystal-multilayer for θ from 0-60° from a s-pol (TE) plane wave incident at $\phi = 45^\circ$.

suppression of propagating modes at $\phi = 0^\circ$ for s-pol incident radiation (Figure 55) is now thought to stem from coupling interactions between neighboring holes. Also, note from Figure 57 that the propagating plasmonic modes below $6 \mu\text{m}$ observed in Figure 55 no longer pass through the filter at $\phi = 45^\circ$. This behavior supports the original claim that the s-pol propagating modes at $\phi = 0^\circ$ were due to coupling of neighboring holes at shorter wavelengths.

Hybrid PC-Multilayer: Initial Fabrication

Fabrication of a PC-multilayer structure, consisting of a hole array embedded inside of a multilayer resonator, required two main steps. The first step involved HIPIMS deposition of the Ag and Ge layers through AFRL's Material and Manufacturing Directorate. The second step involved FIB milling the multilayer using an FEI Nova 600 Nanolab (Serial Number: D117) located in the AFRL MCF. This FIB system was fitted with a Sidewinder ion column (Gallium ion source). The resulting structure consisted of a square array of circular holes cut through to the silicon substrate of the sample. There were two FIB runs executed on two different, but similar multilayers – one made of Ag-Ge-Ag (6-240-160 nm) and the other made of Ge-Ag-Ge-Ag (4-12-270-200 nm). The Ge-Ag-Ge-Ag multilayer structure is designed to selectively emit at $3.39 \mu\text{m}$ in a similar manner to that of Sample 1 from Chapter V. The additional layer of Ge was added to provide an environmental barrier for the top Ag layer based on the previous experiments documented in Chapter V. This thin 4-nm Ge capping layer was employed to mitigate oxidization of the metal and prevent the HIPIMS-deposited Ag from coalescing during

thermal excitation. Both Nova FIB runs were carried out under manual operation by an AFRL MCF operator.

The first Nova FIB run experimented with the precision of positioning holes and ascertaining the requisite FIB power parameters needed to mill through the multilayer down to the Si substrate. SEM micrographs of this test sample taken from surface normal and at a 52° tilt from surface normal are shown in Figure 58 and Figure 59, respectively.

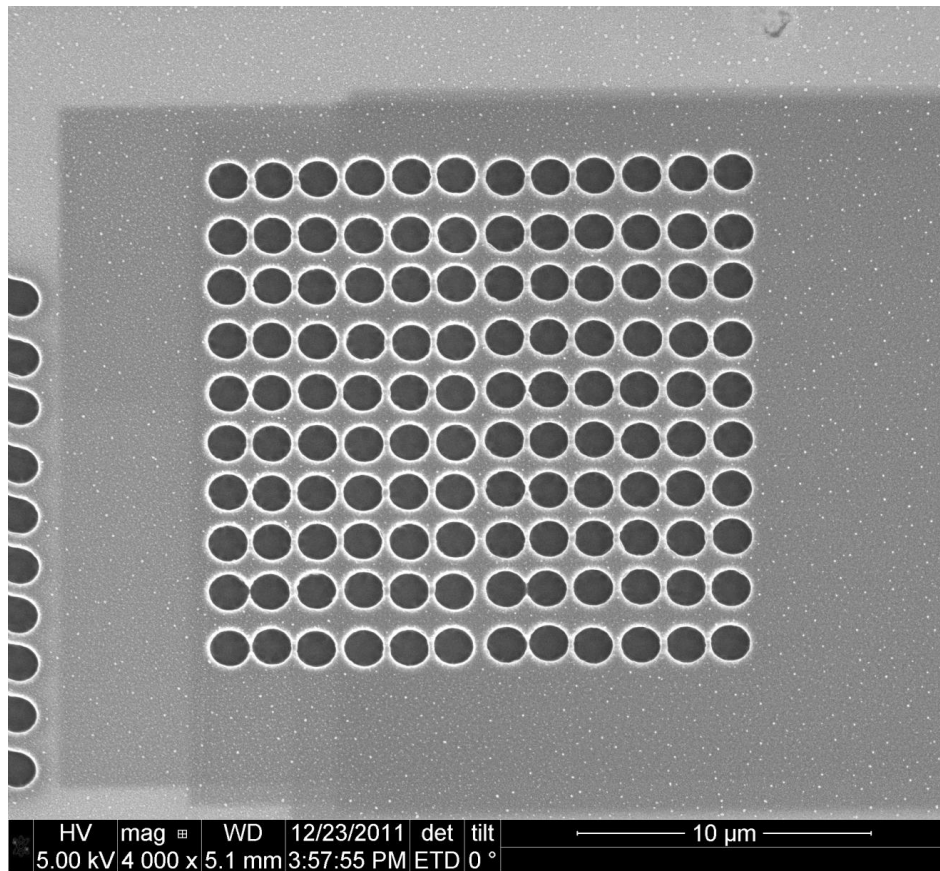


Figure 58. SEM micrograph of a hybrid photonic crystal-multilayer (Ag-Ge-Ag) on a silicon substrate. Ag and Ge layers were deposited via a High Power Impulse Magnetron Sputtering (HIPIMS) technique with dimensions 6-240-160 nm. The hole array was milled into the multilayer using focused ion beam (FIB) milling. Micrograph was taken from surface normal.

Before milling a material with focused ions, the shapes to be patterned must first be generated by constructing a series of traces. The traces can be pulled from a default library, provided by Nova, or custom patterns can be designed. In Figure 58 and 59, traces for the circular holes were individually sized and positioned into a 6×10 array. Then, the traced pattern was milled into the multilayer two times (from left to right).

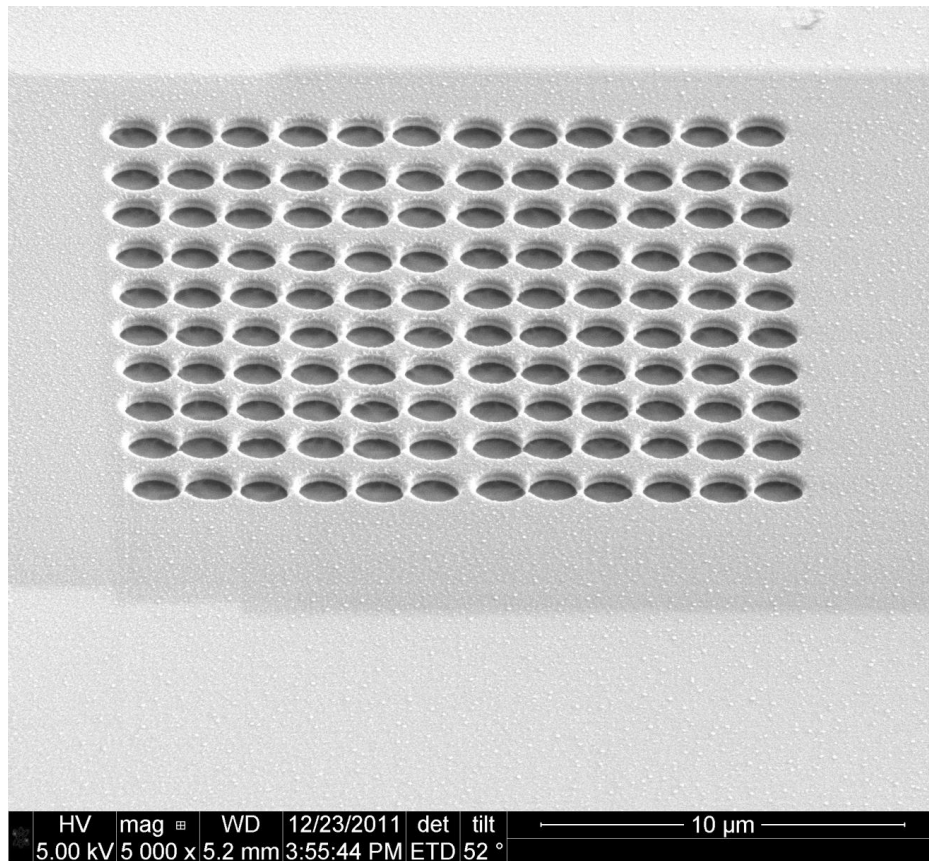


Figure 59. SEM micrograph of a hybrid photonic crystal-multilayer (Ag-Ge-Ag) on a silicon substrate. Ag and Ge layers were deposited via a High Power Impulse Magnetron Sputtering (HIPIMS) technique with dimensions 6-240-160 nm. The hole array was milled into the multilayer using focused ion beam (FIB) milling. Micrograph was taken at an angle of 52° from surface normal.

The rectangular shades of gray surrounding the hole array come from needing to image an effective area on the sample with the FIB so that the next 6×10 array can be

properly aligned and milled next to the first. Similar to an SEM, focused ions can be used to image a sample at high magnifications. The negative side-effect of imaging this way is the minute amount of focused ion energy that is used to image will, to a small degree, ablate some material away in the process.

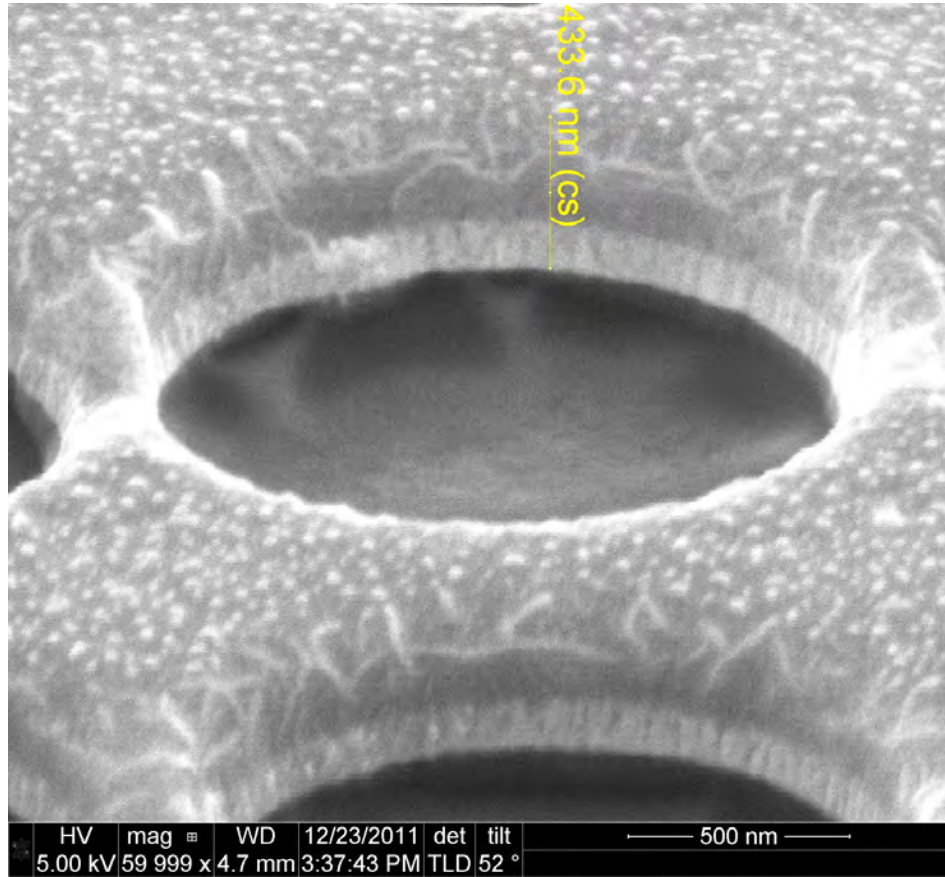


Figure 60. SEM micrograph of a hybrid hole array/multilayer (Ag-Ge-Ag) on a silicon substrate. Ag and Ge layers were deposited via a High Power Impulse Magnetron Sputtering (HIPIMS) technique with dimensions 6-240-160 nm. The hole array was milled into the multilayer using focused ion beam (FIB) milling. Micrograph was taken at an angle of 52° from surface normal.

Figure 60 shows a close-up of a single hole using an SEM. The hole is approximately 1.25 μm in diameter. The ablation that occurs during FIB milling follows

a random raster pattern. Streams of Ag material are visible on the outer edges of the circular aperture due to the residual effects of this raster technique. Also, note that the edges at the top Ag layer are curved slightly.

The objective for the second test run on the Nova FIB Dual Beam was to characterize the feasibility of fabricating a large-scale periodic array. The pattern for this run consisted of a square array of circular holes with 3- μm diameters and 6- μm periods as shown in Figure 61.

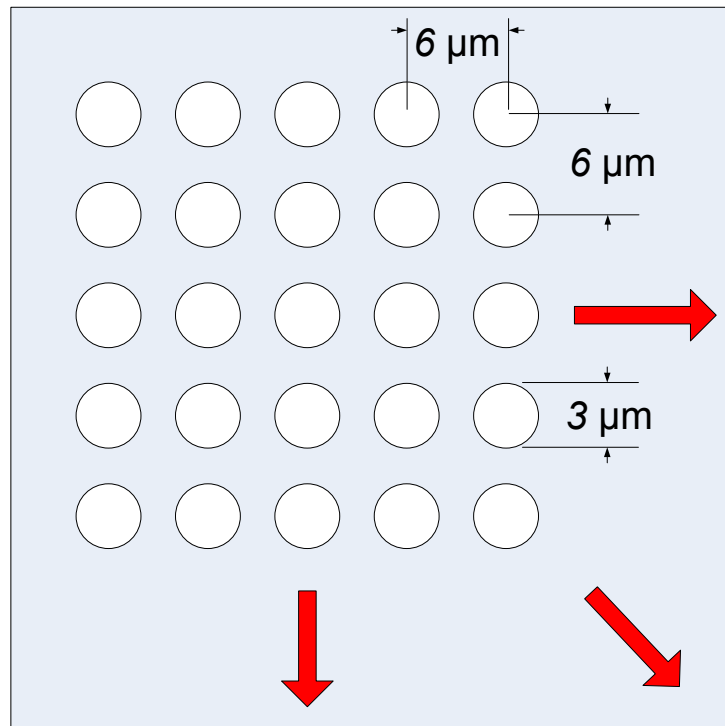


Figure 61. Illustration of a photonic crystal-multilayer hybrid structure constructed of a square array of circular holes embedded inside of a multilayer with 3- μm diameters and 6- μm periods View is from surface normal of the structure.

The Ge-Ag-Ge-Ag (4-12-270-200 nm) multilayer this square hole array was patterned into was deposited via the HIPIMS technique. Figure 62 shows a picture taken with a digital camera of the PC-multilayer structure embedded immediately to the right of

a black ink dot. Total array size is $1.61 \text{ mm} \times 113.33 \text{ }\mu\text{m}$. The black ink dot was used as a marker to pinpoint the center of the multilayer substrate. Longest dimension of the multilayer substrate is 2 inches.

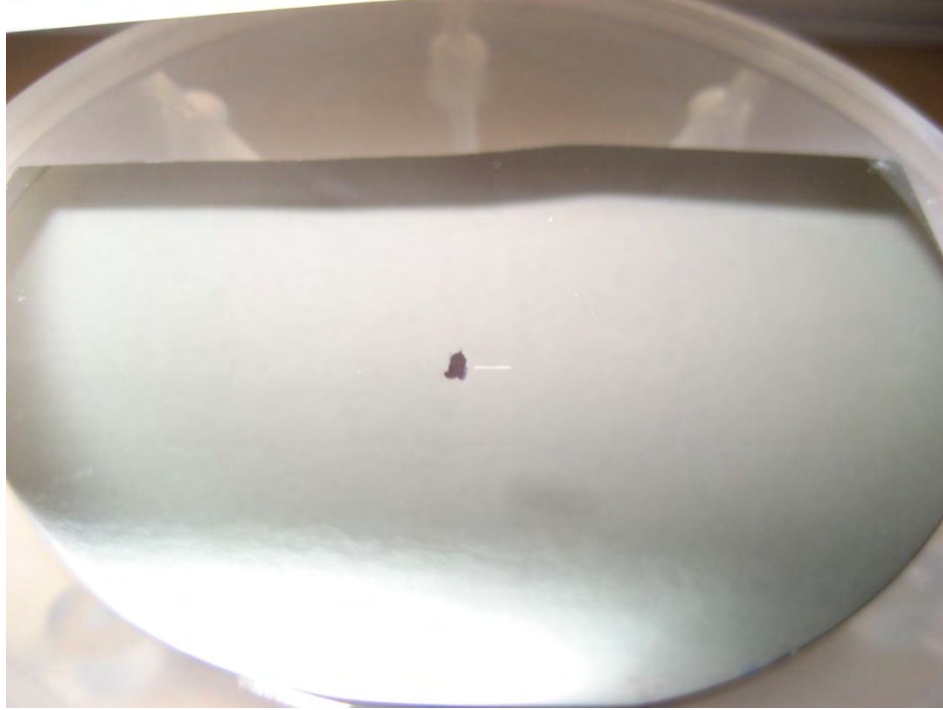


Figure 62. Picture taken with a digital camera of a hybrid photonic crystal-multilayer structure embedded immediately to the right of a black ink dot. Total array size is $1.61 \text{ mm} \times 113.33 \text{ }\mu\text{m}$. The Ge-Ag-Ge-Ag (4-12-270-200 nm) multilayer was deposited on a Si substrate. The square array of circular holes was milled into the multilayer using a focused ion beam (FIB) system.

The square pattern was processed through serial exposures of smaller array cells, 12×12 array of holes, from left to right over a 1.61-mm distance. Two rows were completed from top to bottom to achieve a $113.33\text{-}\mu\text{m}$ width. Nova FIB conditions included a 9.3 nanoamps (nA) beam resulting in 99-115 second patterning times per array cell. Using the 9.3 nA setting is typically higher than desired for precision milling. However, in an effort to mill each array cell more quickly, this amperage setting was

chosen. Figure 63 shows an SEM micrograph of the fabricated PC-multilayer from surface normal at 50× magnification. The black ink dot is especially visible to the left of the fabricated PC-multilayer in this image.

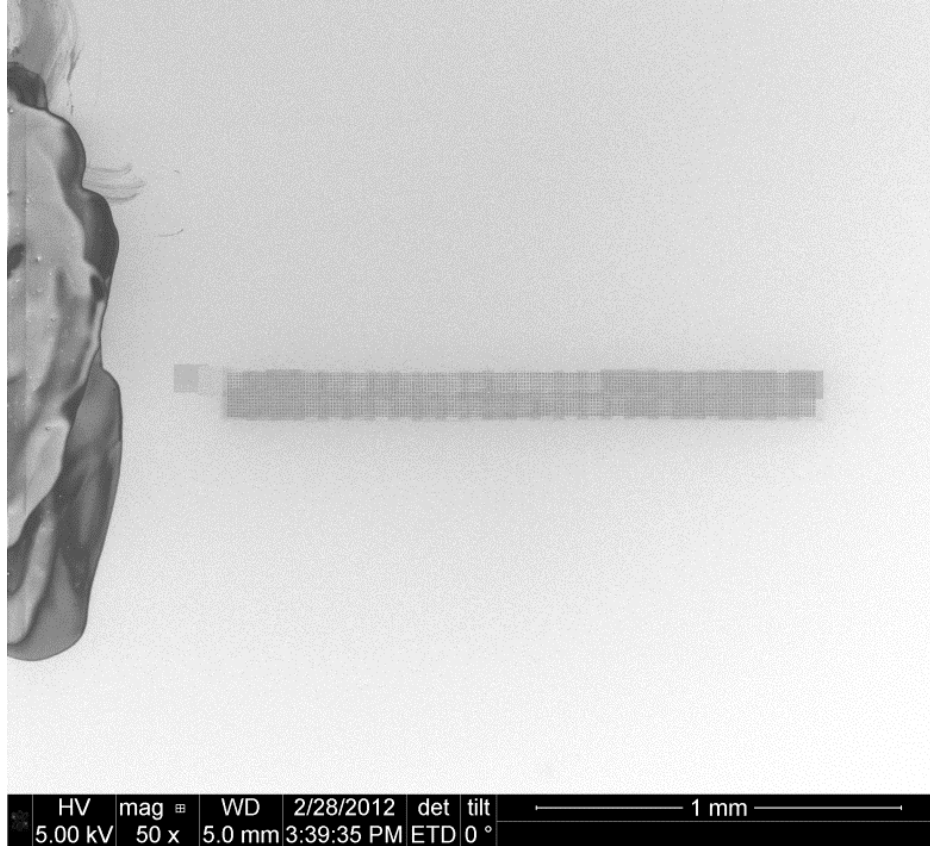


Figure 63. SEM micrograph at 50× magnification of a hybrid photonic crystal-multilayer structure embedded immediately to the right of a black ink dot. Total array size is 1.61 mm × 113.33 μm. The Ge-Ag-Ge-Ag (4-12-270-200 nm) multilayer was deposited on a Si substrate. The square array of circular holes was milled into the multilayer using a focused ion beam (FIB) system.

At higher magnifications, surface materials in varying quantities have been ablated away during manual alignment of adjacent array cells. This is shown in Figure 64 where an SEM micrograph from surface normal of the center of the fabricated PC-multilayer was taken at 750× magnification. Upon visual inspection, the periodic array

of holes is slightly askew, but this was expected given the manual alignment of the hole array.

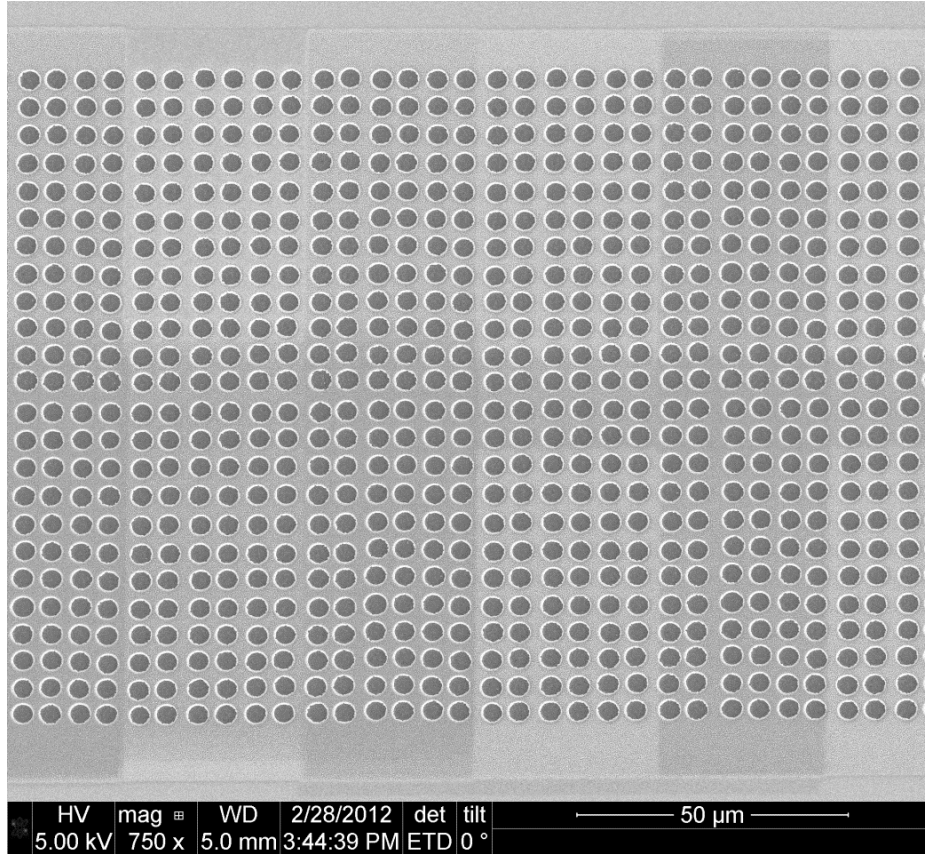


Figure 64. SEM micrograph of the center of a hybrid photonic crystal-multilayer structure at $750\times$ magnification. The Ge-Ag-Ge-Ag (4-12-270-200 nm) multilayer was deposited on a Si substrate. The square array of circular holes was milled into the multilayer using a focused ion beam (FIB) system.

An SEM micrograph from surface normal of the center of the fabricated PC-multilayer taken at $5000\times$ magnification is shown in Figure 65. At this magnification, it is evident that the thin Ge and Ag top layers have undergone mild ablation while the FIB was used to align each array. The diameters of each circular hole ranged from 3.40-3.78 μm . On average, each hole was 0.6 μm over the target hole diameter of 3 μm . The

period between each hole was not exact given the manual alignment resulting in a range of periods from 4-6 μm . Moreover, due to the increased amperage (9.2 nA) used for this test run, the edges around the circular holes were not uniform.

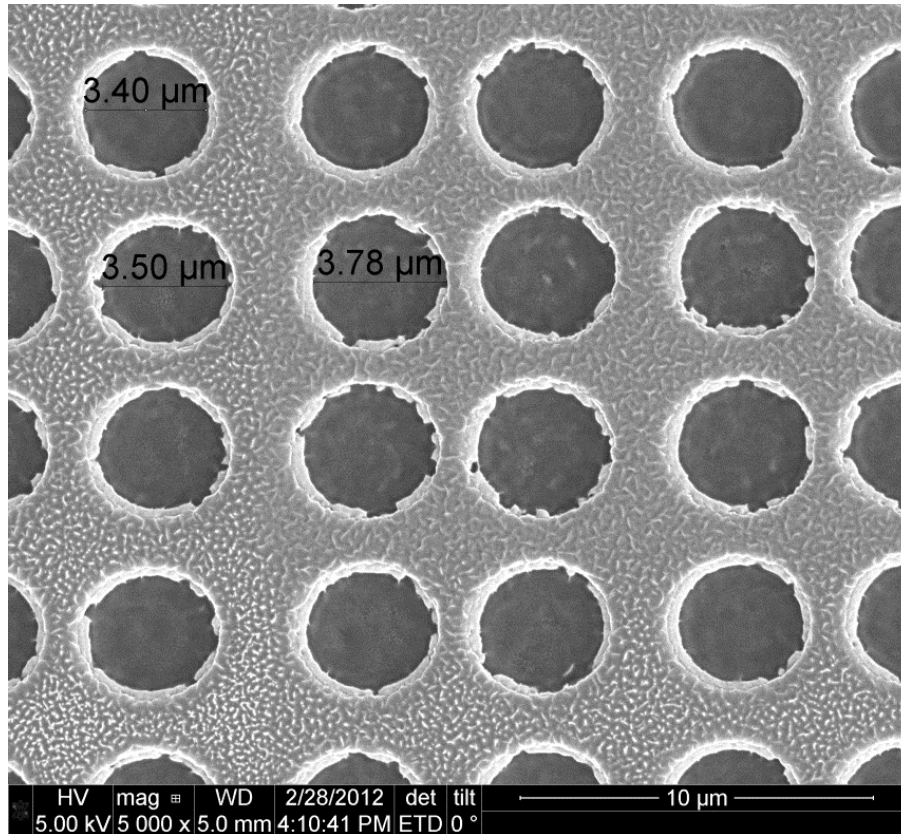


Figure 65. SEM micrograph of the center of a hybrid photonic crystal-multilayer structure at $5000\times$ magnification. The Ge-Ag-Ge-Ag (4-12-270-200 nm) multilayer was deposited on a Si substrate. The square array of circular holes was milled into the multilayer using a focused ion beam system.

The FIB-milled PC-multilayer required a total of 8 man-hours on a FIB system to achieve an array size of $1.61\text{ mm} \times 113.33\text{ }\mu\text{m}$. While this is not practical for commercial applications where larger surface areas would be desired, FIB-milling under manual operation is still useful to converge upon suitable FIB milling settings appropriate

for a sample with a particular composition, and lays the framework for future large-scale patterning efforts with micro- and nano-scale features sizes.

Summary

This chapter discussed the design and initial fabrication results of a Hybrid PC-multilayer. Using CST, this sub-wavelength hole array structure was modeled to examine the angular and polarization sensitivities of a 3-D thermal emitter design. Initial fabrication results from a FIB milling technique on a HIPIMS-deposited multilayer were presented as well. Conclusions and recommendations for future work that will complement the research presented in this thesis are captured in the following chapter.

VII. Conclusion

In this thesis, two thermal emitter designs were proposed using RCWA numerical calculations and CST modeling. Temperature-dependent optical constants of the constituent materials Ag and Ge were calculated and used to predict the performance of the thermal emitters at temperatures at and above room temperature. The truncated resonator design used a HIPIMS deposition technique to deposit nano-layers of Ge and Ag to build a tri-layer structure. Angular sensitivities to incident IR radiation at room temperature were investigated. Spectroscopic ellipsometry was used to derive the actual optical constants of the HIPIMS-deposited materials and then compared to bulk material values from literature and to re-simulate device performance. Emittance was derived from radiance measurements taken from 3-13 μm while the truncated resonator was thermally heated to various temperatures up to 601 K. At normal incidence, a comparison of inferred emittance from reflectance measurements and those derived during thermal excitation was also presented. CST simulation and modeling were used to design a more complex 3-D thermal emitter design, the PC-multilayer. For this hybrid structure, FIB milling was used to pattern a hole array into a HIPIMS-deposited multilayer. Though simulation, angular sensitivities to incident IR radiation at room temperature were also investigated.

The original intent of this research was to investigate how a surface could be engineered to coherently affect the thermal radiative properties of a surface, both spectrally and directionally, through the use of micro- and nano-structured materials. However, as the research effort progressed, it became apparent that practical design and fabrication of engineered structures is not as clear-cut as the designer may expect it to be.

Beginning with the design phase, the material properties found in Palik's *Handbook of Optical Constants of Solids* [44] were used to initially describe the predicted behavior of the truncated resonator. Palik's optical constants are most widely used in published works but, as shown in Chapter V, there were significant differences between the simulation using Palik's values and the experimental results. While the intrinsic bulk values from Palik yielded results that identified the proper spectral location of resonances, the overall behavior of the actual resonances, like considerable broadening, was not predicted. From another perspective, this broadening could be embraced to achieve broadband spectral responses in a given application where more bandwidth is desired. Further, an absorption peak at 12 μm in the HIPIMS-deposited Ge layer was not accounted for in the Palik data but was captured in the effective optical constants derived from the IR-VASE ellipsometric measurements.

Surface quality, purity, overlayers, and microstructure will all affect the optical properties of deposited materials. The HIPIMS deposition technique was chosen to minimize the effects of an amorphous microstructure and surface roughness. Despite this consideration, it seemed that these effects could not be entirely avoided. Evaporated metal films in particular are known to have a significant volume fraction of voids [44]. Using the IR-VASE, optical constants were derived ellipsometrically for the HIPIMS-deposited Ag and Ge. Feeding these derived optical constants back into the simulation allowed the expected emittance to come much closer to the measured results. Ultimately, to accurately predict the performance of a thermal emitter, the optical properties of the actual materials utilized in the design must be determined.

The assessments described thus far were all done at room temperature and the emittance calculations were all made by invoking Kirchhoff's law where emittance was indirectly obtained from reflectance measurements. When the truncated resonator was thermally heated, a direct method was used to calculate emittance from radiance measurements taken with a spectrometer. When comparing calculated emittance under thermal excitation with that obtained using room-temperature reflectance measurements, while inferring emittance can help to approximate the expected emission from a structure, it is not an exact method of determining the actual emittance of a thermal source. It was apparent that inferred emittance using Kirchhoff's law would not only vary in magnitude when compared to direct emittance calculations, but also neglected to capture some physical phenomena.

The truncated resonator thermal emitter design offered spectral coherence, confined to a design wavelength of choice, with near-isotropic emission in the IR regime. The spectral emittance exhibited by this structure was unaffected by the angle of incident radiation. To achieve spatial coherence, a 3-D structure was presented, the PC-multilayer. Using holes with a diameter that was half the design wavelength, the PC-multilayer design acted as a spectrally and spatially selective transmission filter, owing to a rich interplay of plasmonic effects and waveguide modes. While FIB milling a single sample one at a time is not practical for industry, manual operation of a FIB system can still be utilized in academia to study specific phenomena or fabricate master moulds to be used repeatedly in a template-based nanofabrication process. In addition, acquiring proper FIB milling settings specific to a given structure and composition is paramount in achieving high-precision fabrication results. FIB milling large-scale samples becomes

feasible with the use of pattern generators that automate the arraying unit cells are utilized. Newer FIB systems have this capability and should be considered for future periodic designs.

Future Work

There are several areas with respect to this research topic that are recommended below for further investigation. Recommendations for future work to follow have been divided into three sections – design, fabrication, and characterization.

Design

For structures that are expected to operate and perform well in environments above room temperature, it is recommended that the actual optical constants of each constituent material are determined at the expected operating temperatures first. This can be accomplished by using the IR-VASE with an optional heated sample stage attachment called the Heat Cell (HTC-100) or the Cryostat. The Heat Cell can reach temperatures up to 573 K and allow ellipsometric measurements to be taken at fixed temperature increments. The Cryostat's temperature range is from 4.2-700 K and allows temperature-dependent optical constants to be obtained above and below room temperature. Finding the actual material properties of real materials up front will make the analytical designs more accurate when compared to experimental results.

Hierarchical structures and structures with tapered geometrical profiles could be explored next. The analytical development for these structures could be easily implemented in 3-D using advanced modeling and simulation programs. Further, the CST software suite includes an electromagnetic-thermal coupled simulation that enables

an additional thermal analysis of structures to include temperature-dependent material parameters and the effect of thermal expansion on scattering. CST is also compatible with dedicated graphics processing unit (GPU) computing and it is highly recommended that any CST analysis be carried out in conjunction with a dedicated GPU to shorten simulation wait-times. COMSOL is another multiphysics program that is more capable if a rigorous thermal analysis is desired. However, using highly dispersive material properties in CST's frequency domain solver is not practical for broadband examinations given the long simulation times. Thus, use of the CST time domain solver is computationally more efficient, but unable to evaluate off-normal illuminations. Hence, for highly dispersive designs, an FDTD electromagnetic solver such as Lumerical may be more efficient than CST for off-normal incident angles in the time domain. For all these modeling suites, it is recommended that a high performance supercomputer site be utilized to decrease simulation times.

Fabrication

A template-based approach is a simple, repeatable, and low-cost nanofabrication technique capable of producing robust, large-scale samples and is recommended for future fabrication of thermal emitters. Using a double-inverse method, master templates can be created one time and used to repeatedly manifest sacrificial moulds of the master pattern. The double-inverse term is used to highlight the fact that the final product will not be an inverse of the master template, but an exact copy. This technique also offers fabrication of robust samples, capable of being handled constantly, without the necessity of a standard substrate. An illustration of this recyclable nanofabrication process is shown in Figure 66. Certainly, other nanofabrication techniques and tools could have

been utilized or may become available beyond those mentioned here. The intent of this section is not to complete a review of all fabrication avenues, but rather to discuss a few fabrication techniques, tools, and facilities readily available at the time of this research.

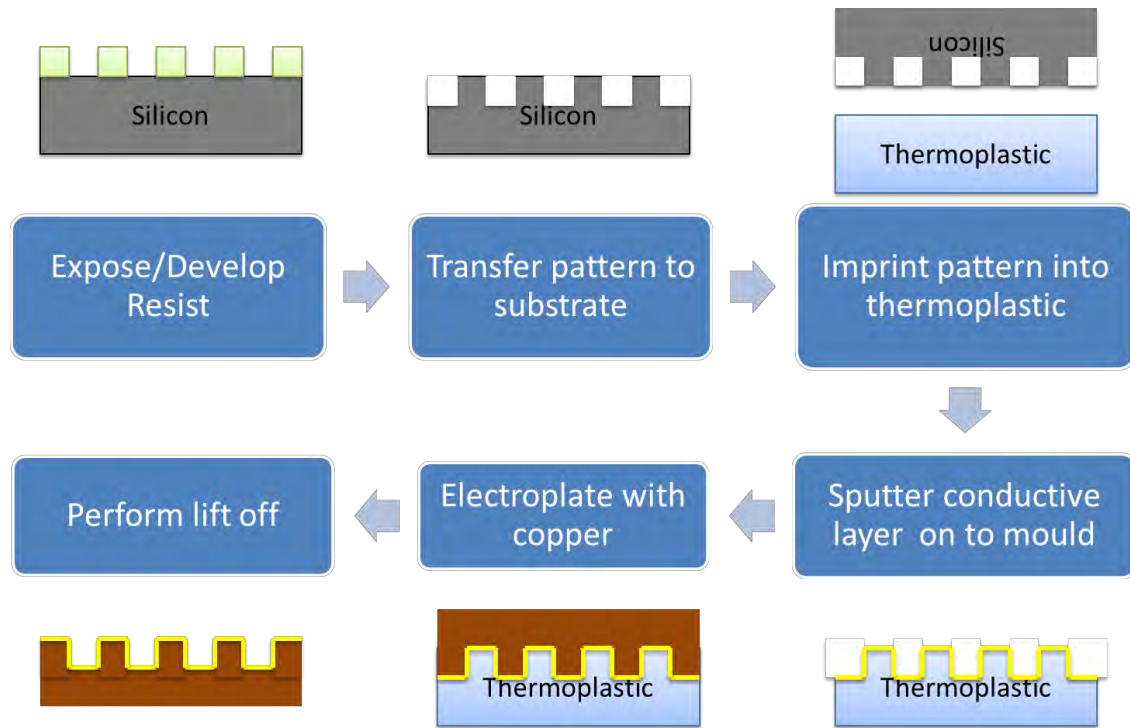


Figure 66. Illustration of a template-based nanofabrication approach that is capable of producing robust, large-scale samples with simple, repeatable, and low-cost execution.

Beginning with photolithography, a pattern is created in photoresist on a substrate. This can be accomplished through the Nanoscribe 3D laser lithography tool (AFRL), interference lithography (AFIT), or exposure through a master mask on a mask-aligner (AFIT). With the exception of using an outside vendor, use of the Heidelberg Mask Maker in the AFIT Clean Room is the most practical way-forward in fabrication of a master template. The Heidelberg is a tabletop laser pattern generator capable of creating master masks with feature sizes down to 1 μm . The master mask is loaded into a

mask aligner where the designed pattern is exposed onto photoresist. The Heidelberg is also capable of grayscale lithography where the laser power can be scaled to adjust the depth of the exposure allowing 3-D images to be fabricated in photoresist, to include tapered profiles and designs with multiple periods. Use of a master mask enables a recyclable process where the master mask can be used repeatedly to expose multiple samples.

After the photoresist is developed, a series of post-processing techniques (*e.g.* chemical etching, reactive ion etching (RIE)) can be used to transfer the designed pattern to the substrate, or another medium, creating a master template. Chemical etching typically involves wet chemicals in various concentrations to selectively etch a given material. The chemical recipe used will depend on the material to be etched. RIE is an anisotropic etching process that selectively etches a given material based on a chemical recipe put together by the user. The chemical recipe will again depend on the material. RIE etch rates run from 200 nm to 1 μm per minute but are usually limited to a total of 10 μm . Deep RIE (DRIE) is a similar process that is capable of higher etch rates up around 20 μm per minute. The total limit on etch depth using DRIE has been demonstrated in excess of 600 μm . RIE equipment is available in the AFIT Class 1000 Cleanroom and in the AFRL/RV Cleanroom. An alternative method to transferring a pattern to a substrate without the need of photoresist is through FIB milling. With FIB milling, custom master templates can be directly patterned. FIB milling tools are available by appointment at AFRL's MCF. AFRL will be installing two new TESCAN FIB systems in 2012 that will enhance the MCF's micro- and nano-patterning capabilities.

With a master template in hand, the pattern would be imprinted into a slave medium such as a thermoplastic, like poly(methyl methacrylate) or PMMA for short. Thermoset/photoresists such as SU-8 could also be used to manifest master templates. This is accomplished via nanoimprinting where a master template acts as a mould to transfer a pattern to a slave template, usually through the use of heat and a vacuum environment. Nanoimprinting is also commonly known as hot embossing when heat is involved. PMMA is an ideal choice since it is inexpensive and more robust than Si. Nanoimprinting can be carried out through commercial tools or other experimental techniques [26, 65, 66]. AFRL/RYS Cleanroom houses a Nanonex NIL system.

Next, the slave template will need a conductive layer (metal or conductive ink) deposited onto it. This is necessary for subsequent electrodeposition. Electrodeposition, also known as electroplating, is a deposition technique that involves metal ions traveling from an anode to a cathode through an electrolyte bath. In this case, the object to be plated is the cathode. Hence, conductivity is needed for deposition to occur. From initial Cu electrodeposition results carried out in the AFIT Clean Room, it is recommended that the thickness of the conductive layer be at least equal to its skin depth. Using sputtered Au, a thickness of 30 nm was ideal for a uniform Cu layer to be electrodeposited. Electrodeposition will be used to “fill in” the slave template with bulk Cu until a sizeable amount of Cu ions has accumulated, resulting in a Cu sample that is more robust and could be handled repeatedly with little complication.

Lastly, a lift-off technique will be required to separate the original PMMA slave template from the Cu structure, thus completing the double-inverse templating process. PMMA is known to have poor adhesion with many metals, so manual lift-off of the slave

template may be possible. Alternatively, since PMMA is a thermoplastic, it can be reheated to make the slave template less rigid and permit lift-off in case manual methods are not feasible. A release layer could also be utilized to aid in lift-off in case the above methods fail.

This template-based process offers a recyclable and low-cost nanofabrication technique capable of producing robust, large-scale optical structures. Initial fabrication results of arrayed nanostructures using a 3-D laser lithography tool made by Nanoscribe can be found in Appendix A.

Characterization

A unique capability at Air Force Institute of Technology (AFIT) in the area of optical observables is the ability to record IR-tunable diffuse ellipsometry measurements. AFIT's Schmitt Measurement Services (SMS) Complete Angle Scatter Instrument (CASI) was upgraded to be fully polarimetric and fit with six tunable external-cavity quantum cascade lasers ranging in wavelength from 4.4-9.7 μm . Original CASI laser wavelength of 3.39 and 10.6 μm are also available. The CASI can be configured with both indium antimonide (InSb) and mercury cadmium telluride (HgCdTe) photovoltaic detectors, allowing detection of scattered radiation between 2-12 μm . AFIT's CASI is capable of measuring both reflected and transmitted scatter from a sample surface. The bidirectional scatter distribution function (BSDF) is developed as a model describing this scatter. BSDF is equal to the sum of the bi-directional reflectance distribution function (BRDF) and bi-directional transmittance function (BTDF). Polarimetric scatterometry is a form of optical scatterometry that accounts not only for angle-of-incidence sensitivities, but also the phase of both incident and scattered radiation as a method to further

characterize the scatter from a surface. To further characterize the scatter of the PC-multilayer structure, BSDF and polarimetric scatterometry measurements are recommended to describe how the IR radiative properties of the sample are affected by the angle and polarization of incident laser radiation.

Appendix A. Nanofabrication

3-D Laser Lithography: Initial Fabrication Results

AFRL/RX recently acquired a Nanoscribe 3-D laser lithography tool in 2011. In an effort to characterize the feasibility of using this equipment to fabricate large-scale nanostructured samples, a test run was carried out with the purpose of fabricating a 2×2 array. Processing times and uniform patterning between each unit cell were evaluated during this effort.

The Nanoscribe can import .stl file extensions for 3-D geometries. CST was used to construct the 3-D unit cell and export the geometry in the .stl file format. Figure 67 shows a drawing of one unit cell generated using CST.

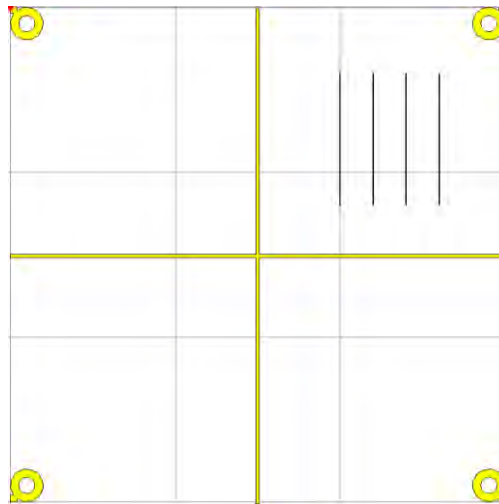


Figure 67. Image of planar 3-D unit cell constructed in CST.

The Nanoscribe has two physical stages, one is mechanical and the other is piezo, that allow it to transverse over three dimensions. The mechanical stage can only move laterally in two dimensions but allows wide surface areas to be transversed. The piezo

stage is capable of moving within a $300 \times 300 \times 300 \mu\text{m}^3$ cube which allows the nanoscribe to expose photoresist within a 3-D space. This makes 3-D structures with spatially varying geometry in all three dimensions possible. The planar unit cell shown in Figure 67 was conceptualized to determine the stability of the piezo stage for the full 300 μm in length and width. Furthermore, this simple geometry would allow one to observe alignment of adjacent unit cells when arrayed. A programming script was written to serially expose the 2×2 array in Nanoscribe photoresist (IP-L). Glass substrates provided with the nanoscribe were used for this test sample. In Figure 68, the final arrayed pattern (simulated in CST) is shown next to same pattern with Zygo images overlaid in front of the respective areas where the pictures were taken on the fabricated sample.

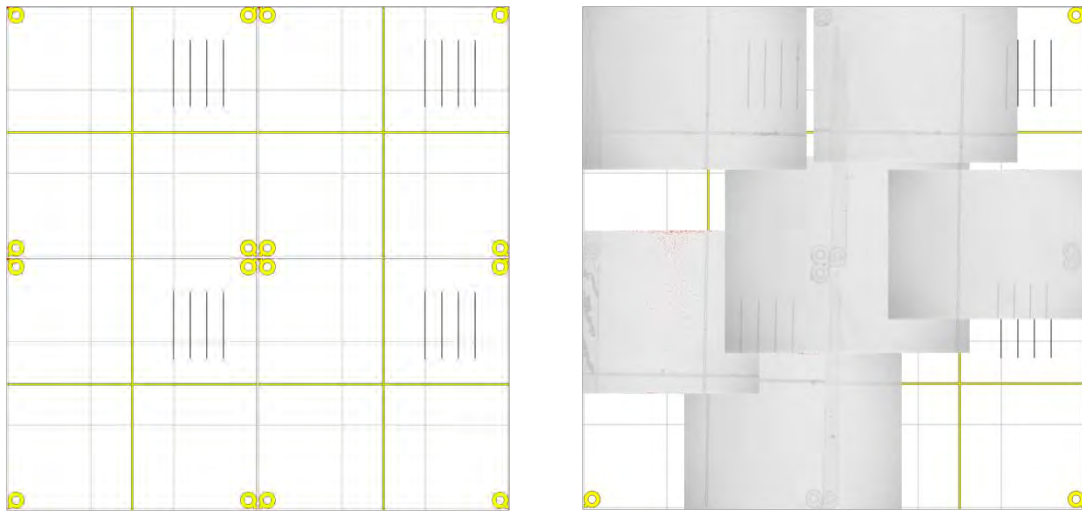


Figure 68. The final arrayed pattern (simulated in CST) shown next to same pattern with Zygo images overlaid in front of the respective areas where the pictures were taken.

Overall, the piezo stage did well for most of its dynamic range but it was observed to be unstable from 275-300 μm . Furthermore, there were alignment issues that were most evident at the corners of the unit cells where overlapping and misalignment was

encountered. There were also several areas where the IP-L photoresist was over-exposed, or burned, due to possibly too much laser power. Figure 69 shows these observations highlighted in red for each respective Zygo image.

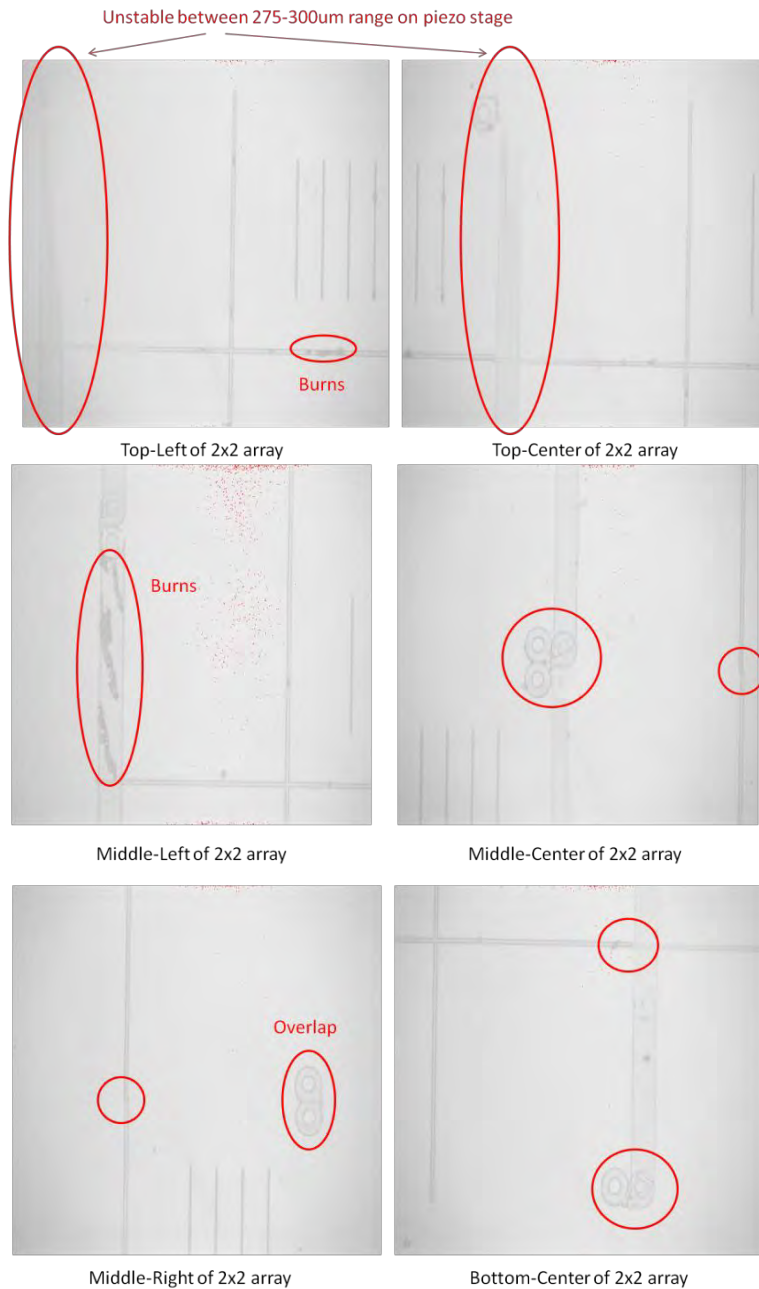


Figure 69. Zygo images of fabricated 2 × 2 array using a Nanoscribe 3-D laser lithography tool. Patterned array was exposed in Nanoscribe IP-L photoresist on a glass substrate.

The next run on the Nanoscribe aimed to fabricate a 10 mm × 10 mm area of 1- μm tall pillars ($200 \times 200 \text{ nm}^2$), periodically arranged in two dimensions with 6- μm periods between each pillar. This run, however, was never executed after first calculating the time it would take to write one array cell ($275 \times 275 \mu\text{m}$) of these same pillars. The estimated time for this size array was 35 minutes. Assuming ideal fabrication conditions, to fabricate a 10 mm × 10 mm pillar array would require 32 days of continuous laser operation. This fabrication time pertains to use of an oil-immersion objective on the Nanoscribe (the only operating objective available at the time). An air objective is available to be used on the Nanoscribe and this allows a larger photoresist volume to be exposed during laser operation at the cost of larger feature sizes. This would help to shorten laser operation time. A shallower design, less than the proposed 1- μm height, would also quicken the exposure time. In summary, use of the Nanoscribe 3-D laser lithography tool for large surface area patterning is not recommended given the impractical processing times.

Other Nanotechnology Characterization Techniques

Thermophysical properties, such as thermal conductivity and specific heat, could be also measured using steady-state, modulated, or pulsed heating techniques. Other optical techniques used in measurement of thermal properties of micro- and nano-structured materials include thermorefectance, Raman spectroscopy, photothermal radiometry, fluorescence, laser flash techniques, and scanning thermal microscopy [33]. For *in-situ* morphological sample changes, a 1500°C heating stage can be utilized with a FIB to characterize how the physical structure changes in real-time with increased temperature.

Using an atomic force microscope (AFM) with a heated probe attachment will enable a near-field microscopy capability. Some ellipsometric tools, such as J. A. Woollam's M-2000, allow *in-situ* ellipsometric measurements to be taken so that real-time changes in optical constants can be observed.

Nanofabrication Literature

- Past Achievements and Future Challenges in 3D Photonic Metamaterials (2011) [26]
- Fabrication of nanostructures with laser interference lithography (2008) [67]
- Large-area flexible 3D optical negative index metamaterial formed by nanotransfer printing (2011) [68]
- Unconventional Nanofabrication (2004) [66]
- Structural Transformation by Electrodeposition on Patterned Substrates (STEPS): A New Versatile Nanofabrication Method (2011) [69]
- Fabrication of Hierarchical Pillar Arrays from Thermoplastic and Photosensitive SU-8 (2010) [70]
- PMMA as a Base Material for SU8 Mold to Fabricate PDMS Relief (2010) [71]
- Removal of SU-8 photoresist for thick film applications (2002) [72]
- Hot embossing on polymethyl methacrylate (2007) [73]
- Comparative study of hot embossed micro structures fabricated by laboratory and commercial environments (1998) [65]
- Dual Beam Milling and Deposition of Complex Structures Using Bitmap Files and Digital Patterning (2004) [74]

Appendix B. Supplemental IR-VASE Measurements and Modeling

Spectroscopic ellipsometric measurements were made over a range of optical wavelengths using the Visible VASE (V-VASE) and IR-VASE on a bare Si substrate. Using the Woollam VASE32 software and IR material library, models were fit to the ellipsometric measurements to extract the optical constants of each material (Si and SiO₂ in this case).

The transmittance baseline of the optical path was captured using the IR-VASE and is shown in Figure 70. Atmospheric absorption bands can be observed affecting the spectral profile of the transmittance due to various molecules such as CO₂ and H₂O.

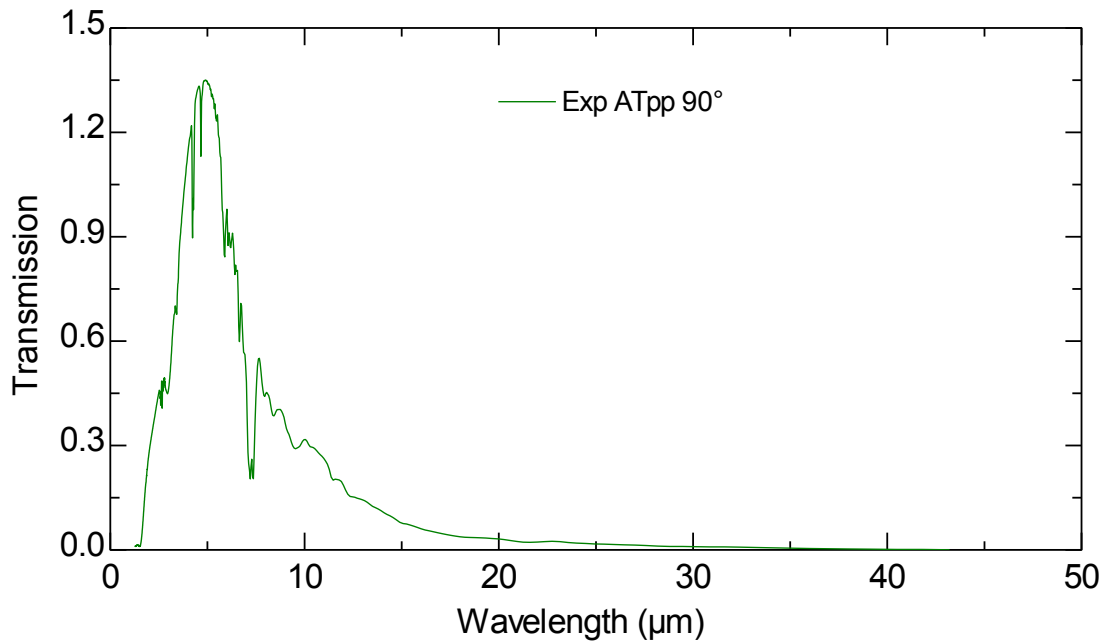


Figure 70. Transmittance baseline of the ambient environment captured by the J. A. Woollam Infrared Variable Angle Spectroscopic Ellipsometer (IR-VASE)

Spectral transmittance of a p-type Si wafer measured using the IR-VASE is shown in Figure 71. From 1.7-5 μm, a negligible amount of light was observed to be

transmitted through the Si wafer. From 5-40 μm , the transmittance monotonically increases from approximately 0 to 0.55. The large absorption observed near 16 μm is attributed to a Fano resonance. This p-type Si wafer was single-side polished. These ellipsometric measurements were taken with laser radiation incident upon the polished surface of the Si wafer. At shorter wavelengths, the rough unpolished surface is observed to scatter light away from the detector aperture. Eventually, as the wavelengths become much longer than the surface roughness features, the surface roughness is no longer resolved and the incident radiation begins to transmit through the Si substrate.

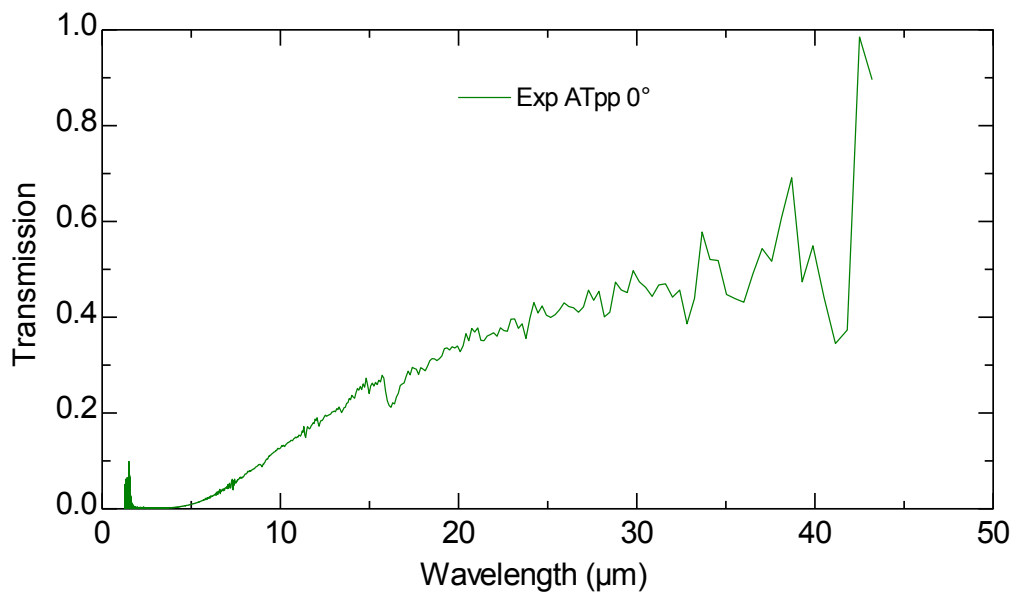


Figure 71. Spectral transmittance of a p-type silicon (Si) wafer measured using the Air Force Research Laboratory's (AFRL) J. A. Woollam Infrared Variable Angle Spectroscopic Ellipsometer (IR-VASE)

A comparison between the spectral transmittance of the same p-type Si wafer and a fitted model is shown in Figure 72. The model was fit using the default Si material from J. A. Woollam's IR library. The large Fano absorption seen at 16 μm was modeled

properly using Woollam’s software. The diffuse scattering resulting from the unpolished backside of the Si wafer cannot be adequately modeled with the Woollam software.

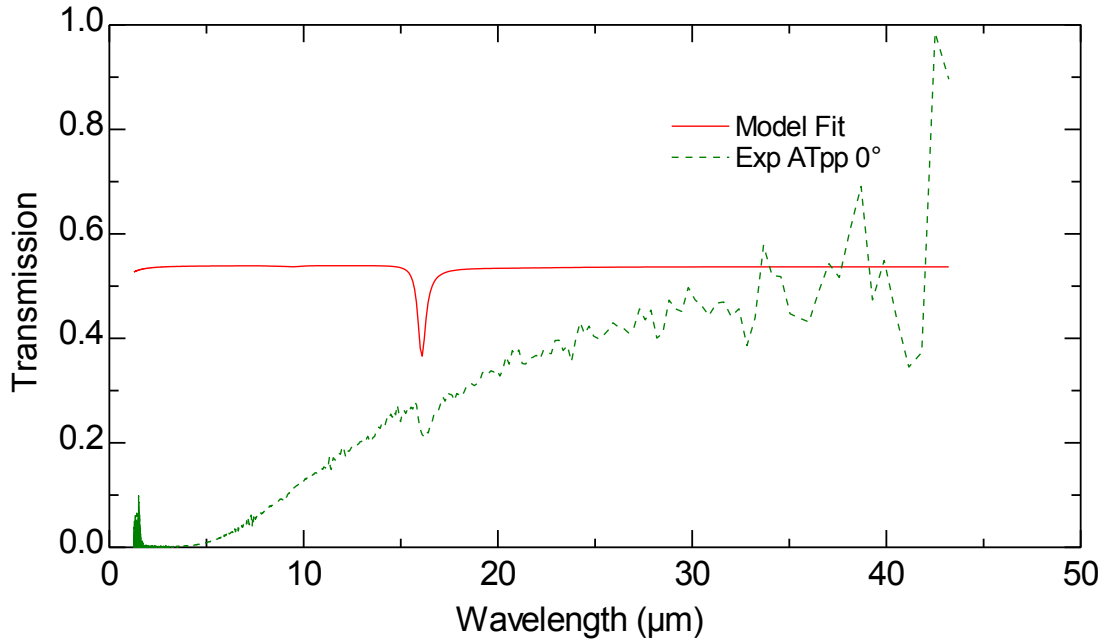


Figure 72. A comparison between a fitted model and spectral transmittance of a p-type silicon (Si) wafer. The model was fit using material constants from J. A. Woollam’s infrared material library. The transmittance was measured using a J. A. Woollam Infrared Variable Angle Spectroscopic Ellipsometer (IR-VASE).

If the Si wafer was double-side polished and the scatter was specular, then a “backside reflection” model could be generated to model interferences between the front and backside reflections at those interfaces. Interface oscillations can be observed when interference between the front and backside reflections occurs. Light from the front and back surfaces will constructively and destructively interfere together in a partially coherent manner. Since this scatter is neither completely coherent, nor incoherent, it is extremely difficult to model. This becomes more and more prevalent at longer

wavelengths when the backside of the wafer effectively appears smoother with respect to wavelength.

Amplitude ratio Ψ and the phase difference Δ ellipsometric measurements made on the V-VASE are shown in Figure 73. The p-doped silicon substrate was measured on the V-VASE initially to verify the thickness of the SiO_2 layer. This is easier on the V-VASE due to the smaller wavelengths used to interrogate the material structures. Thickness of the SiO_2 layer over the silicon wafer was determined to be 2.4 nm at the time of this measurement. Mean square error of the fitted model was 3.35. Materials used from the Woollam visible material library to model the Si substrate and SiO_2 layers were “si” and “sio2”, respectively.

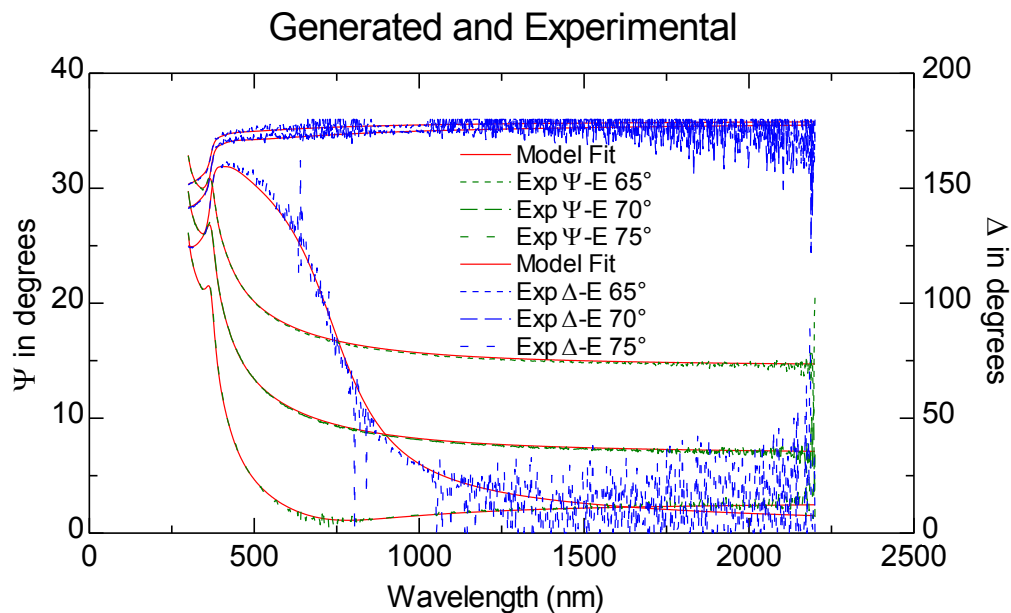


Figure 73. Measured and generated ellipsometry data of a silicon substrate (p-doped) at visible and near-infrared wavelengths. Measured data captured using a J. A. Woollam Visible Variable Angle Spectroscopic Ellipsometer (V-VASE). Fitted model data was generated using J. A. Woollam WVASE23 software.

Using the IR-VASE, amplitude ratio Ψ and the phase difference Δ ellipsometric measurements were made on the same Si wafer and those are shown with their associated model fits in Figure 74 and Figure 75, respectively.

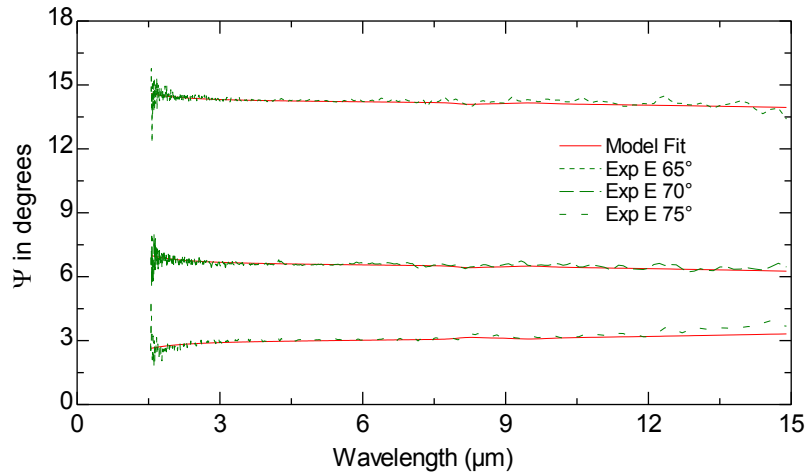


Figure 74. Measured and generated amplitude ratio Ψ data of a silicon substrate (p-doped) at mid-infrared wavelengths. Measured data was captured using a J. A. Woollam Infrared Variable Angle Spectroscopic Ellipsometer (IR-VASE). Fitted model data was generated using J. A. Woollam WVASE23 software.

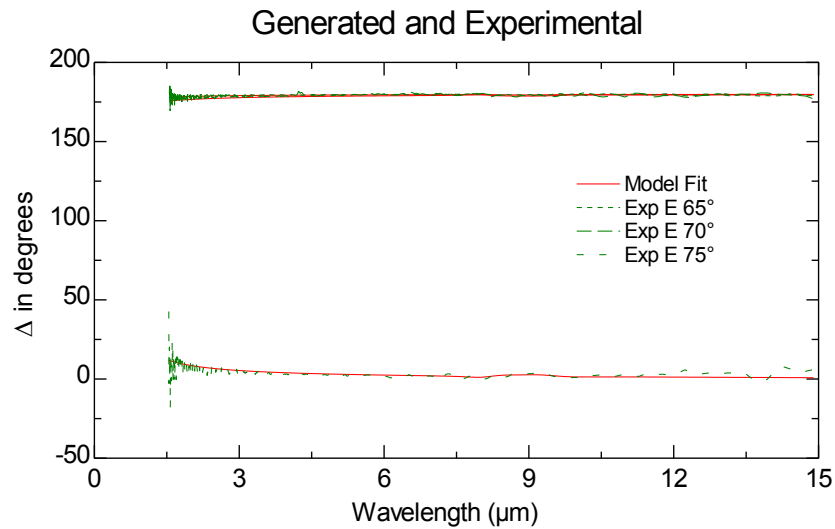


Figure 75. Measured and generated phase difference Δ data of a silicon substrate (p-doped) at mid-infrared wavelengths. Measured data was captured using a J. A. Woollam Infrared Variable Angle Spectroscopic Ellipsometer (IR-VASE). Fitted model data was generated using J. A. Woollam WVASE23 software.

Mean square error of the fitted model on the IR-VASE was 0.51. Materials used from the Woollam IR material library consisted of “sio2_ntve_ir_g” and “si_ir_drude”. Thickness of each layer used in the model was 2.389 nm for SiO₂ and 1 mm for Si. General oscillators and parameters used to model the native silicon oxide layer using the Woollam WVASE32 software are shown in Figure 76.

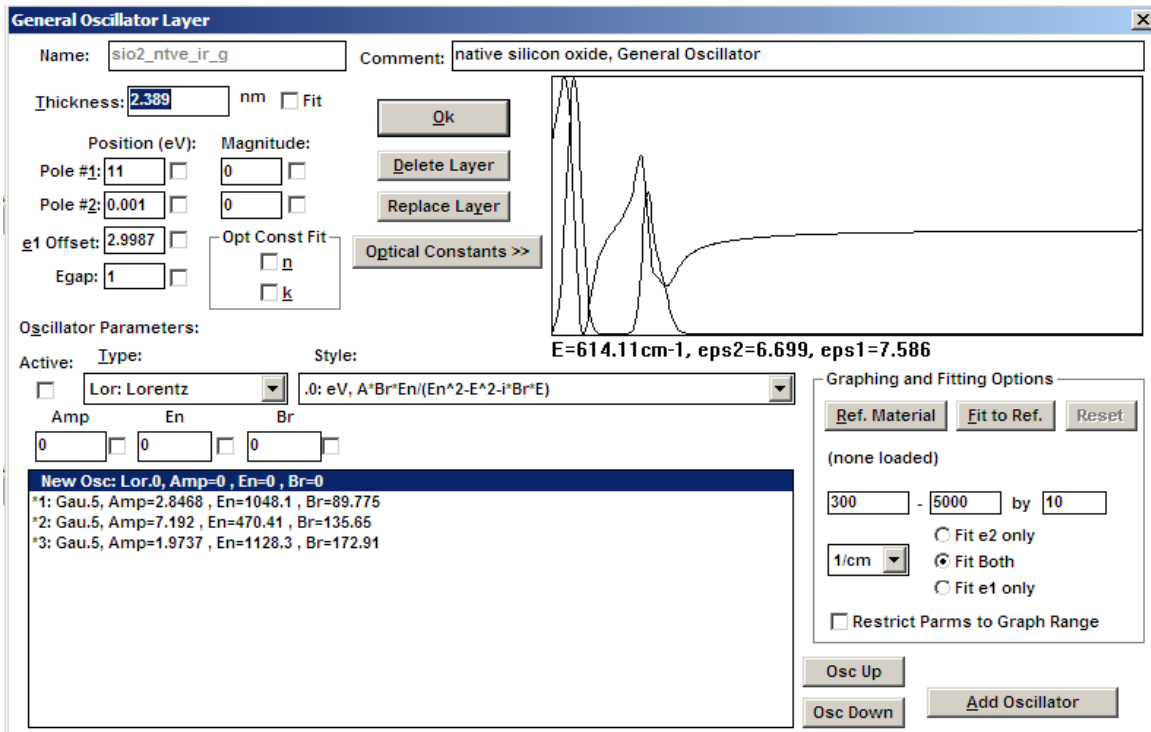


Figure 76. General Oscillator parameters used to model native silicon oxide layer (SiO₂) using Air Force Research Laboratory’s (AFRL) J. A. Woollam Infrared – Variable Angle Spectroscopic Ellipsometer (IR-VASE).

Optical constants for the Si and SiO₂ layers are shown in Figure 77 and Figure 78, respectively. These material properties were derived from the measured ellipsometric data taken by the IR-VASE between 2-15 μm.

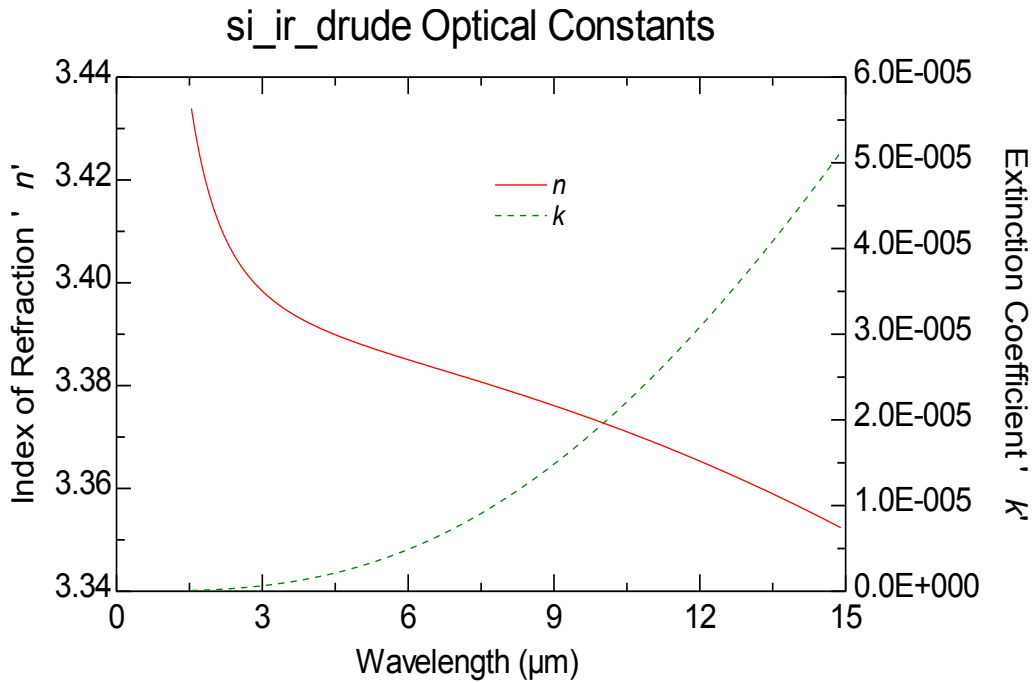


Figure 77. Optical constants for Si wafer derived from measured ellipsometric data between 2-15 μm . Measured data was captured using a J. A. Woollam Infrared Variable Angle Spectroscopic Ellipsometer (IR-VASE).

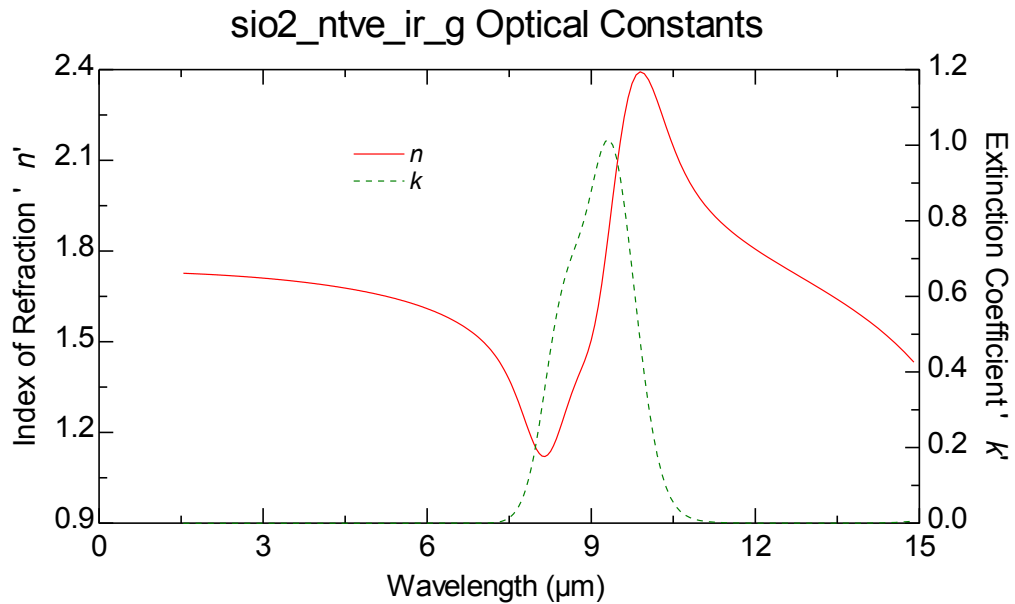


Figure 78. Optical constants for a SiO_2 passivation layer derived from measured ellipsometric data between 2-15 μm . Measured data was captured using a J. A. Woollam Infrared Variable Angle Spectroscopic Ellipsometer (IR-VASE).

Bibliography

- [1] J. R. Howell, Thermal Radiation Heat Transfer, Boca Raton: CRC Press, 2011.
- [2] E. L. Dereniak and G. D. Boreman, Infrared Detectors and Systems, Hoboken: John Wiley & Sons, Inc., 1996.
- [3] J. A. Mason, S. Smith and D. Wasserman, "Strong absorption and selective thermal emission from a midinfrared metamaterial," *Applied Physics Letters*, vol. 98, no. 241105, 2011.
- [4] J.-J. Greffet and C. Henkel, "Coherent thermal radiation," *Contemporary Physics*, vol. 48, no. 4, pp. 183-194, 2007.
- [5] S. Maier, Plasmonics: fundamentals and applications, New York: Springer Science+ Business Media LLC, 2010.
- [6] J. Drevillon, K. Joulain, P. Ben-Abdallah and E. Nefzaoui, "Far field coherent thermal emission from a bilayer structure," *Journal of Applied Physics*, vol. 109, no. 034315, pp. 1-7, 2011.
- [7] S. A. A. Oloomi, A. Saboonchi and A. Sedaghat, "Thermal Radiative Properties of Nanoscale Semiconductors with incoherent Formulation," *Majlesi Journal of Mechanical Engineering*, vol. 3, no. 2, pp. 45-52, 2010.
- [8] B. J. Lee and Z. M. Zhang, "Coherent Thermal Emission From Modified Periodic Multilayer Structures," *Journal of Heat Transfer*, vol. 129, pp. 17-26, 2007.
- [9] B. J. Lee and Z. M. Zhang, "Design and fabrication of planar multilayer structures with coherent thermal emission characteristics," *Journal of Applied Physics*, vol. 100, no. 063529, 2006.
- [10] Y.-T. Chang, Y.-T. H. S.-W. Wu, H.-F. Huang and S.-C. Lee, "Planar Tri-layer Ag/SiO₂/Ag Plasmonic Thermal Emitter with Coherent Thermal Emission," in *Metamorphose-VI*, London, 2009.
- [11] L. P. Wang, B. J. Lee, X. J. Wang and Z. M. Zhang, "Spatial and temporal coherence of thermal radiation in asymmetric Fabry-Perot resonance cavities," *International Journal of Heat and Mass Transfer*, vol. 52, pp. 3024-3031, 2009.

- [12] E. F. Schubert, N. E. J. Hunt, A. M. Vredenberg, T. D. Harris, J. M. Poate, D. C. Jacobson, Y. H. Wong and G. J. Zydzik, "Enhanced photoluminescence by resonant absorption in Er-doped SiO₂/Si Microcavities," *Applied Physical Letters*, vol. 63, no. 19, pp. 2603-2605, 1993.
- [13] A. Narayanaswamy and G. Chen, "Thermal emission control with one-dimensional metallodielectric photonic crystals," *Physical Review B*, vol. 70, no. 12511, 2004.
- [14] W. T. Lau, J.-T. Shen, G. Veronis, S. Fan and P. Braun, "Tuning coherent radiative thermal conductance in multilayer photonic crystals," *Applied Physics Letters*, vol. 92, no. 103106, 2008.
- [15] B. J. Lee, C. J. Fu and Z. M. Zhang, "Coherent thermal emission from one-dimensional photonic crystals," *Applied Physics Letters*, vol. 87, no. 071904, 2005.
- [16] I. Celanovic, N. Jovanovic and J. Kassakian, "Two-dimensional tungsten photonic crystals as selective thermal emitters," *Applied Physics Letters*, vol. 92, no. 193101, 2008.
- [17] A. Narayanaswamy and G. Chen, "Thermal radiation in 1D photonic crystals," *J. of Quantitative Spectroscopy & Radiative Transfer*, vol. 93, pp. 175-183, 2005.
- [18] H. Sai, Y. Kanamori and H. Yugami, "Tuning of the thermal radiation spectrum in the near-infrared region by metallic surface microstructures," *Journal of Micromechanics and Microengineering*, vol. 15, pp. S243-S249, 2005.
- [19] A. Micco, V. Galdi, F. Capolino, A. Della Villa, V. Piero, S. Enoch and G. Tayeb, "Directive emission from defect-free dodecagonal photonic quasicrystals: A leaky wave characterization," *Physical Review B*, vol. 79, no. 075110, 2009.
- [20] J. R. Link and M. J. Sailor, "Smart dust: Self-assembling, self-orienting photonic crystals of porous Si," *Applied Physical Sciences*, vol. 100, no. 19, p. 10607, 2003.
- [21] Y. Gong, X. Liu, L. Wang, H. Lu and G. Wang, "Multiple responses of TPP-assisted near-perfect absorption in metal/Fibonacci quasiperiodic photonic crystal," *Optical Society of America*, vol. 19, no. 10, p. 9759, 2011.

- [22] M. Honda, T. Seki and Y. Takeoka, "Dual Tuning of the Photonic Band-Gap Structure in Soft Photonic Crystals," *Advanced Materials*, vol. 21, p. 1801, 2009.
- [23] Sihvola, "Metamaterials in electromagnetics," *Metamaterials*, vol. 1, p. 2, 2007.
- [24] X.-X. Liu and A. Alu, "First-Principle Homogenization of Magnetodielectric Metamaterial Arrays," *AP-S/URSI*, p. 1522, 2011.
- [25] K. N. Chopra, S. Kumar, J. Joseph and K. Singh, "Advances in Photonic and Microwave Technologies Based on Negative Phase Velocity Materials and Related Topics - A Qualitative Bibliographic Review for the Year 2006: Part I," *J. Science & Technology*, vol. 4, no. 2, pp. 84-127, 2011.
- [26] Soukoulis, "Past Achievements and Future Challenges in 3D Photonic Metamaterials," *Nature Photonics*, vol. 5, no. 523, 2011.
- [27] C. Fu and Z. M. Zhang, "Thermal radiative properties of metamaterials and other nanostructured materials: A review," *Front. Energy Power Eng. China*, vol. 3, no. 1, pp. 11-26, 2009.
- [28] X. Liu, T. Tyler, T. Starr, A. F. Starr, N. M. Jokerst and W. J. Padilla, "Taming the Blackbody with Infrared Metamaterials as Selective Thermal Emitters," *Physical Review Letters*, vol. 107, no. 045901, pp. 1-4, 2011.
- [29] S. L. Wadsworth, P. G. Clem, E. D. Branson and G. D. Boreman, "Broadband circularly-polarized infrared emission from multilayer metamaterials," *Optical Materials Express*, vol. 1, no. 3, pp. 466-479, 2011.
- [30] I. Celanovic, D. Perreault and J. Kassakian, "Resonant-cavity enhanced thermal emission," *Physical Review B*, vol. 72, no. 075127, 2005.
- [31] V. Shklover, L. Braginsky, G. Witz, M. Mishrikey and C. Hafner, "High-Temperature Photonic Structures. Thermal Barrier Coatings, Infrared Sources and Other Applications," *J. Computational and Theoretical Nanoscience*, vol. 5, no. 5, pp. 862-893, 2008.
- [32] R. T. Holm, "Convention Confusions," in *Handbook of Optical Constants of Solids II*, Chestnut Hill, Academic Press, 1991, pp. 21-55.

- [33] Z. M. Zhang, Nano/Microscale Heat Transfer, New York: McGraw-Hill, 2007.
- [34] C. A. Balanis, Advanced Engineering Electromagnetics, New Jersey: Wiley, 1989.
- [35] J.-J. Greffet, R. Carminati and K. Joulain, "Coherent emission of light by thermal sources," *letters to nature*, vol. 416, pp. 61-64, 2002.
- [36] S. M. Rytov, "Correlation Theory of Thermal Fluctuation in an Isotropic Medium," *Soviet Journal of Experimental and Theoretical Physics*, vol. 6, p. 130, 1958.
- [37] S. M. Rytov, Y. A. Kravtsov and V. I. Tatarskii, Principles of Statistical Radiophysics, Berlin: Springer-Verlag, 1989.
- [38] K. Joulain, J.-P. Mulet, F. Marquier, R. Carminati and J.-J. Greffet, "Surface electromagnetic waves thermally excited: Radiative heat transfer, coherence properties and Casimir forces revisited in the near field," *Surface Science Reports*, vol. 57, pp. 59-112, 2005.
- [39] C. A. Balanis, Modern Antenna Handbook, Hoboken: Wiley, 2008.
- [40] Prather, "Photonic Crystal Structures and Applications: Perspective, Overview, and Development," *Journal of Selected Topics in Quantum Electronics*, vol. 12, no. 6, 2006.
- [41] M. Born and E. Wolf, Principles of Optics, Pergmon Press, 1980.
- [42] M. G. Moharam and T. K. Gaylord, "Rigorous coupled-wave analysis of metallic surface-relief gratings," *Journal of the Optical Society of America A (Optics and Image Science)*, vol. 3, no. 11, pp. 1780-7, 1986.
- [43] L. Li, "Use of Fourier series in the analysis of discontinuous periodic structures," *J. Opt. Soc. Am.*, vol. A, no. 13, pp. 1870-6, 1996.
- [44] E. D. Palik, Handbook of Optical Constants of Solids, Orlando: Academic Press, INC, 1985.
- [45] V. Shklover, L. Braginsky, G. Witz, M. Mishrikey and C. Hafner, "High-Temperature Photonic Structures. Thermal Barrier Coatings, Infrared Sources and Other Applications," *Journal of Computational and Theoretical*

Nanoscience, vol. 5, no. 5, pp. 862-893, 2008.

- [46] M. Laroche, C. Arnold, F. Marquier, R. Carminati and J.-J. Greffet, "Highly directional radiation generated by a tungsten thermal source," *Optics Letters*, vol. 30, no. 19, pp. 2623-2625, 2005.
- [47] B. J. Lee, L. P. Wang and Z. M. Zhang, "Coherent thermal emission by excitation of magnetic polaritons between periodic strips and a metallic film," *Optics Express*, vol. 16, no. 15, pp. 11328-11336, 2008.
- [48] C.-Y. Chen, M.-W. Tsai, Y.-W. Jiang, Y.-H. Ye, Y.-T. Chang and S.-C. Lee, "Coupling of surface plasmons between two silver films in a plasmonic thermal emitter," *Applied Physics Letters*, vol. 91, no. 243111, 2007.
- [49] J. J. Burke, G. I. Stegeman and T. Tamir, "Surface-polariton-like waves guided by thin, lossy metal films," *Physical Review B*, vol. 33, pp. 5186-5201, 1986.
- [50] O. G. Kollyukh, L. A. I, V. Morozhenko and V. I. Pipa, "Thermal radiation of plane-parallel semitransparent layers," *Optics Communications*, vol. 225, pp. 349-352, 2003.
- [51] P. Ben-Abdallah and B. Ni, "Single-defect Bragg stacks for high-power narrow-band thermal emission," *Journal of Applied Physics*, vol. 97, no. 104910, 2005.
- [52] L. Savage, "Property Management: A Review of Optical Materials," *Photonics Spectra*, pp. 55-58, September 2011.
- [53] N. P. Barnes and M. S. Piltch, "Temperature-dependent Sellmeier coefficients and nonlinear optics average power limit for germanium," *Journal of the Optical Society of America*, vol. 69, no. 1, pp. 179-180, 1979.
- [54] R. F. Potter, "Germanium (Ge)," in *Handbook of optical Constants of Solids*, Orlando, Academic Press, INC., 1985, pp. 465-478.
- [55] H. H. Li, "Refractive Index of Silicon and Germanium and Its Wavelength and Temperature Derivatives," *J. Phys. Chem. Ref. Data*, vol. 9, no. 3, p. 561, 1980.
- [56] K. Ujihara, "Reflectivity of Metals at High Temperature," *Journal of Applied*

Physics, vol. 43, no. 5, pp. 2376-2383, 1972.

- [57] A. D. Rakic, A. B. Djuricic, J. M. Elazar and M. L. Majewski, "Optical properties of metallic films for vertical-cavity optoelectronic devices," *Applied Optics*, vol. 37, no. 22, 1998.
- [58] V. Kouznetsov, K. Macak, J. M. Schneider, U. Helmerson and I. Petrov, "A novel pulsed magnetron sputter technizue utilizing very high target power densities," *Surface and Coatings Technology*, vol. 122, pp. 290-293, 1999.
- [59] G. T. West, P. J. Kelly and J. W. Bradley, "A Comparison of Thin Silver Films Grown Onto Zinc Oxide via Conventional Magnetron Sputtering and HiPIMS Deposition," *IEEE Transaction on Plasma Science*, vol. 38, no. 11, p. 3057, 2010.
- [60] N. Murphy, L. Sun, A. Waite, J. Jones and R. Jakubiak, "Characterization of Germanium Thin films grown by way of High Power Impulse Magnetron Sputtering and Pulsed DC Magnetron Sputtering," Air Force Research Laboratory, Wright-Patterson AFB, 2012.
- [61] E. Yablonovitch, "Inhibited spontaneous emission in three dimensionally modulated periodic dielectric structures," *Phys. Lett.*, vol. 58, no. 2059, 1987.
- [62] S. John, "Strong localization of photons in certain disordered dielectric superlattices," *Phys. Rev. Lett.*, vol. 58, no. 2486, 1987.
- [63] A. BOMEM, "Research Acquire User's Guide," Analytical and Advanced Solutions, Canada, 2001.
- [64] P. B. Catrysse and S. Fan, "Propagating plasmonic mode in nanoscale aperatures and its implication for extraordinary transmission," *Journal of Nanophotonics*, vol. 2, no. 021790, 2008.
- [65] L. Lin, Y. T. Cheng and C. J. Chiu, "Comparitive study of hot embossed micro structures fabricated by laboratory and commercial environments," *Microsystem Technologies*, vol. 4, pp. 113-116, 1998.
- [66] B. D. Gates, Q. Xu, J. C. Love, D. B. Wolfe and G. M. Whitesides, "Unconventional Nanofabrication," *AR Reviews in Material Research*, vol. 34, pp. 339-372, 2004.

- [67] Q. Xie, M. H. Hong, H. L. Tan, G. X. Chen, L. P. Shi and T. C. Chong, "Fabrication of nanostructures with laser interference lithography," *Journal of Alloys and Compounds*, vol. 449, pp. 261-264, 2008.
- [68] D. Chanda, K. Shigeta, S. Gupta, T. Cain, A. Carlson, A. Mihi, A. J. Baca, G. R. Bogart, P. Braun and J. A. Rogers, "Large-area flexible 3D optical negative index metamaterial formed by nanotransfer printing," *nature nanotechnology*, vol. 6, no. 7, pp. 402-407, 2011.
- [69] P. e. a. Kim, "Structural Transformation by Electrodeposition on Patterned Substrates (STEPS): A New Versatile Nanofabrication Method," *Nano Letters*, 2011.
- [70] Y. Zhang, C.-T. Lin and S. Yang, "Fabrication of Hierarchical Pillar Arrays from Thermoplastic and Photosensitive SU-8," *small*, vol. 6, no. 6, pp. 768-775, 2010.
- [71] I. H. e. a. Hamzah, "PMMA as a Base Material for SU8 Mold to Fabricate PDMS Relief," in *Conference on Science and Social Research*, Kuala Lumpur, 2010.
- [72] P. M. Dentinger, W. M. Clift and S. H. Goods, "Removal of SU-8 photoresist for thick film applications," *Microelectronics Engineering*, vol. 61, no. 62, pp. 993-1000, 2002.
- [73] S. H. Ng and Z. F. Wang, "Hot embossing on polymethyl methacrylate," *SIMTech*, 2007.
- [74] P. A. Anzalone, J. F. Mansfield and L. A. Giannuzzi, "DualBeam Milling and Deposition of Complex Structures Using Bitmap Files and Digital Patterning," in *Microscopy and Microanalysis*, Savannah, 2004.
- [77] G. Chen, *Nanoscale Energy Transport and Conversion*, New York: Oxford University Press, 2005.
- [78] E. Rousseau, A. Siria, G. Jourdan, S. Volz, F. Comin, J. Chevrier and J.-J. Greffet, "Radiative heat transfer at the nanoscale," pp. 1-3, August 2009.
- [79] F. Marquier, K. Joulain, M. J.-P, R. Carminati and J.-J. Greffet, "Coherent spontaneous emission of light by thermal sources," *Physical Review*, vol. 69, no. 155412, pp. 1-11, 2004.

- [80] M. G. M. M. v. Kraaij and J. M. L. Maubach, "A More Efficient Rigorous Coupled-Wave Analysis Algorithm," in *Progress in Industrial Mathematics at ECMI 2004*, Berlin, Springer-Verlag, 2006, pp. 164-168.
- [81] M. G. Moharam, D. A. Pommet and E. B. Grann, "Stable Implementation of the rigorous coupled-wave analysis for surface-relief gratings: enhanced transmittance matrix approach," *J. Opt. Soc. Am. A*, vol. 12, no. 5, pp. 1077-1086, 1995.
- [82] B. E. A. Saleh and M. C. Teich, *Fundamentals of Photonics*, Hoboken: John Wiley & Sons, Inc., 2007.

REPORT DOCUMENTATION PAGE			<i>Form Approved</i> OMB No. 074-0188	
<p>The public reporting burden for this collection of information is estimated to average 1 hour per response, including the time for reviewing instructions, searching existing data sources, gathering and maintaining the data needed, and completing and reviewing the collection of information. Send comments regarding this burden estimate or any other aspect of the collection of information, including suggestions for reducing this burden to Department of Defense, Washington Headquarters Services, Directorate for Information Operations and Reports (0704-0188), 1215 Jefferson Davis Highway, Suite 1204, Arlington, VA 22202-4302. Respondents should be aware that notwithstanding any other provision of law, no person shall be subject to any penalty for failing to comply with a collection of information if it does not display a currently valid OMB control number.</p> <p>PLEASE DO NOT RETURN YOUR FORM TO THE ABOVE ADDRESS.</p>				
1. REPORT DATE (DD-MM-YYYY) 22-03-2012		2. REPORT TYPE Master's Thesis		3. DATES COVERED (From - To) 04 Aug 2010 - 23 Mar 2012
4. TITLE AND SUBTITLE Spectral and Spatial Coherent Emission of Thermal Radiation from Metal-Semiconductor Nanostructures			5a. CONTRACT NUMBER	
			5b. GRANT NUMBER	
			5c. PROGRAM ELEMENT NUMBER	
6. AUTHOR(S) McConnell, Shane N., Captain, USAF			5d. PROJECT NUMBER	
			5e. TASK NUMBER	
			5f. WORK UNIT NUMBER	
7. PERFORMING ORGANIZATION NAMES(S) AND ADDRESS(S) Air Force Institute of Technology Graduate School of Engineering and Management (AFIT/EN) 2950 Hobson Way, Building 640 WPAFB OH 45433-7765			8. PERFORMING ORGANIZATION REPORT NUMBER AFIT/EE.ABET/ENP/12-M01	
9. SPONSORING/MONITORING AGENCY NAME(S) AND ADDRESS(ES) Intentionally Left Blank			10. SPONSOR/MONITOR'S ACRONYM(S)	
			11. SPONSOR/MONITOR'S REPORT NUMBER(S)	
12. DISTRIBUTION/AVAILABILITY STATEMENT APPROVED FOR PUBLIC RELEASE, DISTRIBUTION UNLIMITED				
13. SUPPLEMENTARY NOTES				
14. ABSTRACT The spectral and spatial radiative properties of coherent thermal emission in the mid- and far-IR through the use of micro- and nano-structured metal-semiconductor materials were designed and demonstrated experimentally. Using an implementation of the Rigorous Coupled Wave Analysis and Computer Simulation Technology (CST), two structures were designed to selectively emit at mid- and far-IR wavelengths, a 1-D truncated multilayer resonator and a 3-D hybrid photonic crystal (PC)-multilayer. A High Impulse Power Magnetron Sputtering (HIPIMS) deposition technique was used to fabricate two silver-germanium-silver (Ag-Ge-Ag) resonating structures with layer thicknesses of 6-240-160 nm for one sample and 6-700-200 nm for the other. Ellipsometric measurements showed significant disagreement between HIPIMS-deposited material properties and bulk values found in literature. From radiance measurements, spectral emittance was directly derived and compared to the emittance inferred from reflectance measurements. It was established that inferring emittance can help to approximate the expected emission from a structure, but it is not an exact method of determining the actual emittance. Using CST, the PC-multilayer was modeled to examine its spatial coherence. Initial fabrication results of the PC-multilayer involving both HIPIMS deposition of a Ge-Ag-Ge-Ag (4-12-270-200 nm) multilayer, and focused ion beam milling of a square hole array are also presented.				
15. SUBJECT TERMS Coherent Thermal Radiation, Nanostructures, Infrared, Plasmonics				
16. SECURITY CLASSIFICATION OF:			17. LIMITATION OF ABSTRACT UU	18. NUMBER OF PAGES 155
a. REPORT U	b. ABSTRACT U	c. THIS PAGE U		
			19a. NAME OF RESPONSIBLE PERSON Marciniak, Michael, PhD, USAF	
			19b. TELEPHONE NUMBER (Include area code) 255-3636, x4529 (Michael.Marciniak@afit.edu)	

Standard Form 298 (Rev. 8-98)
Prescribed by ANSI Std. Z39-18